Doctorate Program in Materials Science

Atomic Scale Characterization of Semiconductor Non-Planar Nanostructures

María de la Mata Fernández

Supervisor:
Prof. Jordi Arbiol i Cobos
Tutor:
Dr. Xavier Granados García

October 2015

Instituto de Ciencia de Materiales de Barcelona, ICMAB-CSIC

Physics Department of Science Faculty,
Universitat Autònoma de Barcelona

CHAPTER 4

2D-like Nanostructures: Polarity, Growth Mechanisms and Physical Properties

4.1 2D-like Nanostructures

Although the majority of the work reported within this thesis deals with non-planar morphologies at the nanoscale, the shape diversity of nanoobjects has resulted in the creation of some 2D-like nanostrucutures. However, despite their 2D morphology, these structures have a finite lateral extension and nanometrical thickness, although unconfined length, making the difference with the classical 2D layers or thin films. Therefore, these nanoobjects are in between 2D and 1D structures. In this context, we include nanobelts and/or nanosheets, also referred to as nanoribbons sometimes, nanomembranes and nanoplates. Notice that nanobelts, nanosheets and nanomembranes can be also considered as non-planar nanostructures, as they grow out from a substrate and are not extended on top of its surface. The nanoplates, are instead, the only morphology with a clear planar structure, meaning that is extending parallel to the substrate. Examples gathering a variety of materials, going from II-VI (ZnTe nanobelts) to III-V (InAs nanomembranes) semiconductors, and passing through topological insulators as Bi_2Te_3 2D crystals under the nanoplate shape will be shown in the present section.

Continuing with the directed polar growth mechanisms, the investigations performed on ZnTe nanobelts and sheets allow us to understand the asymmetric lateral expansion of ZnTe nanosheets. In contrast, for the InAs nanomembranes studied, we find a nice example of polarity inversion promoted by the creation of an antiphase boundary (APB) crossing the entire structure from the base to the top, and dividing it in two quasi symmetrical wings (sides). Lastly, we include an example of non-polar growth as it is the case for Bi_2Te_3 nanoplates.

4.2 Lateral Extension: ZnTe Nanobelts

II-VI combinations under nanobelt architecture have been extensively exploited in several applications, such as field emitters, solar cells or sensors [203]. Moreover, they are excellent candidates to probe the emergent nanoscale phenomena, as the electron-phonon interaction occurring in ZnTe nanobelts [204]. Thus, motivated by the emerging interest around II-VI nanobelts and the ability achieved of growing ultralong ZnTe nanobelts reaching the subcentimeter length scale, we perform a comprehensive characterization at atomic scale of the as-grown structures [205]. The study reveals two types of nanobelts attending to their shape, i.e., tapered or straight, which morphology can be explained in terms of the sidewalls polarity, as we will show in the following.

The synthesis is carried out in a vapor-transport system, using $\langle 100 \rangle$ Si substrate precoated with Au to create catalytic droplets. As consequence of the gradient temperature inside the furnace (already commented in Sec. 3.3.1), three different morphologies are

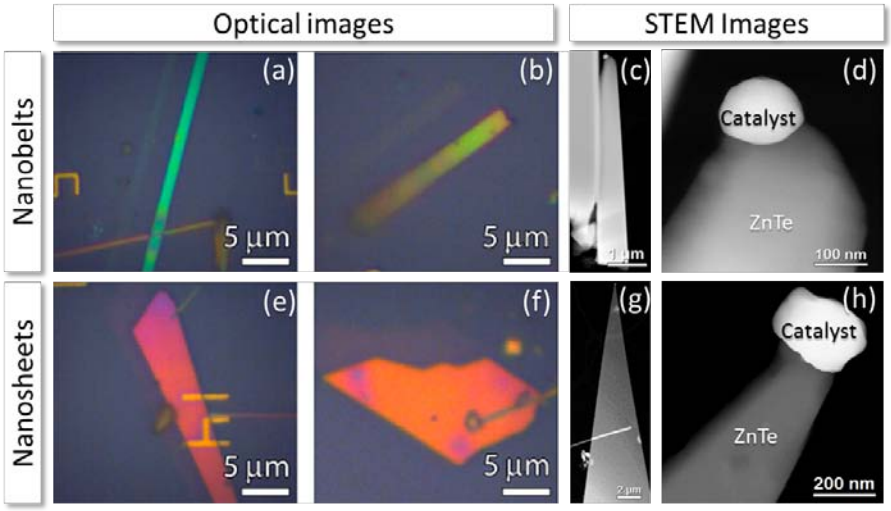

Figure 4.1: Optical micrographs of the nanobelts (a,b) and nanosheets (e,f), and low magnification HAADF images of one nanobelt (c) and one nanosheet (g). Magnified details of the tips are included at the most right column (d,h). Adaped from ref. [205]

developed:

- Kinked micro/nanowires growing at the downstream region with lower local temperature
- moving to warmer substrate areas, long micro/nanowires grow randomly oriented
- and, finally, at the higher temperature regime in the upstream region the substrate is full of very long nanobelts

This morphological dependence of the ZnTe structures with the temperature has been usually attributed to a VS mechanism favored at higher temperatures and responsible of the nanobelt lateral expansion [206]. On the contrary, the lower temperature reached at the downstream prevent the lateral growth and the NW formation is promoted instead. Focusing on the nanobelt structure, analyses of the samples show that within the higher temperature regime two nanobelt morphologies can be developed:
(i) nanobelts with parallel sidewalls and the expected 1D morphology (Fig. 4.1(a-d)), and
(ii) nanosheet-like structures, experiencing strong tapering (Fig. 4.1(e-h)).

PL measurements performed in both, nanobelts and nanosheets, result on pretty similar resonant Raman scattering (RRS) spectra, being the higher PL intensity of the nanobelts the main noticeable difference among them. Up to the 7th order longitudinal optical, LO, phonon emissions are observed when exciting the belts with a 514 nm wavelength, probing the excellent crystal quality of the grown ZnTe nanobelts. The peaks indicated in the Raman spectra included in Fig. 4.2 appear spaced (206 $\pm$ 7) cm^{-1}, corresponding to the frequency of the LO phonon of ZB ZnTe. The main differ-

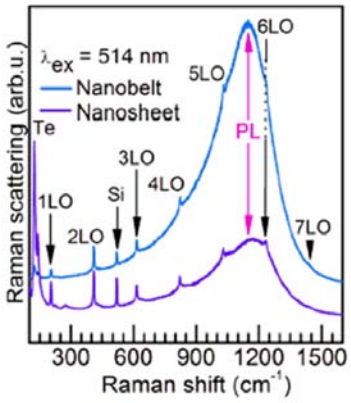

Figure 4.2: Raman spectra acquired in both, ZnTe nanobelts (blue) and nanosheets (purple) excited with a 514 nm wavelength. Adapted from ref. [205].

ence among the two morphologies is the much more intense PL emission observed for the nanobelts (blue plot) compared to the nanosheets (purple plot). The Crystalline Te related emission peaks were also observed, similar to those commented on the ZnTe NWs (Section 3.3.1).

The two different shapes, nanobelts and nanosheets, were studied by HRTEM, EDX and aberration corrected HAADF techniques. Both morphologies preserve the catalyst particle after growing, in agreement with an underlying VLS growth mechanism. Compositional analyses performed by EDX at the two morphologies do not manifest significant differences on their composition: nanobelts (Fig. 4.3(a-f)) and nanosheets (Fig. 4.3(g-l)) are composed of Zn and Te in a 1:1 ratio, while the catalyst particles are mainly composed by gold, showing also slight content of Zn and Te (especially for the nanobelt case).

Regarding their crystallinity, although sharing ZB structure, nanobelts and nanosheets grow along different directions, guided by the catalyst. While the nanobelts grow following one polar {111} direction, the nanosheets axial direction is along the non-polar $[1\overline{1}2]$. Based on our previous knowledge of the material behavior when growing under the similar NW morphology [69, 189], we conclude that the belts should grow along one anionic polar direction, as the $[1\overline{1}1]$, which is more likely to occur. Other similarities can be established between NW and nanobelts, as the presence of transversal twin boundaries, perpendicular to the growth direction, shown in Fig. 4.4(a,b). Unlikely the NW case, especially the cylindrical NWs, twin distribution at the nanobelts is quasi periodic, leading to well defined domains of pure ZB structure.

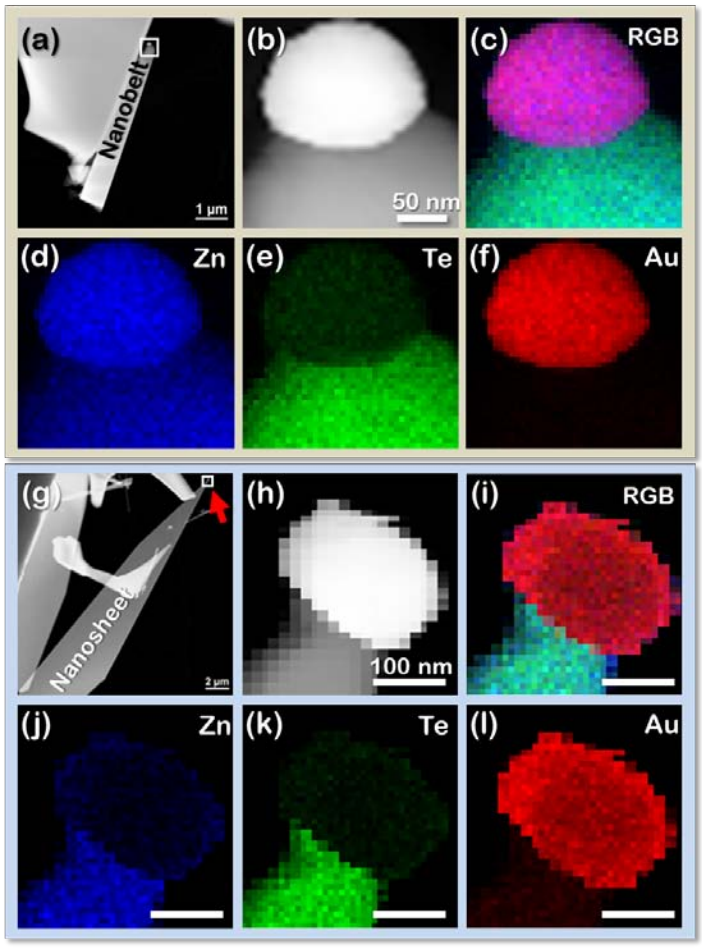

Figure 4.3: EDX results obtained on the tip of the nanobelt shown in (b), at the squared area in (a), where the entire belt can be seen. The EDX signal mapping of the Zn, Te and Au constituents is displayed in (d-f) .The RGB composition of the three signals is included in (c). Low magnification HAADF image of a ZnTe nanosheeet (g). The red arrow points the tip area shown in (h), analyzed by EDX. EDX elemental maps of the nanosheet constituents, Zn (j) and Te (k), and the catalyst, mainly composed by Au (l) are included, along with the RGB composition of the constituents (i). Adapted from ref. [205]

In contrast to the nanobelts, the nanosheets suffer strong lateral tapering while growing axially. The nanosheet VLS elongation growth is promoted along one non-polar {112} direction, as concluded from the presence of the catalyst epitaxed to the $(1\bar{1}2)$ plane at one corner of the structure. The droplet particle can be indexed in agreement with the Au crystalline phase, seen along the [110] direction. It is important to mention the size of the particle, about 200 nm diameter, similarly to the nanobelt case, excluding the possible influence of the catalyst size on the developed morphology. Longitudinal twin boundaries extend from the stepped interface between the droplet and the nanosheet down to the base of the structure along {111} planes. The lateral faceting of the sheets at the straighter base is conformed also by {111} planes. Inter-

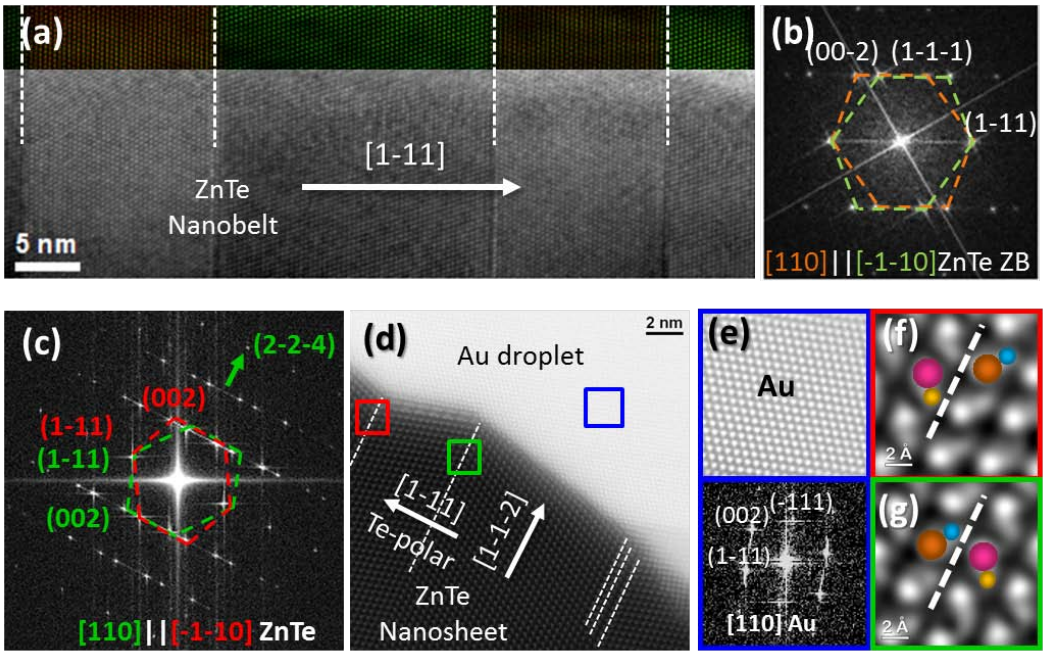

Figure 4.4: TOP PANEL: HRTEM analyses on the nanobelts. Transversal twin boundaries are pointed by dashed lines and by the superposition of the image displayed in (a) with the partial IFFT image where the rotation domains are differently colored, according to the code shown the indexed FFT (b). BOTTOM PANEL: aberration-corrected HAADF structural study performed on the nanosheets. (d) Atomic resolution image at the interface between the ZnTe sheet and the Au droplet, revealing a stepped interface where longitudinal twin boundaries, indicated by dashed lines, emerged. The FFT obtained at the ZB structure shows the presence of two domains related by the twin boundaries (c). Magnified details of the orthotwins are displayed in (f,g). Also a magnified detail of the droplet structure is shown in (e) along with its FFT, indexed in agreement with the Au power spectra. Adapted from ref. [205]

estingly, the catalyst position, almost vertically aligned with the right side facet shown in Fig. 4.3(g), indicates that the lateral growth of the structure is highly favored along the opposite (left hand). Polarity characterizations carried out by intensity analyses at the dumbbells on the HAADF images (see Fig. 4.4(c-g)) reveal that the left hand facet, experimenting further lateral growth, is Te-polar, while the {111} right hand straight facet, is Zn-polar. Therefore, we clarify the influence of the polarity on the growing morphologies and, as occurred with the ZnTe NWs, tripods and tetrapods, the used growth conditions favored the development of the structures following a Te-directed growth. Applying the growth model established by Hao et *al.* [185] on ZnS nanobelts, and based on our observations of further ZnTe growth along the Te-polar directions, the $(1\bar{1}1)$ facet would act as the preferential diffusion direction for the arriving atoms to the catalyst under high supersaturation of the particle, while the Zn-polar $(\bar{1}1\bar{1})$ facet would remain less reactive. In this way, the Te-polar facet becomes the active growth

front, explaining the observed shape.

Regarding the crystalline defects, we have already commented the presence of perpendicular twin boundaries on the nanobelts and longitudinal ones on the nanosheets, always along {111} planes in the ZB structure, and always belonging to the orthotwin category (preserving the polarity across them). No other twin directions, which would promote kinking of the structures, or any extended crystalline defects were detected at the structures, allowing their longitudinal expansion to obtain ultralong straight nanobelts.

Therefore, along with the results presented in the previous chapter, we have completed the growth mechanism study on ZnTe nanostructures, including cylindrical NWs, hexagonally-faceted NWs, tripods and tetrapods, by considering the nanobelts case. Structural and chemical characterizations of belt-like and sheet-like structures are used to analyze the samples. Twining phenomena and polarity effects establish the base to explain the formation of the observed morphologies. In summary, as usually in these kind of materials, twinning is observed along {111} planes, always preserving the polarity. However, twin boundaries are spaced enough to lead the formation of wide ZB domains. The twins are transversal to the nanobelts (perpendicular to the growth) while due to the growth of the nanosheets along the non-polar $[1\bar{1}\bar{2}]$ direction, twins are longitudinal within the nanosheets (parallel to the growth vector). The lateral faceting of the sheets allows their asymmetrical lateral expansion promoted along the Te-terminated $(1\bar{1}1)$ facet but not along the opposite Zn-polar $(\bar{1}1\bar{1})$ one, in good agreement with a B-polar preferential growth.

4.3 InAs Nanomembranes: An Example of Inversion Domain Boundaries

Continuing with 2D-like nanostuctures, nanomembrane architectures can be synthesized nowadays by SAG procedures. The traditional growth of 2D structures relies on the epitaxial extension of one material over another, but mismatch differences between the extended used silicon and III-V combinations, difficult the creation of high quality 2D crystals. However, the growth of free-standing nanoscale structures of III-V materials can be achieved on group IV substrates, as, for instance, NWs or nanotripods among others. In this context, also the growth of vertical InAs nanomembranes on (001)Si has been already reported [187, 207]. The SAG procedure is carried out on patterned holes on SiO_2 masks, on top of (001) Si substrates, resulting on vertical V-shaped nanomembranes created by MBE, without metal pre-deposition (non intended catalyst used).

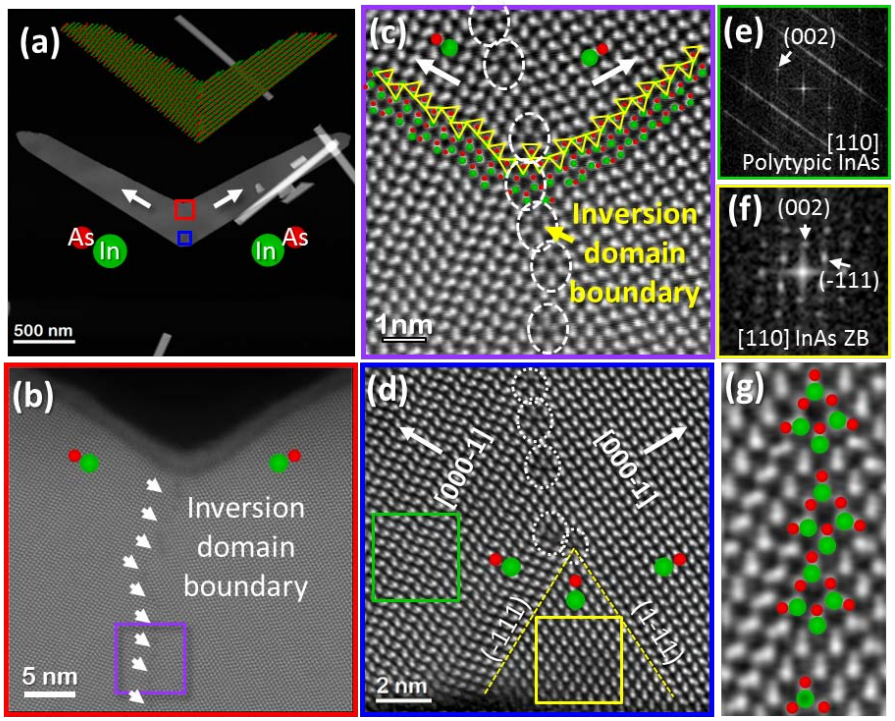

Figure 4.5: (a) Low magnification HAADF image of an InAs V-shaped nanomembrane. The inset corresponds to a 3D atomic model. Atomic resolution HAADF images of the top part of the membrane, where the two wings merged together creating the IDB (b), easily visible on the detail displayed in (c); and of the base of the membrane, showing the triangular ZB nucleus. FFTs taken at one wing (e) and at the seed (f) are also shown. (g) Atomic resolution HAADF image of the IDB, where atomic ring arrangements flipping the polarity are pointed.

Here we address the atomic structure analyses of the membranes by means of HAADF technique. In agreement with the HRTEM observations already reported in ref. [207], we find a triangular nucleus of pure ZB at the central part of the base of the nanomembranes (see Fig. 4.5(d)), and two wings extending outwards, of polytypic InAs phase. The front and back sides correspond to {110} facets. The membranes are flat and regular in thickness, showing an overall V-shape perimeter (Fig. 4.5(a)). The InAs ZB triangle grows along the [001] direction following the underlying Si orientation, as it points the FFT in Fig. 4.5(f). The triangles stand on their (001) basal plane on contact with the Si surface and are laterally bordered by As-polarized {111} planes. From the initial triangular seeds, the lateral expansion of the membrane continues with a randomly aperiodic polytypic structure, close to the WZ hexagonal phase (see Fig. 4.5(b-c)). The placement of the ZB triangles is coincident with the patterned holes, meaning that the nucleation takes place on the bare exposed Si, where the SiO_2 has been removed. The membrane expansion proceeds along the also anionic polar $[000\bar{1}]$ directions lying on the two lateral {111}B borders of the nucleus, inducing the branching of the structures into two "wings ", both with As-polarity through the tips. During

their lateral growth, the membranes keep on growing axially, too. As a consequence, above the ZB triangle vertex, there is a controversial region where the two wings merge together (Fig. 4.5(b-d)). Consequently with the fast polar growth of the wings along As-polar directions, the converging region between them contains two In-polar domains facing each other, as shown in Fig. 4.5(e). Therefore, there is an inversion domain boundary (IDB), which propagates perpendicularly to the substrate along the membranes starting from the ZB triangle top vertex, and dividing the membranes into two polar domains. Although propagating perpendicular to the substrate, the exact trajectory of the IDB is dependent on the polytypic regions combined at both sides of the defect: confronting pure WZ structure at both sides of the boundary leads to the creation of straight defects, while twinning and polytypic mixtures result in local deviations of the IDB trajectory (visible at Fig. 4.5(b)). There are three possible dumbbell orientations in the structures, derived from the branching and the polytypism phenomenon, as pointed in Fig. 4.5(d). The boundary acts as a mirror defect, with dumbbells oppositely oriented at both sides, and vertically aligned dumbbells are allowed in all the different regions, usually connecting both wings (Fig. 4.5(g)). If the two matching regions are purely WZ, the atomic arrangements at the boundary locations consist of ring-like formations composed by 6 atoms, alternating As and In, conforming the IDB. Again, depending on the polytypic sequence, other atomic rearrangements are observed.

It is important to note that the IDB does not reach the base of the membranes where the ZB nucleus is. There, the polarity reversal is stepped, mediated the presence of the ZB, where all the dumbbells are vertically aligned. Such situation might induced different physical properties on the different areas of the membranes, i.e., the base containing the ZB nucleus or the upper merging area between the wings. Therefore, in addition to the polarity inversion among the wings of the membranes, one should account for the vertical asymmetry of the system.

Notice that, as consequence of the preferred unidirectional polar growth, anionic in this case, the branched structures develops an inversion domain boundary, defect not observed in binary NWs free of impurities. The effect of the found polarity reversal may be comparable to the reported for the inversion promoted by a paratwin within a GaAs NW. The plain differences are predicted for the electron transport in presence of non-polar and polar twins. The theoretical calculations accounting for a paratwin (polar defect) and an orthotwin (non-polar defect) by taking GaAs as model system under three different considerations: occurrence of orthotwins, with two possible paratwin configurations, i.e.; mirror twin creating a Ga-Ga bilayer and another for the As-As bilayer, as we reported elsewhere [69]. The performed first-principles electron transport calculations by density-functional theory (DFT) using the Siesta code [208] are summarized in Fig. 4.6. It is easily seen that the conductivity (Fig. 4.6(d)) at the

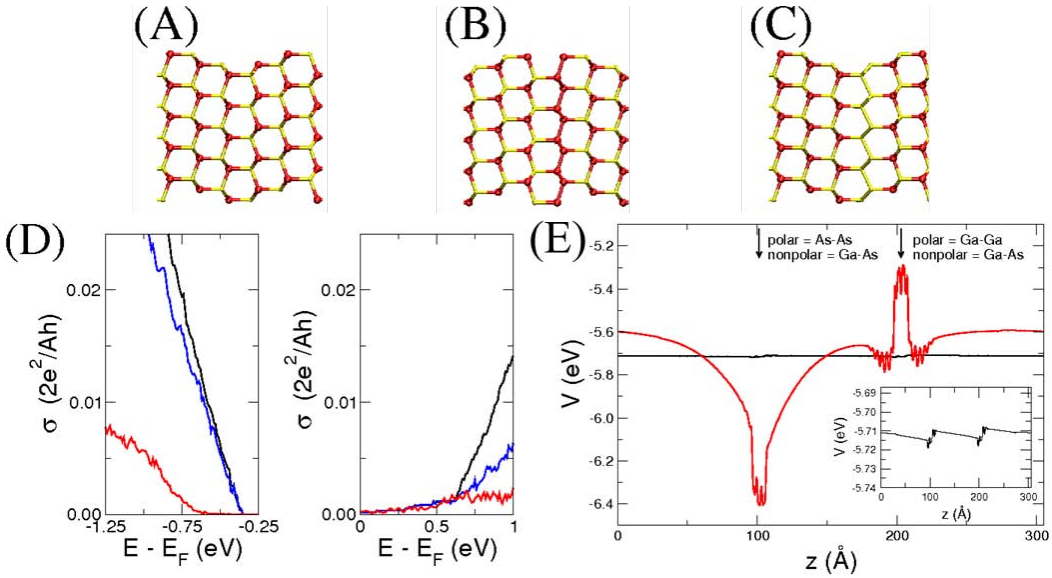

Figure 4.6: Twinned GaAs structure: (a) Orthotwin preserving the Ga-As bilayer (b) Anionic paratwin, leading to a As-As bilayer (c) Cationic paratwin, with one Ga-Ga bilayer (d) Conductivity at the band edges on pristine GaAs (black), on GaAs with two orthotwins (blue) and on GaAs with presence of both paratwin configurations (red). (e) Electrostatic potential as perpendicular to the twin plane for the presence of orthotwins (black) and paratwins (red). The arrows point the twin location. Inset: magnification of the electrostatic potential in presence of orthotwins. Adapted from the supporting information of ref. [69].

band edges dramatically drops if a polar paratwin (red curve) occurs compared with the pristine material (black curve), while the effect of the non-polar orthotwin (blue curve) almost does not perturb the conductivity. This difference between polar and non-polar twins is even more pronounced in the electrostatic potential (Fig. 4.6(e)), which remains almost unchanged in presence of orthotwins but is strongly modified if the twin reverses the polarity. Moreover, plain differences for the electron and hole conductivity can be seen: while the deep well created by the As-As paratwin imposes a barrier for the holes, the sharp barrier exhibited by the Ga-Ga paratwin scatters the electrons. This is true for defective homostructures, but even more for heterostructures where the spontaneous polarization leads to interface charges which strongly modify the band alignments depending on the polarity at both sides of the heterointerface [41]. The unavoidable discontinuity on the band structures when switching the material, i.e., at the interface, can be exploited to create 2-dimensional electron gases (2DEG), 2-dimensional hole gases (2DHG) or tunel diodes for instance, just by playing around with the polarity at both sides of the interface.

In the case of InAs nanomembranes, lattice deformation measurements performed by means of peak pair analyses (PPA) (more details on the strain analyses are given in Section 2.4.1) at the membranes show that the IDB is remarkably strained. In the

strain maps obtained around the IDB area, the lattice deformation along the defect is evident when accounting for the average lattice distortion along x (ϵ_{xx}) and y (ϵ_{yy}) directions (D_{xy}). The main strain results are summarized in Fig 4.7, where the mapped strain is presented (b) along with the analyzed atomic resolution HAADF image of the boundary (a) and their superposition (c). In (b) and (c), the lattice distortions at the boundary are noticeable from the temperature color code, and highlighted by the integrated intensity profile crossing the defect included in (d). Apart from the boundary, the lattice structure of the membrane is relaxed, and the only variations observed are related to the twinning.

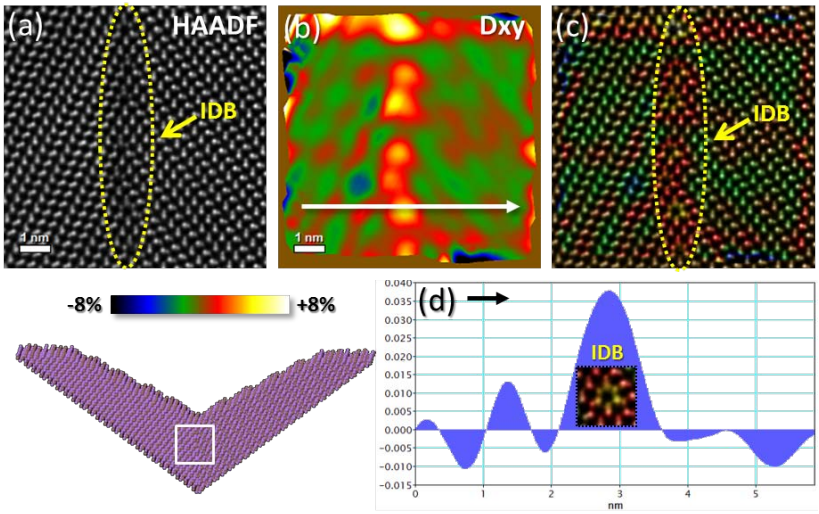

Figure 4.7: Strain measurements performed at the IDB of the InAs nanomembranes, by means of PPA. The analyzed region is shown in (a), the strain distribution can be seen in (b) and their superposition is displayed in (c). The IDB location is indicated in (a) and (c). (d) Intensity profile across the strain map in (b) following the arrow, highlighting the lattice deformation at the IDB. The left bottom inset corresponds to the atomic 3D model of the structure, pointing the analyzed area.

On this way, we atomically show that, guided by the fast anionic polar growth of InAs under the employed conditions, V-shape nanomembranes systematically have two polar domains, separated by a vertical IDB. The atomic disorder induced while connecting planes belonging to the different wings results in the presence of strain fields along the length of the boundary. At the base of the membranes, the existence of a triangular ZB nucleus sharing base with the membrane and growing along the [001] direction offers an alternative, giving rise to an area where the lateral polarity reversal is stepped. Further studies should clarify the experimental implications of such polarity distribution on the physical properties (e.g.: formation of internal potential barriers blocking the carrier conduction).

4.4 Crystalline Defects Driving the Morphology: InSb Nanosails

We have earlier commented on the popularity of nanostructuration as a common strategy through materials functionalization. There are two main ways for synthesizing nanostructures, classified as bottom-up or top-down, depending on whether small building blocks are piled up to reach the desired morphology or contrary, the material is firstly synthesized and from there, its size is reduced. Today, a huge control over some procedures has been achieved, especially on physical growth procedures, such as the molecular beam epitaxy (MBE), pushing the nanoengineering one step further. As the position, phase, size, shape and growth direction can be tuned with a high precision, playing around with material combinations or phase engineering allows the creation of novel structures and functionalities.

The manifold synthetic possibilities rely on the management of different growth parameters to enhance or inhibit the material formation under certain conditions or along particular directions. Due to the demand of high quality crystals, the phase purity or presence of crystalline defects should be carefully controlled. However, the presence of defects can be also exploited to engineer the structure on the desirable way. This is the case of twinning superlattices or intentionally induced polytypism, where by switching the phases, twinned related, the band gap can be modulated at will [9, 195, 209]. Nevertheless, morphological issues occurring during the growth of nanostructures are also linked to the presence of crystalline defects, as we illustrated for the tetrapod example, developed thanks to the lattice rotation driven by a twin boundary occurring at the nucleation stage. In fact, crystallographic defect engineering can be successfully exploited in order to create complex morphologies at the nanoscale, as it happens with branched structures driven by dislocations [186]. Along this section we show how the overall shape of a nanoobject can be dictated by the presence of a unique twin within the structure. We called these structures nanosails (NSs) in the following, for their resemblance in shape with the sail of a boat.

It is noteworthy that the NSs are created when growing InSb NWs on top of InAs template stems, showing much smaller yield than that of the NWs. A SEM picture of the as-grown sample is shown in Fig. 4.8(a), where the prevalence of the NWs over the NSs is obvious. In any case, the NSs can be described as wide (hundreds of nanometers) flat structures growing perpendicular to the substrate, on top of InAs stems. The growing NWs along with the NSs are hexagonally faceted by six equivalent {110} planes and show pristine ZB phase, where none structural defects were observed. In contrast, the NSs have a more complex faceting but showing still some {110} planes and its phase

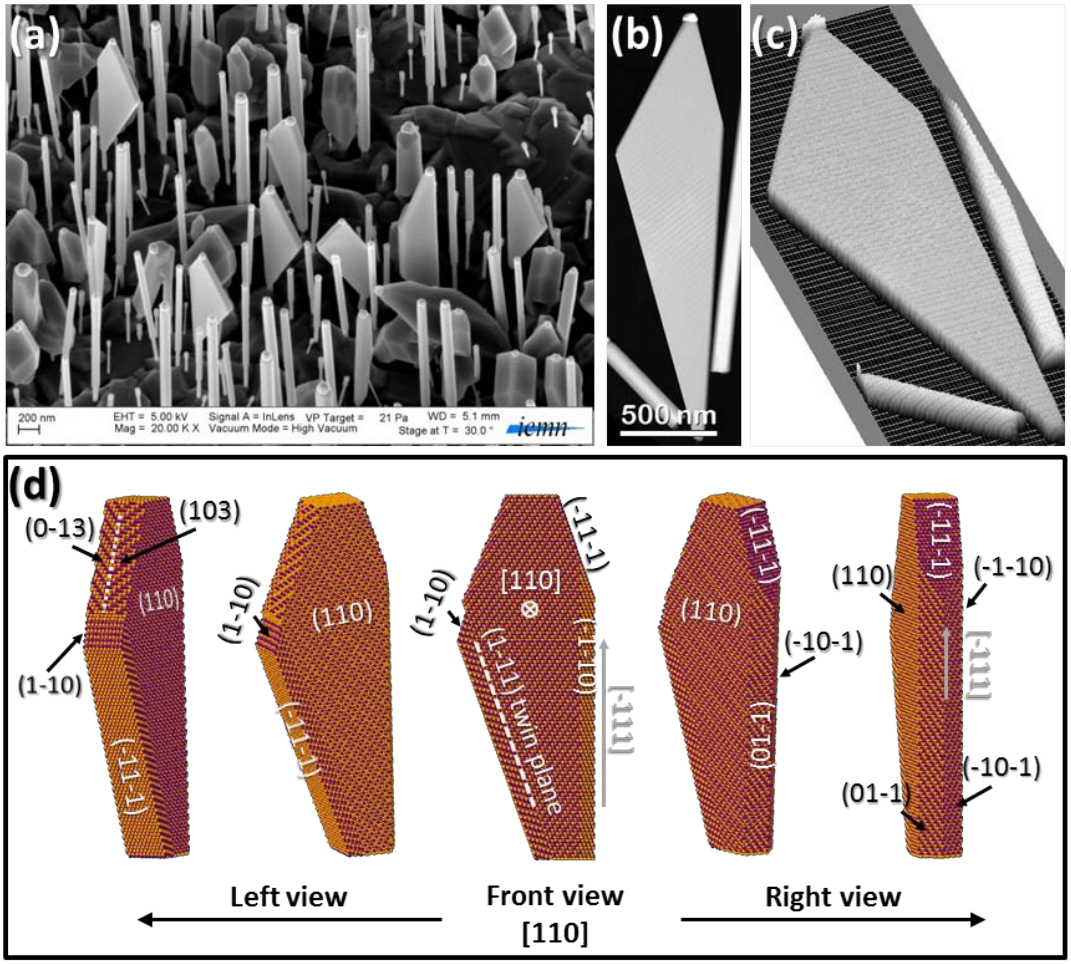

Figure 4.8: (a) Tilted view (30°) SEM image of the as-grown sample containing InSb NWs and NSs. (b)HAADF image of one NS, also displayed as a surface plot (c). (d) 3D atomic model of the NS structure view along different directions, where its faceting is included.

purity is as good as in the NWs, with the only exception of the presence of one single twin boundary at every NS. The twin occurs along a {111} plane, parallel to one of the sail facets, running along its whole length from the base until the facet is extinguished, as schematically shows the 3D model included in Fig. 4.8(d). The perfect ZB structure grows oriented with the $\{\bar{1}11\}$ plane, Sb-polar, parallel to the surface substrate. Importantly, the presence of the twin is mandatory to create the NS as we show in the following; otherwise the growth would proceed to create a NW as it happens in most of the cases.

The morphology of the structures in terms of the ZB crystallographic planes is depicted in Fig. 4.8, where we included a 3D atomic model with indexed facets. Four of the {110} sidewalls present on the wires can be found also at the NSs, conforming the

frontal and back sides ([110] and $[\overline{1}\overline{1}0]$) and other two lateral facets that converge along the $[\overline{1}11]$ direction, creating the right corner of the sails at the sketches. In contrast, the opposite side (left) is defined by a unique {111} plane, parallel to the top right facet. Lastly, the left top facet is again a combination of two different planes, that coincide to complete the NS faceting. The different facets might evolve more or less, leading to a variety of asymmetric shapes.

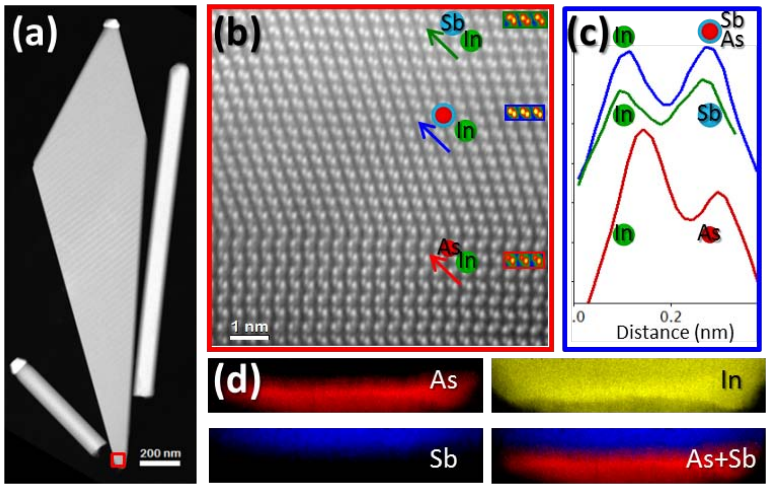

Figure 4.9: (a) Low magnification HAADF image of one analyzed NS. (b) Atomic resolution HAADF image of the base of the NS, where the last monolayers of the InAs stem can be seen (WZ structure). The $InAs_{1-x}Sb_x$ graded interface before the pure InSb ZB is evident when analyzing the dumbbells intensity at different heights from the base, following the colored arrows. The results are gathered in (c). (d) As, In and Sb mapped EELS signals at the base, showing the blunt As-Sb transition confined to a narrow region. The As and Sb RGB composition is also included.

The thickness of the NSs is a direct consequence of the size of the metallic droplet used for the growth, meaning that their thickness is tunable, similar to the reported observations for the NWs diameter [210, 211]. Au droplets are used to initiate the growth of the InAs stems, on top of which the InSb structures are developed. The InAs stems firstly grown crystallize on the WZ structure along the As-polar $[000\overline{1}]$ direction, while the antimonide shows pristine ZB structure, where the growth plane is the $\{\overline{1}11\}$, Sb-polar. The post-grown droplet was found to be pure $AuIn_2$, perfectly epitaxied to the InSb structure by the $(\overline{1}11)[110]_{AuIn_2}||(1\overline{1}1)[110]_{InSb}$ relationship (more details on the $AuIn_2/InSb$ matching can be found in section 5.2.3).

Structural characterizations performed at the sails by means of atomic resolution HAADF technique show still few monolayers of the WZ InAs stems, attached to the base of the NSs. Note that the stems break down when scratching the nanostrucutures to be deposited on the TEM grid, since they remain adhered to the substrate

while the wider parts are removed apart. The InAs observation at the base of the NSs was further confirmed by spectroscopic measurements (EELS results included in Fig. 4.9(d)) performed on the sample. To address the polarity at both phases and the abruptness of the heterointerface between the InAs and the InSb we carefully inspect the dumbbells intensity at the first monolayers of the ZB phase. The results highlight the strong trend of antimony compounds to crystallize under cubic structures, since the introduction of small amounts of Sb within the InAs lattice spontaneously promotes the transition from WZ to ZB. About 2 nm above the WZ-ZB transition interface, the pure InSb stoichiometry is already reached and kept along the entire NS. However, the 2 nm thick $InAs_{1-x}Sb_x$ transition layer cannot be neglected. Another remarkable result of the dumbbell analyses is the fact that both, the InAs and InSb growth planes are anion-polar and, logically, also the intermediated $InAs_{1-x}Sb_x$ section.

We have already mentioned that the NSs faceting is partially common to the NWs one, due to high stability of the {110} planes. But the asymmetry of the NS morphology is induced by the presence of a lateral twin boundary emerging at the base of every sail along the $\{1\bar{1}1\}$ plane, breaking the hexagonal symmetry of the NWs faceting. Although an accurate model depicting the underlying growth mechanism is missing yet, the appearance of the twin allows overcoming the barrier imposed by the {110} lateral faceting at this site and acquiring instead a $\{\bar{1}1\bar{1}\}$ lateral facet. At this stage, the system is likely growing simultaneously vertical, following the trend of the NWs, and expanding laterally from the twin occurrence that apparently opens another growth front. It should be pointed that the narrow width of the twinned region (extending exactly 25 {111} planes on the example in Fig. 4.10(a-d)) is preserved along its entire length, and its location is so close to the NS border that its influence on the main core electronic properties (e.g. axial transport) will be hardly noticeable. The twinned region is $\{1\bar{1}1\}$ limited at the top, where the facets switch in order to squeeze the structure, meeting at the $\{\bar{1}1\bar{1}\}$ plane already created at the opposite site.

The atomic resolution images taken at the bases of the NSs show the initial superposition of the two different ZB orientations, i.e., [110] and $[\bar{1}\bar{1}0]$, related by the presence of the twin (see Fig. 4.10(d,h)). Such observation is consistent with the gliding of the twin along an oblique plane (tilted in depth plane), and thus, leading to the observation of both lattices overlapping. The gliding plane ought to finish when reaching the NS surface, and from there, the two rotation domains, twin related, are clearly projected side by side (sharing the $\{1\bar{1}1\}$ twin plane). It should be mentioned that the phase transition from the InAs to the InSb is accompanied with a broadening on the NW diameter for the axial heterostructures observed on the sample, and reported in other works [95, 212, 213] (for more details on the diameter increase the reader is referred to Section 5.2.3). In those cases the morphological transition takes place by the creation

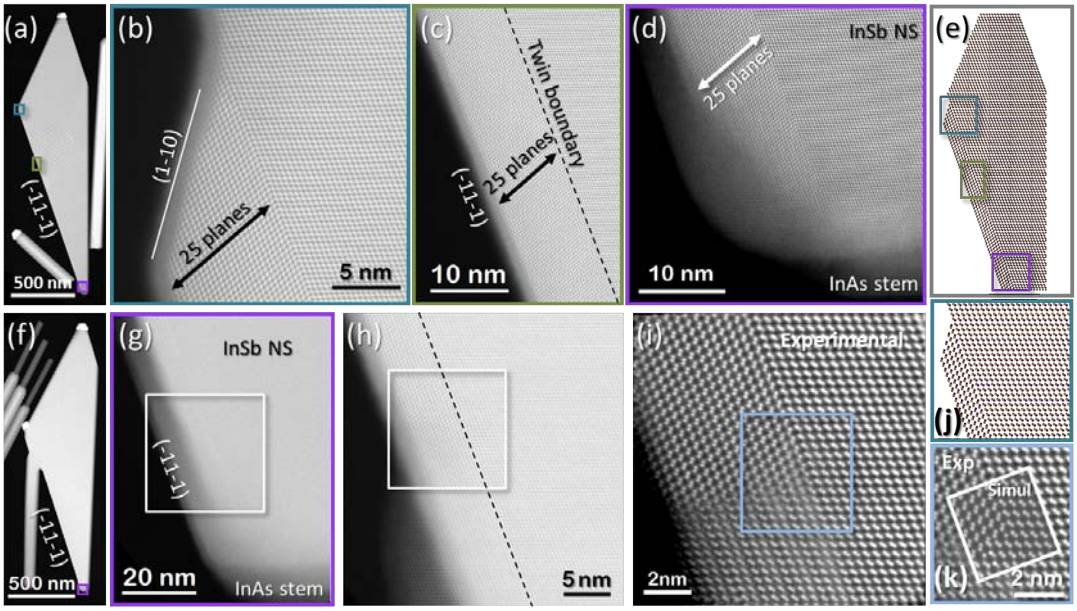

Figure 4.10: (a,f) Low magnification HAADF images of two NSs. Atomic resolution HAADF images at different heights (pointed in the image in (a) and the 3D model in (e)) of the $(\bar{1}1\bar{1})$ lateral side of the NSs where the twin is placed, from the base (d) until its ending (b, j), including the intermediate region (c). Note the constant thickness of the twinned area. (g-i) images show the crystalline structure at the base of the sail in (f) at different magnifications. (k) Simulated image superimposed to the experimental at the beginning of the twin.

of {113} planes connecting the two sections with different sizes. It would be reasonable assuming a similar faceting here, responsible for the twin gliding. From the emergence of the twin, the growth proceeds by a lateral expansion of the structure while it keeps on growing axially.

Once seen the high crystalline quality of the NS, the electronic material quality has been proven through electric measurements performed at isolated NSs. The measurements were conducted by using the van der Pauw geometry (shown as inset in Fig. 4.11(a)) by positioning the NSs lying on a highly conductive substrate covered by more than 200 nm of thermal oxide acting as back gate. Such experiments provide information on the carrier density (due to the Hall effect), the intrinsic conductivity and the carrier mobility.

Fig. 4.11(a) shows the linear dependence of the Hall voltage with the magnetic field, **B**, applied perpendicular to the surface of the NS, for specific back gate voltages in the range of 2-7 eV. At high temperature, the dependence of the Hall voltage as a function of the back gate voltage is non monotonous, indicative of both types of carriers, electrons (n) and holes (p), since n increases for positive voltage values while p does it

for negative ones. Thus, by lowering the temperature and using only positive voltages, we exclude the contribution of the holes to the transport and we can apply the single carrier model to determine the electron surface density n_s, which is plotted as a function of the back gate voltage and for different temperatures in Fig 4.11(b). Fitting the linear region for the lower temperature checked (40 K), results in a slope of $1.36 \pm 0.13 \cdot 10^{-4}$ C/cm^2, in agreement with the expected charge density for an equivalent thick capacitor (estimated to be 1.5 C/cm^2).

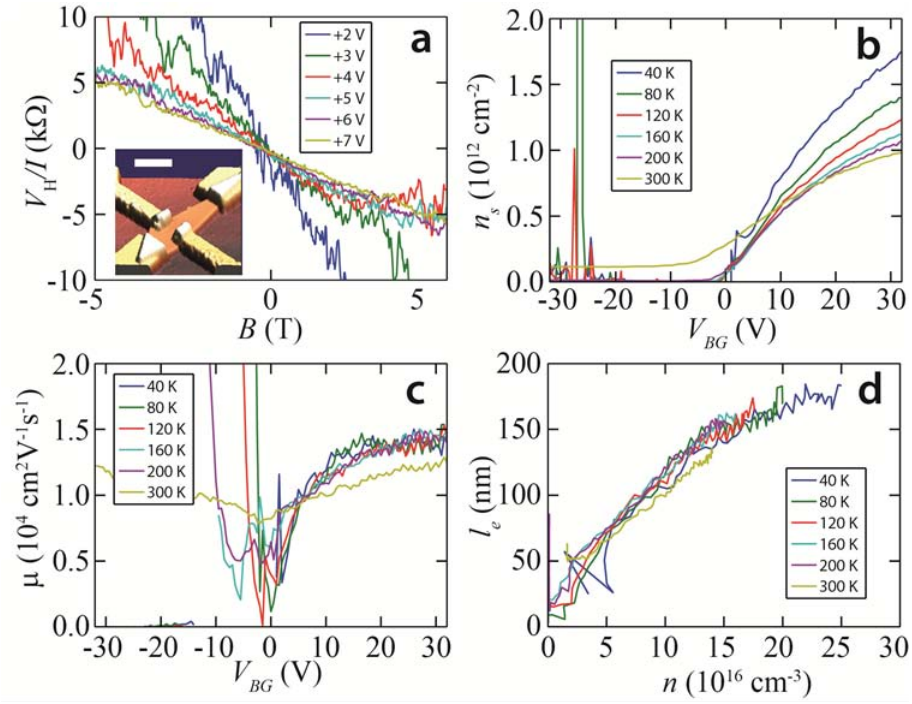

Figure 4.11: (a) Hall voltage as a function of B (perpendicular to the NS surface) for different voltages applied on the back gate (values given in the legend) and at a temperature of 2.1 K. The inset shows an atomic force microscope image of the four-terminal NS device (scale bar 500 nm). (b) Electron density deduced from the Hall measurements and using the single carrier model as a function of the back-gate voltage, for different temperatures (values given in the legend). (c) Electron mobility as a function of the back-gate voltage. (d) Elastic mean free path as a function of the bulk carrier density (assuming an homogeneous carrier distribution over the 70 nm thickness of the NS).

The conductivity measured is also a consequence of both types of carriers. But, again it is dominated by the electrons at low temperatures and positive voltages, allowing extracting the electron mobility, μ, by assuming the single carrier model. The resulting data is plotted as function of the gate voltage for various temperatures (Fig. 4.11(c)). Importantly, at room temperature we find out mobilities as high as $1.25 \cdot 10^4$ $cm^2/(Vs)$ for a 70 nm thick sail. Although the experimental mobility found is still lower than the bulk one, it is four times larger than the best reported value for a 70 nm thick

InSb layer on GaAs, reaching values reported for 300 nm thick layers [214,215]. Finally, we have calculated the electron mean free path (l_e) as function of the electron density, as shown in Fig. 4.11(d). The large resulting mean free path values found hint the possible ballistic transport regime in the structures, addressed in the following.

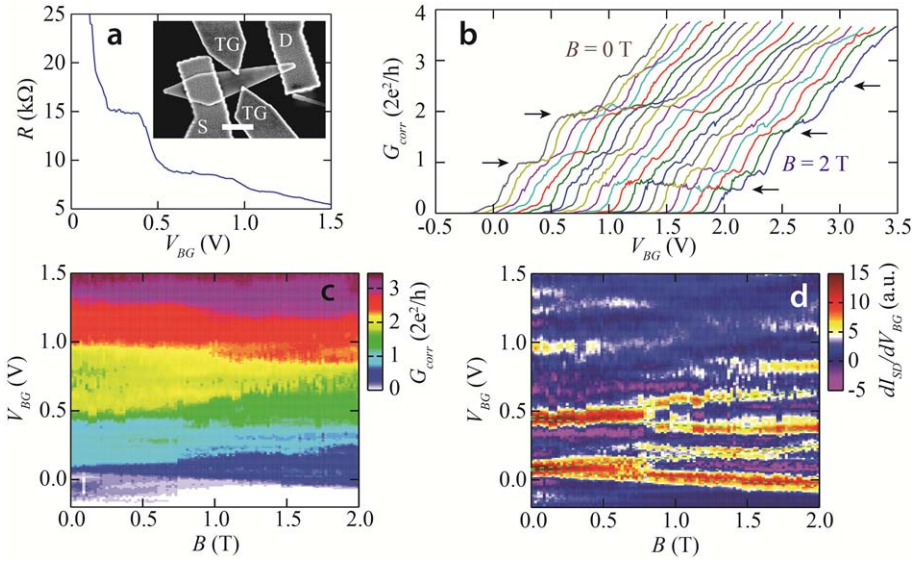

Figure 4.12: Top-gated quantum point contact in an InSb nanosail. (a) Two-point source-drain resistance as function of the back-gate voltage, for a fixed voltage applied on the top gates ($V_{TG} = +0.68V$) at T = 6 K. The inset shows the top-gated quantum point contact device (scale bar 500 nm). (b) Corrected conductance obtained after removing a 2 kΩ series resistance from the two-terminal resistance (contact resistance) as a function of the back gate voltage and varying the parallel magnetic field from 0 to 2 T by = 0.1 T steps. The measurement has been performed at T = 6 K, and the curves have been laterally shifted by 0.1 V for clarity. The arrows emphasize the steps corresponding to conductance quantization. (c) Corrected conductance as function of the parallel magnetic field and back gate voltage, measured at T = 2.1 K. (d) Color map of the dI_{SD}/dV_{VG} as a function of the parallel magnetic field and the back-gate voltage emphasizing the conductance steps, showing the splitting of the two first conductance steps measured at T = 2.1 K.

Therefore, we constrict the system by incorporating two top gates, as it is indicated at the inset in Fig. 4.12(a), creating a quantum point contact. The resistance measured at a fixed top gate value ($V_{tg} = +0.68V$) as function of the back gate voltage, V_{BG} in absence of magnetic field, evidences the 1D transport. The 1D carrier quantization is clear in Fig. 4.12(a), where the plateaux at 15 and 8.5 kΩ, correspond to $h/2e^2$ and $h/4e^2$ level, respectively. The constant 2 kΩ deviation from the expected values (12.9 and 6.5 kΩ instead of 15 and 8.5 kΩ) is mainly attributed to the contacts. The corrected conductance, G_{corr} it is plotted in Fig. 4.12(b) as function of the applied back-gate voltage (curves are 0.1 V laterally shifted for clarity) for an applied magnetic field within the 0-2 T range (every 0.1 T) parallel to the NS surface. The plateaux at

$2e^2/h$ and $4e^2/h$ fade while increasing **B**, disappearing completely at 2 T and giving rise to plateaux at e^2/h, $3e^2/h$ and $5e^2/h$. This fact is better illustrated in Fig. 4.12(c), where the different colors correspond to discrete quantized levels. As **B** increases, even plateaux shrink and odd ones appear, possibly due to the 1D subband spliting. In order to emphasize the edges of the plateux, we plot the differential conductance, dI_{SD}/dV_{VG} included in Fig. 4.12(d), where the splitting of the two firts subbands is evident.

On one hand, it is noteworthy that, even though InSb NWs are expected to show 1D transport, it has been only demonstrated at high magnetic fields [216]. On the other hand, 1D transport in InSb has been reported in 2D electron gases at heterointerfaces, but not in free-standing InSb systems, such as the present NSs [217].

4.5 An Unpolar Case: Bi_2Te_3 Nanoplates

Covering 2D related structures, it is worth mentioning the recent interest on the V-chalcogenide compounds, such as Bi_2Se_3, Bi_2Te_3 or Sb_2Te_3. Their popularity emerges from their topological insulator behavior, induced by the presence of both, conducting surface states and insulating bulk states. This especial condition turn them into promising materials for exploring phenomena in condensed matter physics, as well as allowing the fabrication of disipationless devices and quantum computers [218, 219].

Until now, all the examples shown along the chapter deal with binary combinations showing 1:1 stoichiometry and sharing structural phases. In contrast, V-VI combinations use to crystallize under rhombohedral space groups, and the charge compensation among A^{3+} and B^{2-} leads to a 2:3 stoichiometry of the compounds. These systems are prone to develop 2D shapes due to their layered structure, which can be described as the stacking along c-axis of quintuple layers (QL) following the B-A-B-A-B sequence, where A-B bonds within the QL are covalent while only van der Waals forces are established among different QLs (B-B bonding). As a consequence, there is a van der Waals gap spacing between the QLs along the c-axis. Such structural phase is advantageous for the development of 2D crystals, as Bi_2Te_3 nanoplates (NPTs).

Motivated by the increasing interest around these materials, we have reported extensive structural and chemical characterization on Bi_2Te_3 NPTs synthesized following a vapor transport route on SiO_2 coated Si substrates. The detailed (S)TEM characterizations of the samples are intended to spread the control over the synthetic process and improve the abilities on the structural design of the NPTs, provididing us the basis for postulating their growth mechanism. An approach to determine the NPTs thicknesses by the optical contrast of the NPTs on SiO_2/Si substrate completes the study [220].

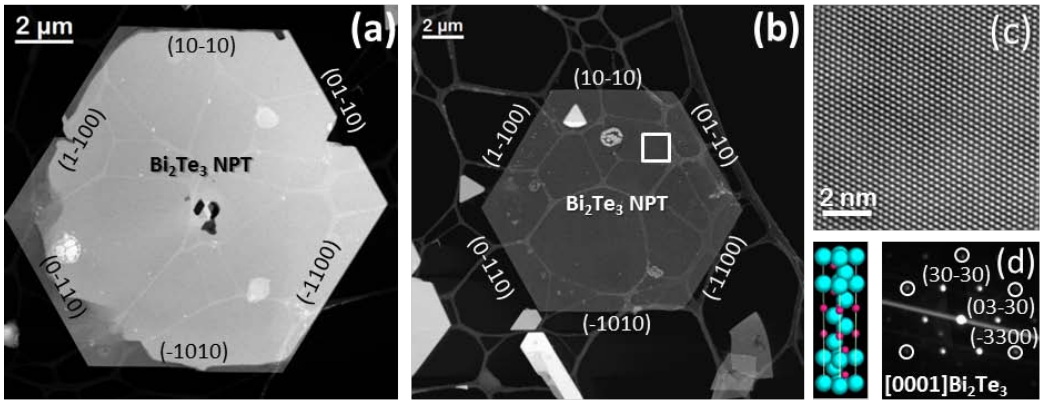

Figure 4.13: Low magnification HAADF images of two $Bi2Te3$ NPTs with different thicknesses, one thicker (a) and another thinner (b). The top view of the lattice structure is shown in (c), and the corresponding indexed SAED pattern (which allows the NPT facet identification) in (d), side by side with the 3D unit cell. Adapted from ref. [220].

The structural analyses are conducted by HRTEM, STEM and SAED techniques, under two orthogonal directions which allow studying the NPTs from top (planar) and lateral (cross-section) views. The synthesized NPTs are large hexagons (wider than 10 μm) faceted by {01-10} planes, and growing along the [0001] c-axis of the Bi_2Te_3 structure, to reach a final height ranging from few nanometers down to 3 QLs (3 nm). The thinner NPTs are useful for the planar view imaging while thicker NPTs are preferred for the cross-sectional analyses due to sample preparation limitations.

The Bi_2Te_3 crystallizes on the $R\bar{3}m$ space group (rhombohedral) as extracted from the SAED patterns, also useful for the identification of the facets and growth direction. Regarding the crystal quality of the Bi_2Te_3 phase, no extended defects are detected when visualizing the NPTs along the growth direction (top view). The morphological issues and the SAED pattern are included in Fig. 4.13. It is worth mentioning that on the planar view sample, we notice one small hole around the center on most of the hexagons observed, tentatively attributed to the pinning point among the NPTs and the substrate, as further explained later. Importantly, the TEM sample has been prepared by removing the NPTs from the substrate which can promote the hole creation when de-attaching the NPTs.

To get more insights on the growth mechanism of these planar structures, we prepare a cross-section sample where the NPTs remain attached to the substrate. Fig. 4.14(b) shows one example of the cross-sectional view of a thick NPT on the Si substrate, along with its surface plot. In addition to the structural analyses, the figure summarizes the

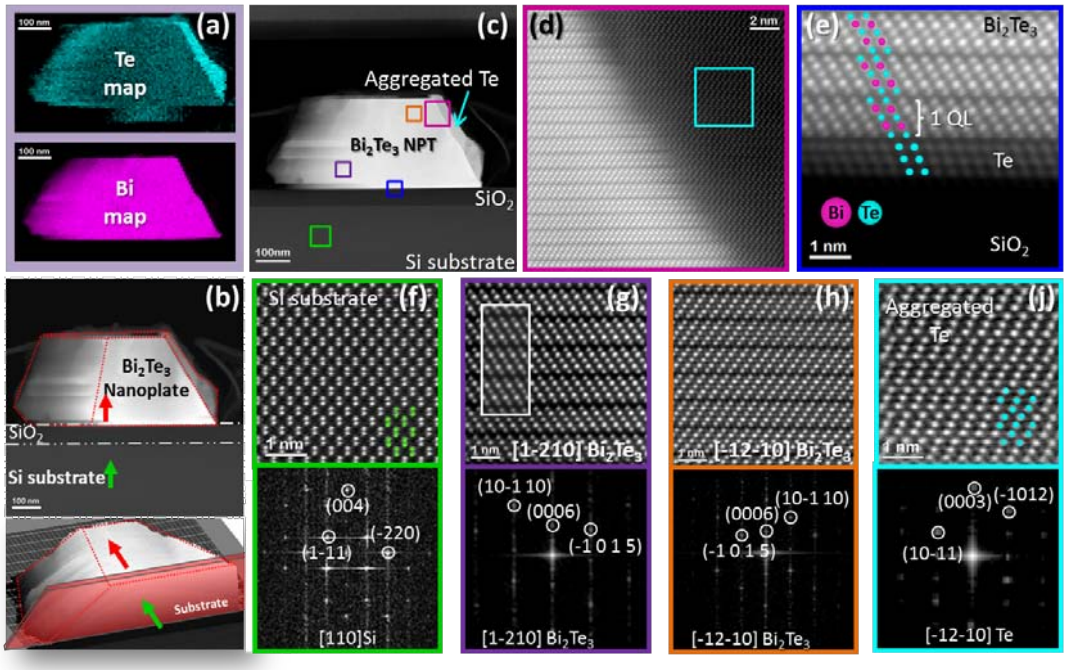

Figure 4.14: (a) Te (cyan) and Bi (pink) EELS maps acquired at the NTP shown in (b), along with its surface plot (below). (c) HAADF image of the NPT pointing the regions analyzed under atomic resolution conditions in (d-j), including images of the Bi_2Te_3/Te aggregated and of the NPT/substrate interfaces, and magnified details of all the phases found (Si in (f), two Bi_2Te_3 orientations in (g, h) and the pure Te structure (j) of the aggregated). Adapted from ref. [220].

main compositional results obtained by means of EELS. The Bi and Te signal maps (Fig. 4.14) reveal two important features: (i) the presence of a Te structure aggregated to the right lateral side of the analyzed NPT, deducible from the lack of Bi and the brighter Te signal at that region, and, (ii) the penetration of Te into the SiO_2 until reaching the pure Si underlying, presumably being the pinhole of the NPT. The atomic resolution HAADF images taken at the NPT confirm the presence of crystalline Te at both, the lateral side of the NPT (Fig. 4.14(d)) and below its base (Fig. 4.14(e)). The Te crystals observed belong to the $P3_121$ space group and grow along the c-axis, as well as the Si substrate and the Bi_2Te_3 NPT, regardless their location (i.e., below the NPT or laterally attached). At the NPT base, only 3 atomic layers of the Te phase are visible before embedding on the oxide. We can correlate these two facts (the crystalline nature of the Te and its deep penetration into the SiO_2 until the Si) with the existence of Te seeds epitaxially pinning the plates to the substrate. In addition, this situation provides a potential explanation for the observed holes on many NPTs from the planar view. The NPTs removal from the substrate is conducted by chemical etching of the SiO_2. However, the Te seems not to be affected during the etching process and remains attached to the substrate, inducing the formation of the hole on NPTs when they are

torn from the substrate.

The Te structure at the lateral side of the analyzed NPT is perfectly oriented with respect to the Bi_2Te_3, being both phases $[\bar{1}2\bar{1}0]$ oriented and growing along their c-axes. Misfit dislocations appear at the interface, mainly due to the van der Waals gaps in between consecutive QLs on the bismuth telluride, not reproduced on the pure Te. The presence of Te structures can be explained on the attending to the vapor transport process, based on the Bi_2Te_3 sublimation and recrystallization. The $Bi_2Te_{3(s)}$ decomposition is expected to originate 2 $BiTe_{(g)}$ and 1/2 $Te_{2(g)}$, but a possible incongruent sublimation process leading to the creation of vapor phase Te rich has been suggested on the literature [221]. The Te rich vapor conditions induce phase segregation and result in the crystallization of both Bi_2Te_3 and Te according to the Bi-Te phase diagram [222].

Regarding the Bi_2Te_3 crystalline phase, it should be noted that two different orientations twin related were found within the NPT, shown in Fig. 4.14(g,h), corresponding to the regions purple and orange framed in (c). Previous works on the same material have reported the observation of (0001) basal twins [223, 224], also energetically favorable from theoretical calculations [223]. Thus, it is likely our NPT show same kind of basal twins. However, as the orientation is kept for large areas (tens of QLs), it is assumable that for the thinner NPTs, with heights of few QLs, twin boundaries are not created.

Gardening all the information, we can postulate a model for the NPTs growth. At the first stages of the growth, the sublimation of Bi_2Te_3 results in the formation of Te-rich vapor promoting the crystallization of Te seeds on the substrate, with the possibility of diffusing into the SiO_2 before condensing, to create the crystalline Te pinhole attached to the Si. Then, $BiTe_{(g)}$ and $Te_{2(g)}$ are preferentially absorbed on the Te seeds, where they react to form the Bi_2Te_3. The axial growth of the NPT proceeds in a layer-by-layer mode, leading the creation of the epitaxial NPTs. The absence of Te pinholes in some NPTs may be due to their merging with the NPT or its reaction with the $BiTe_{(g)}$ to become Bi_2Te_3.

Therefore, we have shown that large thin hexagonal Bi_2Te_3 NPTs can be obtained by a vapor transport route on SiO_2/Si, by Bi_2Te_3 sublimation and recrystallization. The NPTs grow along the (0001) plane, as the underlying Si. The presence of Te aggregates and pinholes suggests the formation of a Te-rich vapor during Bi_2Te_3 sublimation, promoting the phase segregation. Initially, Te condensation on the SiO_2 leads to the formation of Te nucleation seeds where the BiTe and Te_2 meet to react. Before crystallizing, Te species can penetrate on the amorphous SiO_2 reaching the Si substrate, where they will be epitaxially attached.

4.6 Conclusions

We have extended our polarity study to some 2D-like nanostructures as nanobelts, nanosheets, nanosails or V-shaped membranes. Interestingly, crystalline defects have a remarkable role in the growth and properties of these structures.

The ZnTe nanobelts and sheets analyzed show an excellent crystal quality, which is reflected in the optical measurements performed. As a proof of fact, PL spectra acquired on the structures show up to 7th order longitudinal optical phonon emissions at room temperature. Both morphologies were found to differ mainly on the peak intensity, being the emission stronger for the nanobelts case compared to the nanosheets.

Regarding the crystalline defects, on one hand, the nanosail formation is driven by the occurrence of a twin boundary, opening the way to the lateral expansion of the structure. The measured electron mobilities for the InSb NSs are four times larger than the best reported value for an equivalent system, evidencing the superior electronic quality of the sails. In addition, the conductance analyses reveal 1D type transport along the sails, only reported until the date in 2 DEGs, but not in free-standing InSb systems. On the other hand, the preferred polar growth following divergent directions, as it happens in the V-shape membranes, gives rise to the formation of an inversion domain boundary at those regions where the wings merged together. Huge implications are expected for the carrier transport in presence of inversion domain boundaries, based on the performed first-principles calculations on the electronic structure and conductivity.

Lastly, we include the example of Bi_2Te_3 nanoplates, illustrating a non-polar growth case which surprisingly grow after the formation of a Te nucleation seed embedded on the thick SiO_2 layer covering the substrate, while Bi is restricted to the nanoplate.

CHAPTER 5

Nanowire Heterointerfaces at Atomic Scale

5.1 Introduction

5.1.1 Heterostructures, Mismatch and Strain

Nanoengineering has emerged as a powerful branch of materials science, focusing on the design and growth of materials with advanced functionalities at the nanoscale. The miniaturization itself modifies the material bulk properties; but there are a lot of factors to play around. In this context, the creation of interfaces where different materials are connected allows exploring new material properties and physical principles.

The creation of such interfaces is achieved by the epitaxial growth of one material over another. If there are no matching planes connecting both phases, the interface is said to be incoherent while if there is a perfect matching between both phases through their atomic planes, the resulting interface is coherent. Intermediate situations with partial lattice matching and creation of dislocations are considered semi-coherent. Generally, coherent interfaces are required to ensure a high performance in the material electronic/photonic properties, since crystalline defects would act as non-radiative recombination centers and reduce quantum efficiencies. Moreover, the presence of inhomogeneous alloy compositions in ternary alloys, $A_xB_{1-x}C$, (i.e. $In_xGa_{1-x}N$) around dislocations has been recently shown [225]. This alloy segregation locally modifies the atomic arrangement and, therefore, affects the optoelectronic properties.

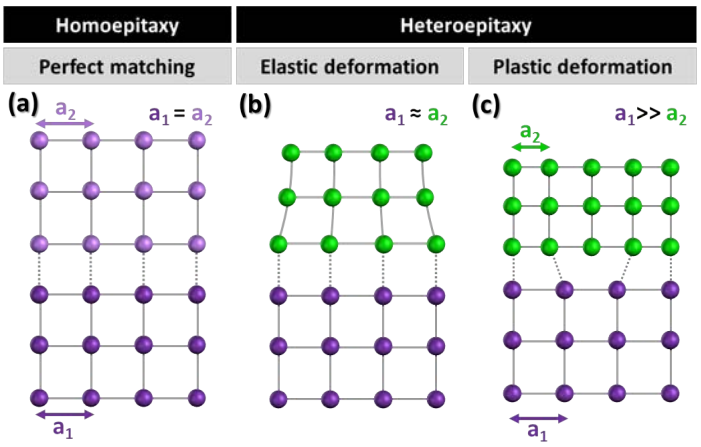

Figure 5.1: Possible lattice distortions while matching two phases in a (semi)coherent way. The homoepitaxial matching results on undistorted lattices (a), while heteroepitaxy induce lattice deformations, either elastically (b), for small mismatches, or plastically (c), for large lattice differences.

Whenever we couple two different phases coherently, the different lattice parameters or lattice mismatch would create strain fields inside the structure. The theoretical mismatch between two different phases can be calculated as follows:

$$\epsilon = \frac{a_2 - a_1}{a_1} \tag{5.1}$$

where a_1 and a_2 are the lattice constants of the considered materials, being 1 the former grown material and 2 the subsequent (epitaxied material). The related strain fields can be accommodated by the growing structure until some extent which will depend on the relative mismatch and on the obtained morphology, among other factors (e.g. the thickness of the epitaxied material). For large mismatches, dislocations will be created to allow the matching between both materials (see Fig. 5.1(c)). Predicting the dislocation spacing for a fully relaxed system is straightforward by considering the interatomic distances of matching planes. It should be noted that different epitaxial relationship could be achieved depending on the crystalline phase and lattice parameters of both materials, needing to take into account those distances for the dislocations spacing calculations (see Table 5.2). In bulk materials and 2D systems, a strictly coherent interface can be achieved only for homoepitaxial systems or really low mismatches (<1%) as schematically shown in Fig. 5.1(a), but, nanoobjects (i.e. NWs), are able to accommodate much more strain thanks to their limited lateral dimensions, thus preserving the interface quality.

One remarkable advantage of the NWs geometry is the possible switching from axial to radial growth mode by adjusting the growth parameters. This allows the creation of axial or radial heterostructures when combining different materials within the same NW. Axial heterostructures will be created when stacking different materials along the NW axis while radial or coaxial combinations will be formed when one material grows around the NW facets (lateral growth on the NW sidewalls). Such combinations tune the band gap of the connected materials, allowing tailoring the absorption/emission of the structure in the desirable way. Due to their morphology, NWs have been extensively shown as ideal candidates for the combination of highly mismatched materials since their large aspect ratio provides enough surface/area to effectively release the mismatch strain laterally over short distances from the interfaces [34, 226, 227], preserving the interface quality. In fact, theoretical models predict the capability of NWs to keep the coherency for radius about one order of magnitude larger than the dimensions required for the equivalent planar system [228]. Therefore, the heterostructures will be elastically strained but remaining coherent at the interface for small NW radii; although for radii above a critical value (system dependent), misfit dislocations may be energetically favored. {111} dislocations are usually observed in fcc crystals growing along the ⟨111⟩ or ⟨110⟩ directions. Such defects have edge and screw components, but only the edge one relaxes the mismatch strain. For the particular case of the NWs, pure edge

dislocations can be considered as the gliding plane is coincident with the interface and reaches the NW surface. Associated with the NW radii, there is a dependent critical thickness of the epitaxied material below which dislocations would not show up. For infinite layer thicknesses, a threshold radii ensuring the coherency can be calculated [229]. The obtained critical values are dependent on the mismatch of the system, as shown in Fig. 5.2. Note that for heterostructures with lattice differences larger than 3%, dislocations are expected for radius above 25 nm. Other reported calculations follow the same trend, although resulting in even more restrictive coherency limits, where NWs with radii five times larger than the dimensions of the same material system under 2D morphology, do not reach the plasticity limit yet [230].

Material	**Crystal Structure**	**Lattice Parameters (Å)**	**(*hkl*) d_{hkl}(Å)**
GaAs	ZB	a = 5.6535	(*111*) 3.264
*GaAs	WZ	a = 3.9976, c = 6.5281	(*0002*) 3.264
InAs	ZB	a = 6.0600	(*111*) 3.499
*InAs	WZ	a = 4.2851, c = 6.9975	(*0002*) 3.500
GaSb	ZB	a = 6.0959	(*111*) 3.519
InSb	ZB	a = 6.4800	(*111*) 3.741
GaN	WZ	a = 3.190, c = 5.189	($1\bar{1}00$) 2.763
InN	WZ	a = 3.545, c = 5.703	($1\bar{1}00$) 3.070
Si	ZB	a = 5.4286	(*111*) 3.134
Ge	ZB	a = 5.6580	(*111*) 3.267

Table 5.1: Crystalline phases and lattice parameters of the materials studied. * WZ lattice paramters calculated based on the ZB ones, following the ecuations 3.1.

On one hand, strained materials show modified properties compared to relaxed systems [231]. On the other hand, the strain relaxation will take place elastically through

Materials & planes	Mismatch	Misfit spacing (Å)	planes between misfits
$(\bar{1}1\bar{1})$ InAs (ZB)/ $(\bar{1}1\bar{1})$ InSb (ZB)	6.9 %	54	14-15 InSb / 15-16 InAs
$(\bar{1}1\bar{1})$ $InAs_{0.85}Sb_{0.15}$ (ZB)/ $(\bar{1}1\bar{1})$ InSb (ZB)	5.5 %	64	17 InSb/ 18 $InAs_{0.85}Sb_{0.15}$
$(\bar{1}1\bar{1})$ GaAs(ZB)/ $(\bar{1}1\bar{1})$ GaSb(ZB)	7.8 %	46	13 GaSb / 14 GaAs
(0002) InAs(WZ)/ (0002) GaAs(WZ)	-6.7%	49	15 GaAs / 14 InAs
$(1\bar{1}00)$ InN(WZ)/ $(1\bar{1}00)$ GaN(WZ)	-11.1%	27	10 InN / 9 GaN
(111) Si/ (111) Ge	-4.1%	77	23-24 Ge/ 24-25 Si

Table 5.2: Calculated mismatches and predicted spacing between dislocations in Å and number of planes.

plane bending, as shown Fig. 5.1(b), which changes the band alignments [232–236], and/or plastically by the formation of interfacial misfit dislocations, illustrated in Fig. 5.1(c) (and, thereby, creating semicoherent interfaces).

However, experimental evidences of dislocated heterointerfaces in NWs are scarcely reported for both, axial [32,52,237] and radial systems [56,238] on binary combinations, while most published works neglect their presence [212,239–244]. Since the existence of misfit dislocations will influence the final material properties in different ways [4], their detection becomes extremely important and detailed characterizations at atomic level of such interfaces are highly desirable.

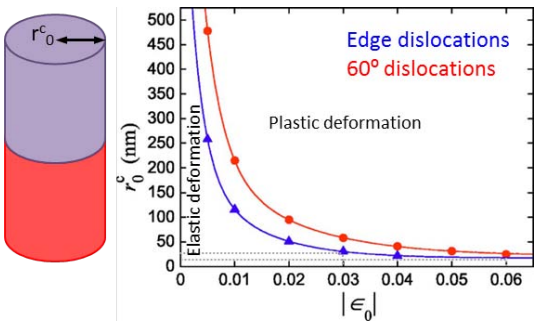

Figure 5.2: Coherency limits in terms of the critical radius of the NW, r_0^c, and the mismatch, ϵ_0, under two considerations: creation of edge dislocations (blue) or 60° dislocations (red). Adapted from ref. [229].

A common route employed to create binary heterostructured NWs is switching the anion/cation source while keeping the cation/anion one. However, the growth of high crystal quality heterostructured NWs is challenging, especially for cation switching synthesis processes when using metal seed particles (mainly gold). Anion switching has also potential drawbacks: the high solubility of the group-V anions in the catalyst promotes the reservoir effect which can result in kinking and graded interfaces [32], having detrimental implications for the later use of the synthesized structure. Then, addressing the abruptness of the interface and possible ternary compound formation is also extremely important. This is especially true for Sb, which is also a known surfactant, changing drastically the interface energy balance at the droplet/NW interfaces. Similarly, in the case of elemental semiconductors, composed by only one atom specie, binary combinations can be created at the heterojunctions. Thus, along the chapter, we carefully inspect the herojunctions, not only for the possible defect location but also to establish the sharpness of the interfaces.

In the following, a variety of heterostructured NWs; including examples of anion and cation exchange interfaces under axial or radial configurations, are analyzed in order to show how the misfit strain is released in those systems. The considered systems contain combinations of III-V semiconductors. In all the cases here explored, the heterojunctions are created by combining isomorphic materials sharing orientation. The case of coaxial or radial heterojunctions is illustrated by analyzing the InAs@GaAs system, while a variety of combinations account for the axial configuration. We will distinguish among those examples involving complex interfaces(GaN/InN, GaAs/GaSb) and those showing imtermixing and diffusion phenomena (InAs/InSb).

In order to analyze the strain relaxation mechanisms at different semiconductor heterostructure NWs, we analyzed the materials under high resolution conditions. This is done either by conventional HRTEM or by aberration-corrected HAADF techniques, since the only requirement on the image is the presence of Bragg spots in the Fourier transform (therefore, lattice fringes should be visible at the micrographs). The obtained data is processed by means of Geometric Phase Analyses (GPA), as explained in Section 2.4

5.2 Strain Relaxation Mechanism in Heterostructured NWs

5.2.1 Partial Strain Relaxation: Radial InAs@GaAs

The InAs@GaAs core@shell NWs analyzed in this section have been grown by a VLS procedure using a gold droplet guiding the growth. Such droplet remains attached to the tip of the NWs as evidenced the images taken at the wires by means of SEM and

(S)TEM related techniques (an example of a low resolution STEM image is shown in Fig. 5.3(a)). The NWs grow perpendicular to the InAs ⟨111⟩B substrates employed, where the Au droplets are initially deposited. Then, the system is fed with the required gas precursors which will be incorporated to the Au, where they will precipitate creating the NW. Slight different temperatures are needed for the formation of the InAs and GaAs, being 400°C for the former while it is 380°C for the shell. Also the time for the core and shell growths are different, since the thin shell deposited (around 2 nm thick) only requires 100 s deposition while growing the inner cores takes 55 min.

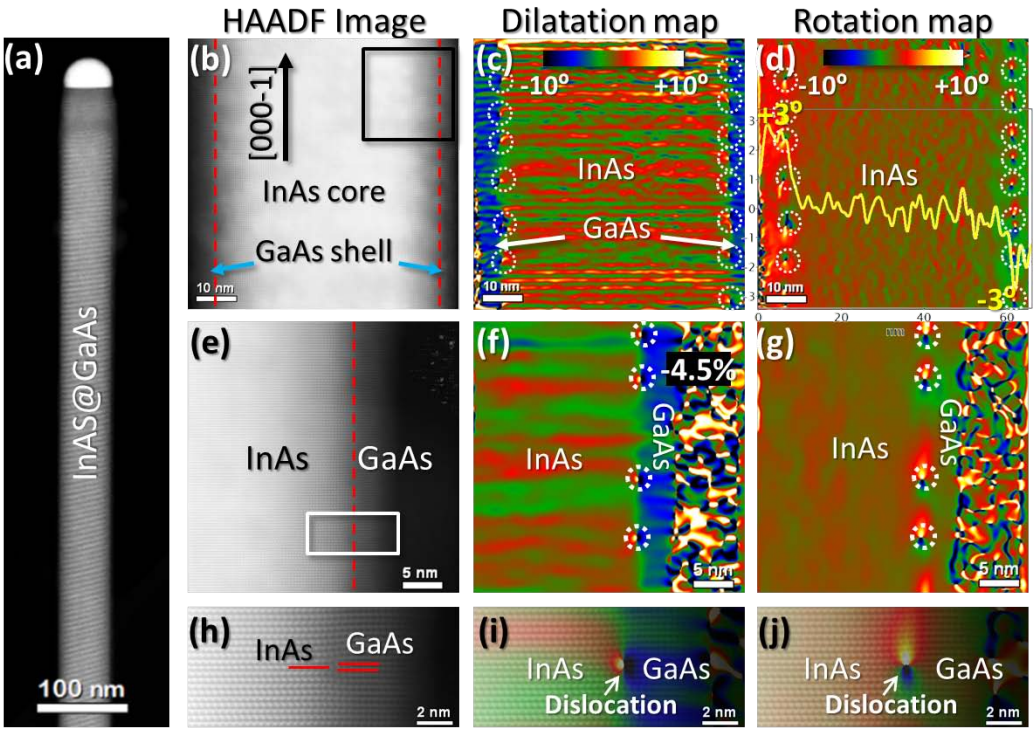

Figure 5.3: (a) Low magnification HAADF image of one InAs@GaAs NW. Atomic resolution HAADF image of the entire diameter of the NW (b) , and the corresponding GPA dilatation (c) and rotation (d) maps obtained by analyzing the (0002) growth plane. (e-g) Zoom into the black squared region in (b) and GPA study performed at higher spatial magnification (f,g). The white framed area in (e) is displayed magnified in (h), while (i) and (j) shows the superposition of (h) with the corresponding dilatation and rotation maps.

The GaAs shell adopts the WZ phase mimicking the InAs core, which grows along the $[000\bar{1}]$ direction. Although it is hard to be distinguished at naked eye, the interface location is clear at the obtained GPA maps calculated by analyzing the (0002) plane (growth plane), shown in Figs. 5.3 and 5.5. The presence of "8"-like features at both, dilatation (Fig. 5.3(c,f)) and rotation maps (Fig. 5.3(d,g)), decorating the whole heterointerface correspond to the locations of misfit dislocations, distributed along the

entire length of the NW. A further detail to be mentioned concerns the stacking faults induced by the misfit dislocations. As a closer look at the structure reveals, the extra atomic plane inserted at the GaAs phase at every dislocation leads to the formation of ZB domains within the shell, localized at the exact misfit positions (see Fig. 5.3(h-j)). These punctual stacking faults are in fact needed to preserve the rest of the shell growing coherently, following the pristine InAs WZ structure, as illustrated in Fig 5.4.

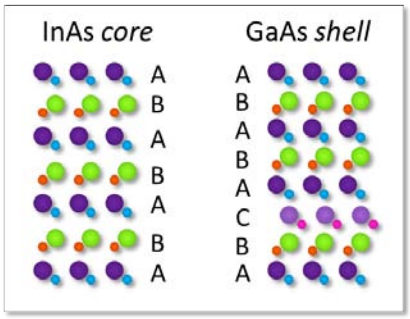

Figure 5.4: Matching of the axial stacking sequences of core and shell in the InAs-GaAs NWs.

The dislocated interface separates two noticeable regions in terms of the d spacing of the (0002) planes, shown in Fig. 5.3(c). The dramatic change from the neutral red-green color shown by the $d_{(0002)}$ InAs core, where the GPA reference was chosen, to a deep blue at the GaAs shell is correlated to the smaller lattice parameter of the GaAs versus the InAs (see tables 5.1 and 5.2). Analyzing the interface in more detail, we can quantify the lattice difference at both sides, resulting in a 4.5% compression of the GaAs growth plane compared to the InAs, as shown in Fig 5.3(f). This value is in agreement with the observations reported in ref. [238], where authors find a 4% of mismatch along the growth plane when analyzing the same type of heterostructures. However, this difference in the growth plane spacing when comparing core and shell does not reach the theoretical mismatch value between the phases involved.

To complete the study, we model the NW system, considering completely relaxed phases at both sides of the interface, but neglecting the elastic lattice distortion, thus, accounting only for the plastic relaxation. A picture of the created 3D model is shown in Fig. 5.5(g), displayed at two different radii scales, to enhance the atomic matching (left panel) and the 3D geometry (right panel). The cell parameters considered in the 3D atomic models are those included in table 5.1. The simulated images obtained of the InAs@GaAs core@shell (shown in Fig. 5.5(d)) and the corresponding strain maps (Fig. 5.5(e,f)) indicate that such heterojunction requires presence of misfit dislocations every 4.9 nm to completely relax the induced strain by the 7.2% mismatch among them.

This mismatch difference between experimental and theoretical data (see Fig. 5.5)

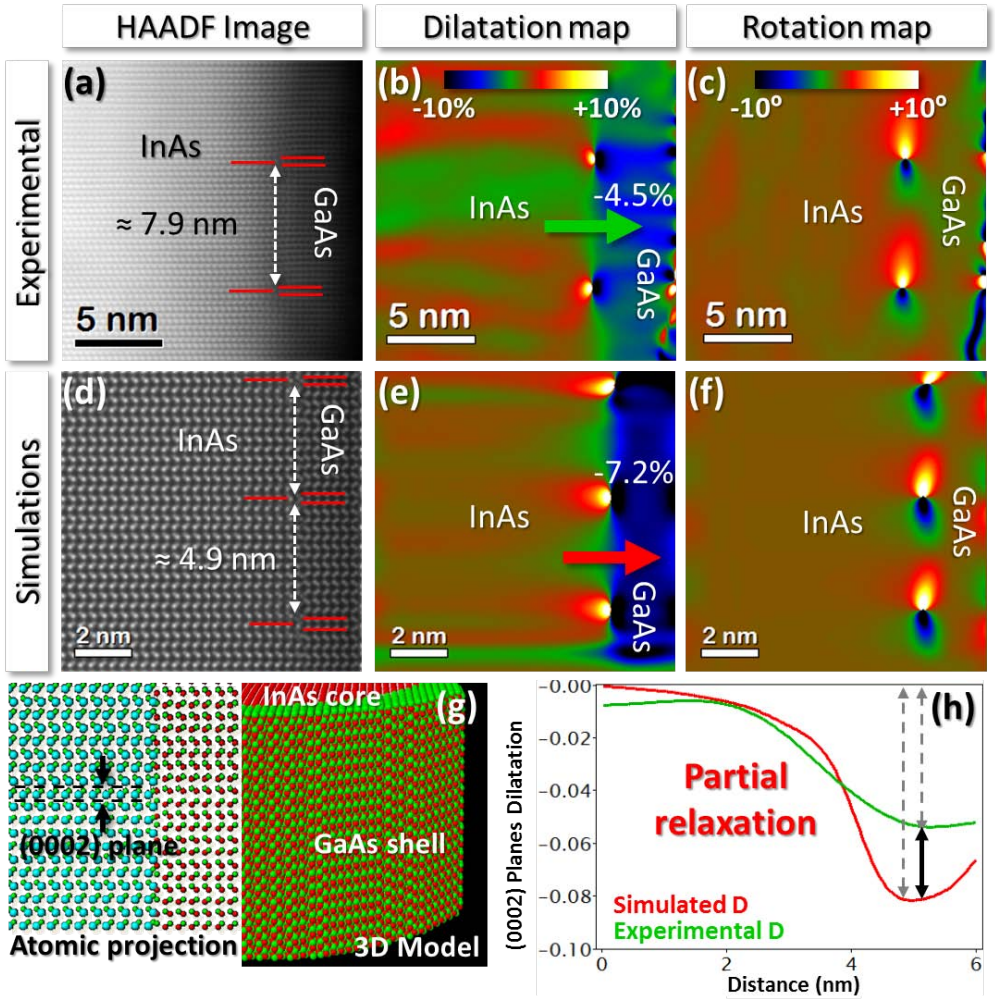

Figure 5.5: (a/d) Experimental/Simulated atomic resolution HAADF image of the InAs-GaAs interface, with dislocations 7.9/4.9 nm apart. The corresponding dilatation and rotation GPA maps calculated on the (0002) plane are displayed in (b/e) and (c/f), respectively. (g) 3D Atomic model used for the simulations (right side) and its projection along the $[11\bar{2}0]$ direction. (h) Intensity profiles taken the green/red arrows in the dilatation maps (b/e), evidencing differences between the experimental and the simulation, suggesting a partial relaxation of the strain within the system.

implies that the d_{0002} spacing of the GaAs shell is still 2.7% larger than its theoretical value, meaning that the shell is tensile strained due to its epitaxy with the larger lattice of the InAs core. By comparing intensity profiles taken across the experimental and simulated interfaces, the partial relaxation becomes more evident (see Fig. 5.5(h)). It should be mentioned that a symmetrical plane bending of $\pm 3^{o}$ was detected at the shell when analyzing the rotation map of the growing plane, representing the upwards/downwards plane bending at the GaAs region. This fact is highlighted by the intensity profile taken across the rotation map and yellow displayed superimposed to the map in Fig. 5.3(d). Although the plane bending partially accounts for the strain relaxation (elastic relaxation), the GaAs structure is still strained as deduced from its larger cell that does not reach its characteristic value.

5.2.2 Completely Relaxed Systems: Complex Axial Interfaces

Along this section we will present examples of abrupt axial heterointerfaces in a NW. We will consider systems with cation or anion exchange interfaces where the formation of graded interfaces has been completely avoided, analyzing the role of geometrical factors. We will demonstrate the importance of the cell symmetry along with the interface morphology for a proper interpretation of the experimental data. The studied systems are GaN/InN NWs as an example of cation exchange interface and GaAs/GaSb NWs to address the case of anion exchange interface.

Axial GaN/InN

GaN NWs are first grown on Si substrates, as stems for the late growth of InN on top, creating the axial GaN/InN heterojunction, by using the PAMBE procedure. Neither Si diffusion into the NWs, nor Ga diffusion on the Si substrate were detected by EELS measurements, as shown in Fig. 5.6(c). The observable N enrichment at the substrate surface is due to the nitridation step required to prevent the formation of a GaN wetting layer [124], resulting in a Si_xN_y amorphous layer, 2.3 nm thick in the present case. Thus, mismatch constrictions dictated by the substrate usually involved in the epitaxial growth are avoided, although the NWs are still aligned with the underlaying crystalline substrate. Crystalline pinholes penetrating the amorphous layer mediate the observed alignment. The resulting NWs have hexagonal cross-section faceted by $\{1\bar{1}00\}$ planes. Both materials involved grow under the hexagonal WZ crystalline structure along the $[000\bar{1}]$ direction. It is noteworthy the surface oxidation of both nitrides, especially remarkable in the indium section (as evidenced in the EELS maps in Fig. 5.6(b)), where we can even identify one In_2O_3 nanocrystal on the InN sidewalls. The pattern resulting from the fringe overlapping between the In_2O_3, with $Ia\bar{3}$ space group, and the InN, with $P6_3mc$ WZ structure, is displayed in Fig5.7. By properly filtering separately the bragg reflections in the FFT of the phases involved, as indicates the inset in Fig. 5.7(a), we

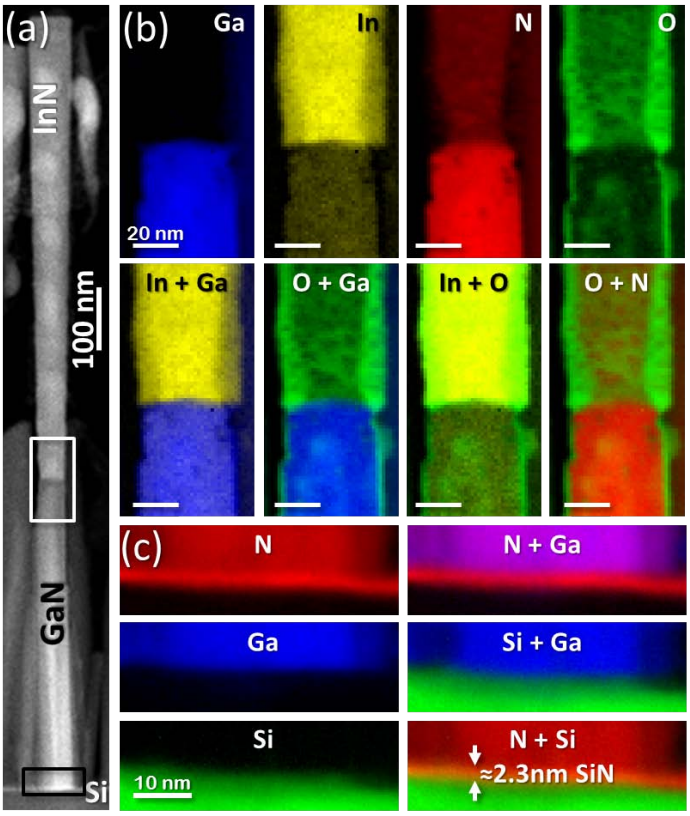

Figure 5.6: (a) HAADF image of an entire GaN/InN NW on Si. (b/c) EELS maps of the GaN-InN inteface/GaN-Si substrate interface white/black squared in (a). Color code: we display the Ga signal in blue, the In in yellow, the N in red and green is used for O (b) and Si (c).

can extract filtered images of the InN (Fig. 5.7(d), indicated in green at the FFT) and In_2O_3 (Fig. 5.7(e), in red) isolated structures. Superimposing the two filtered images results in the composition included in Fig. 5.7(f), showing the same atomic pattern as shown in the experimental atomic resolution HAADF image in Fig. 5.7(c), also in great agreement with the HAADF image simulation performed (inset on Fig. 5.7(c)). The advantage of the image composition over the raw HAADF image is that allows identifying the two phases contributing to the final pattern. Thus, it is clear from the EELS measurements and the atomic resolution data that the outer surface of the NWs is oxidized, widely known to occur in certain materials.

The high resolution images taken at the heteroninterface between the GaN and InN reveal a non-flat growth front (see Fig. 5.8(a,i)). The materials are connected through a smooth bended interface, plenty of misfit dislocations. Before going deeper on the strain analyses, note that for both phases, GaN WZ and InN WZ the c/a ratio deviates from the ideal value of $\sqrt{\frac{8}{3}}$, in different amounts. In the GaN structure such lattice constant

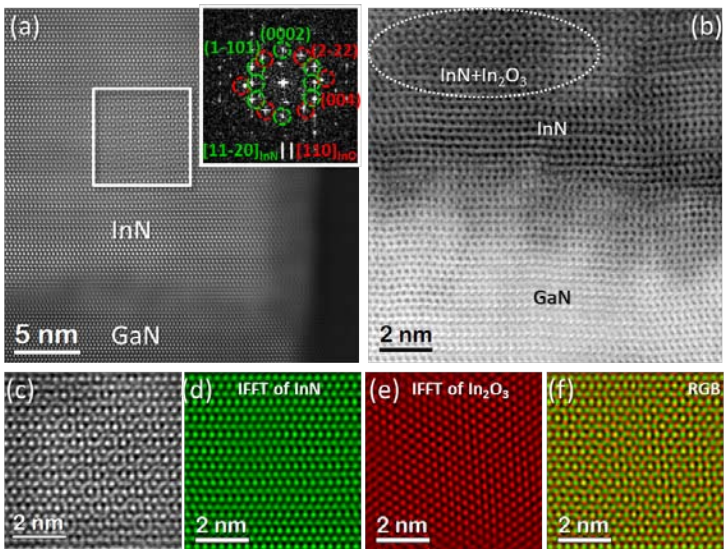

Figure 5.7: (a) HAADF image of GaN/InN interface. The FFT inset corresponds to the white squared region, where the In_2O_3 and InN structures overlap. Bragg reflections from the InN are encircled in green and In_2O_3 in red. (b) Atomic resolution ABF image of the squared region in (a). (c) Magnified detail of the atomic pattern resulting from the superposition of InN and In_2O_3 lattices. The simulated HAADF image is included as inset in (a). (d-f) IFFT of the InN and In_2O_3 structures and their addition.

relationship is 1.627, which is really close to the ideal value (1.633), while in InN such ratio is only 1.609. Thus logically leads to different misfit values along a and c, being 11.1 % and 9.9 % for a and c, respectively. As the $(000\bar{1})$ planes are stacked along the growth direction, (i.e., the NWs grow along the $[000\bar{1}]$) dislocations will not be formed within these planes. Contrary, the vertical $(1\bar{1}00)$ and inclined $(1\bar{1}01)$ family planes connecting the gallium and indium nitrides, necessarily generate misfit dislocations at the interface to match both structures, as shown in Fig. 5.8. The figure also includes the lattice experimental deformation obtained by applying GPA, displayed in terms of the d spacing variation (upper row in Fig. 5.8) and plane rotation (middle row in Fig. 5.8) of the $(1\bar{1}00)$, $(000\bar{2})$ and $(1\bar{1}01)$ planes, referred to the GaN lattice. The continuity of the matching planes is clearly broken at the interface where the dislocation cores are located, following the bended growth front morphology (Fig. 5.8(i)). We can asses from the beginning the presence of dislocations just by looking at the fast Fourier Transform, where two sets of bragg reflections are distinguishable (yellow and white indexed in Fig. 5.8(b)) for the InN and GaN, respectively), indicating two different lattice parameters for the two materials. The 11% difference on the $(1\bar{1}00)$ planes experimentally found is indicative of the total lattice relaxation apart from the junction, as inferred by comparing with theoretical system mismatch (see table 5.2).

Interestingly, in addition to the dislocated interface, the $(000\bar{2})$ planes just below the

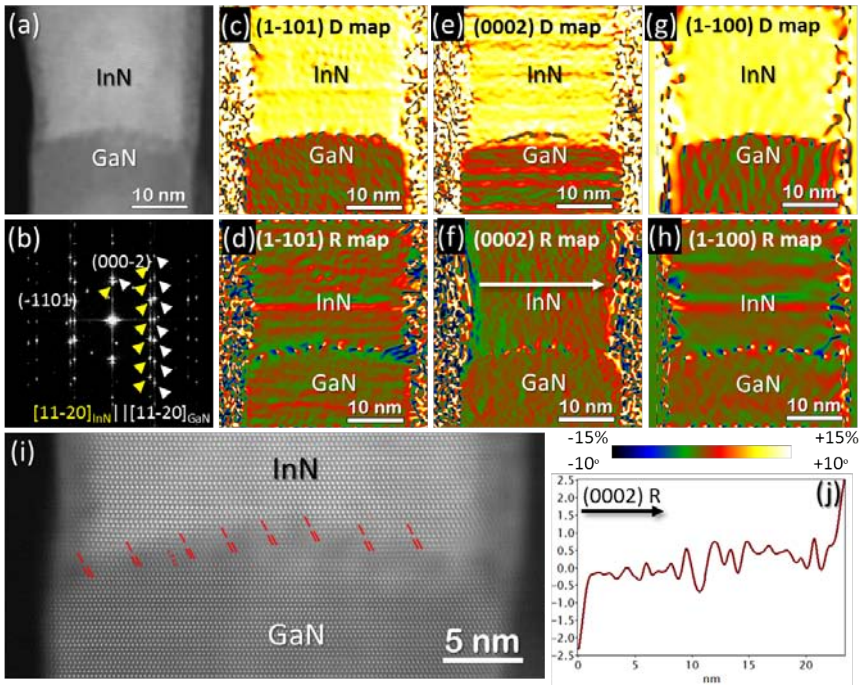

Figure 5.8: (a) HAADF image of the GaN/InN interface. (b) FFT of (a). (c/h) GPA maps obtained from the $(1\bar{1}01)$, (0002) and $(1\bar{1}00)$ for (c-d), (e-f) and (g-h), respectively. Top maps show the changes on the plane spacing while bottom row represents the plane rotation. (i) Magnified detail of the interface pointing the dislocations in the $(1\bar{1}01)$.(j)Profile taken at the rotation map of the (0002)plane following the arrow in(f).

growth front curvature are highly expanded (almost 9%) in the supposed GaN region. Unfortunately, the origin of such distortion becomes elusive. It should be noted that In atoms under the electron beam show really high mobility, but any In diffusion across the heterointerface would deform the lattice in other directions, which we do not observe. Moreover, the graded interfaces should be visible at naked eye in the Z-contrast images or apparent on the EELS maps. Similarly, postulating a slight radial overgrowth of the InN around the GaN at the junction, and focusing close to the InN, we would see differences in all the planes considered, which is not the case. Just by taking into account the blunt interface morphology, InN and GaN lattices may overlap each other around the considered area, blurring the $(000\bar{2})$ plane and giving a possible explanation. Complex out-of-plane strain distributions have been already reported in these heterostructures, which show twisted atomic arrangements at the interface resulting in modulated interfaces [245]. Another issue to point out is the growth plane rotation through the edges at the InN section, where the (0002) planes are symmetrically rotated up to 2.5°, as highlighted in Fig. 5.8(j), with the growing planes adapting to the interface morphology and elastically releasing residual mismatch strain.

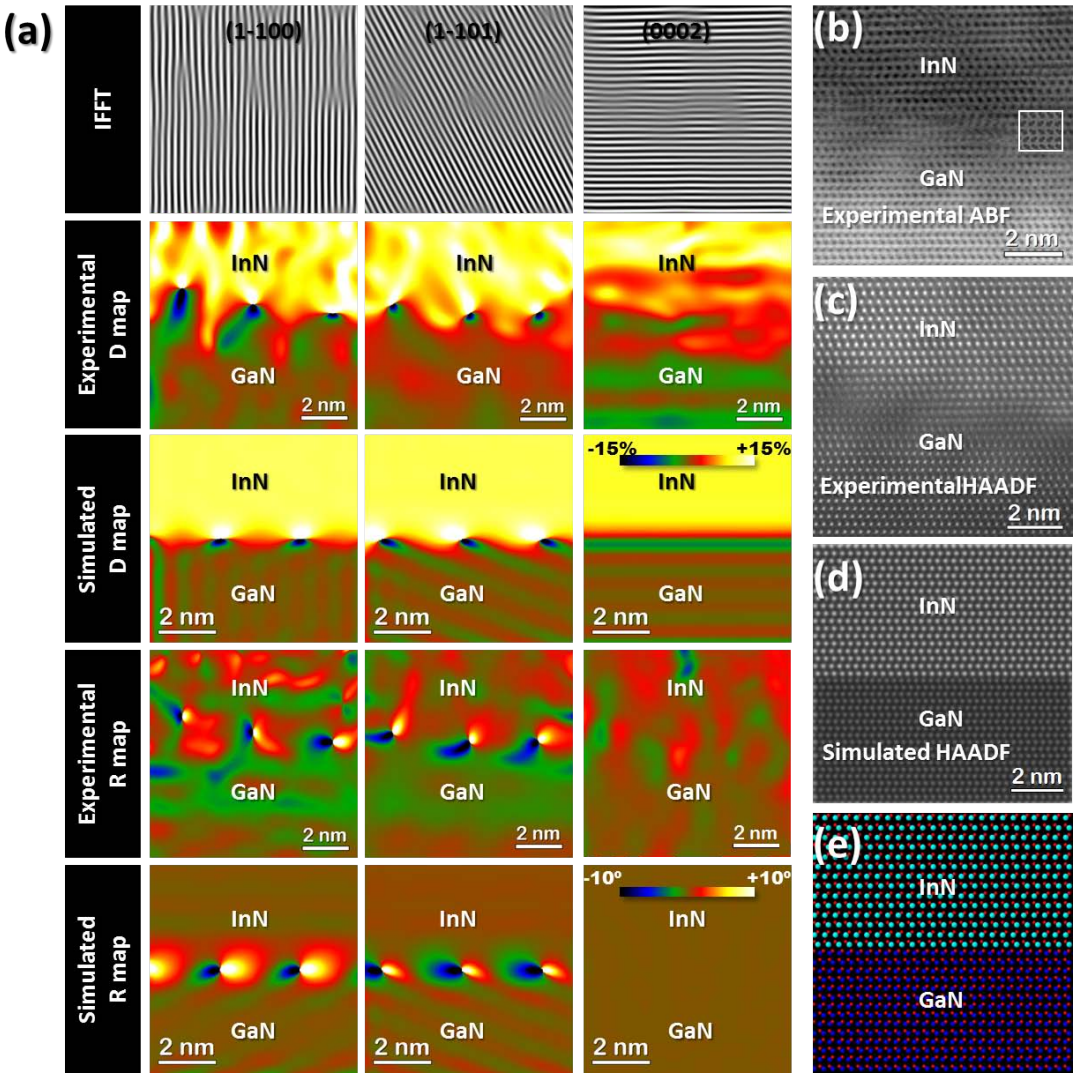

Figure 5.9: (a) GPA maps extracted by analyzing the $(1\bar{1}00)$ (first column), $(1\bar{1}01)$ (middle column) and (0002) (right column) planes, including experimental and simulated maps. (b/c/d) Experimental ABF/HAADF image/simulated HAADF image of the GaN/InN interface. The overlapping inset corresponds to the simulated ABF image. (e) Atomic model used to obtain the simulated data created by Rhodius.

We have analyzed the interface at higher magnification, paying attention again to different dislocated family planes, i.e.; $\{1\bar{1}00\}$ and $\{1\bar{1}01\}$, as well as to the $\{0002\}$ growth plane. Fig. 5.9(a) displayed the resulting deformation GPA maps along with the maps obtained when performing the same analyses in a simulated model completely relaxed, neglecting the elastic relaxation and morphological constrictions of the interface; that is, with a flat interface instead of curved. The different planes analyzed show different misfit location along the NW diameter, as expected from the already mentioned mismatch discrepancies along the different directions, but also they appear axially shifted. The misfit distribution along the radial direction is in good agreement with the simulated model, as it accounts for the mismatch between structures; however their axial location is underestimated in our simple model as consequence of the flat phase transition chosen. Again, the interface curvature observed in the 2D projected images, which is actually a convex surface, should be taken into account. Considering this fact, the dislocations will appear at different heights due to the location of the $(1\bar{1}00)$ and $(1\bar{1}01)$ dislocations at different depths and, therefore, corresponding to different axial coordinates on the interface surface. As in the general strain maps, dilatation of the (0002) planes happens through an intermediate stage at the interface, possibly coming from the overlapping of both phases, as previously suggested.

Therefore, we have shown that GaN/InN axial heterostructures in a NW release the mismatch strain totally by creating a net of misfit dislocations which extends over the entire surface of the chemical phase transition. Considering the interface morphology, which is not flat but bended, and accounting for the different c/a ratio of the materials involved, we can achieve a better understanding of the misfit distribution within the interface.

Axial GaAs/GaSb

Arsenide and antimonide compounds show outstanding optoelectronic properties that make them suitable for integrating in a variety of advanced devices [32], including high speed electronics, long-wavelength optical devices [246], single photon emitters [62], room temperature lasers [247, 248] or photovoltaic cells [249]. Moreover, antimonide compounds show the narrowest bandgap, the highest electron/hole mobility (InSb/GaSb, respectively), the largest Landé g-factor [250] among binary semiconductors, as well as a strong spin-orbit coupling, being ideal candidates for the study of basic physical principles in condensed matter such as Majorana fermions [27, 28]. But, as already discussed, their properties and performance will be highly influenced by the presence of strain fields and structural defects.

Among the different arsenide/antimonide possible combinations, we start by analyz-

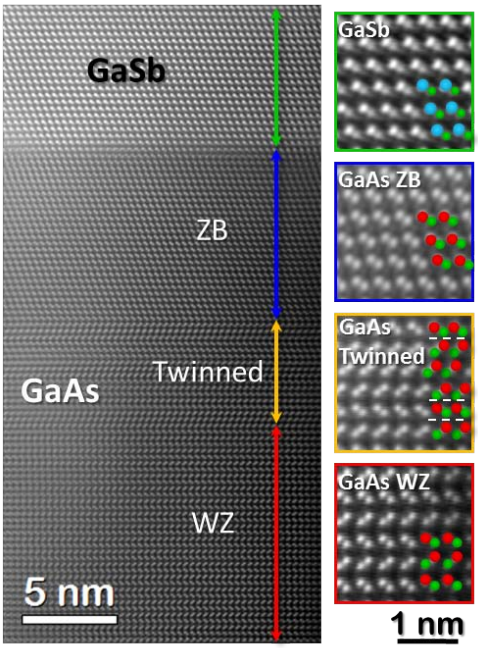

Figure 5.10: Atomic resolution HAADF of the phase transition from pure GaAs WZ to pure GaSb ZB. Right panels displayed magnified details of the different areas.

ing a heterostructured system rarely synthesized under the NW morphology: GaAs/GaSb [239,241]. The growth begins by creating the arsenide stems (GaAs) for the later growth of the antimonide counterpart (GaSb) on their top. The final NWs show hexagonal cross-section bordered by non-polar {110} planes and present spherical particles on their tips, consequence of the vapor-liquid-solid (VLS) mechanism governing the NW growth. The arsenide and antimonide regions are easily distinguishable by their different contrast in the HAADF images. The GaAs stems have pure WZ structure, as usual, growing along the $[000\bar{1}]$ direction (As-polar) while the GaSb grows with pristine ZB structure along the $[1\bar{1}\bar{1}]$ direction, being also anionic polarized (Sb-polar). The phase transition from WZ to ZB takes place before the chemical interface, meaning that the last GaAs nanometers already have ZB structure, being the $(1\bar{1}\bar{1})$ the growth plane as shown Fig. 5.10. Thus, the epitaxial relationship between both materials can be written as follows:

$$(1\bar{1}\bar{1})[110]_{GaAs} || \ (1\bar{1}\bar{1})[110]_{GaSb},$$

where [110] direction is the used zone axis for the measurements. In order to account for the GaSb lattice accommodation on the top of the GaAs lattice, we analyze the $(\bar{1}1\bar{1})$ planes deformation, referred to the GaAs ZB lattice. The resulting dilatation and rotation maps highlight the interface shape, which is sharp but bended (Fig. 5.11-c-d). The curved interface could be the result of a drastic change on wetting configuration of

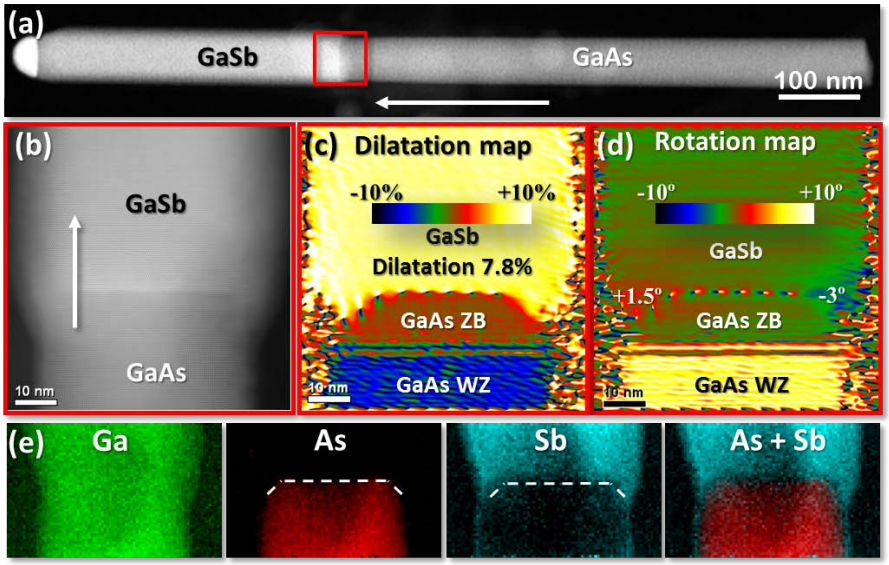

Figure 5.11: (a) Low magnification HAADF image of one GaAs/GaSb NW. (b) Aberration-corrected image of the interface, analyzed by GPA on the $(\bar{1}1\bar{1})$ plane. The white arrow indicates the growth direction. Dilatation and rotation maps are displayed in temperature color in (c) and (d), respectively. (e) EELS mapping of the Ga (green), As (red) and Sb (cyan) signals at the interface area.

the gold-containing alloy seed: due to surface energy differences occurring during the switching sequence and/or a change of its volume (from As to Sb), eventually the particle wets both sides of the GaAs stems, as inferred in other works [251, 252]. Truncation of the growth plane along the contact line between the NW and the catalyst has been observed in several semiconductor NWs [253, 254] allowing a deep characterization of the growth dynamics [165]. It turns out that supersaturation of the droplets drives the fast 1D growth on the {113} and {112} facets (which formation has been related to the growth temperature [255]) followed by a slower growth on the main ones [165]. Our spectroscopic measurements, performed by means of EELS, evidence the lateral (radial) growth of the GaSb around the last nanometers of the GaAs while growing the axial system (Fig. 5.11-e). Notice the truncation of the GaAs growth front, which has been filled by the GaSb grown afterwards. Thus, the interface of the NW can be considered as a core-shell interface (referred to its shape), where the core is formed by the GaAs (ZB) stem (bordered by {113}truncation planes) and the shell forms from the radial overgrowth of GaSb, explaining the interface morphology. A 3D atomic model of the NW is shown along different directions in Fig. 5.12.

Besides the interface curvature, the obtained GPA maps show an almost periodic array of singularities along the heterointerface, which positions correspond to the location of misfit dislocations. Apart from the interface, we find the GaSb lattice 7.8% expanded compared to the GaAs ZB reference area, in perfect agreement with theoret-

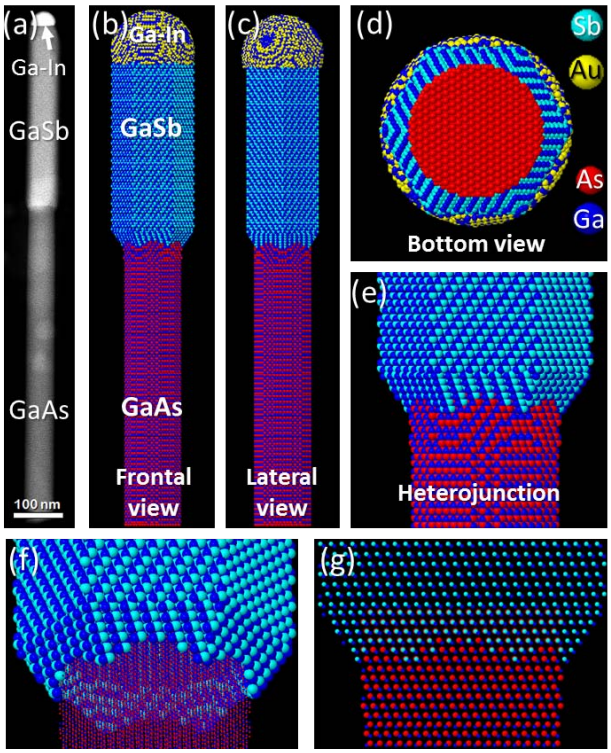

Figure 5.12: (a) Low magnification HAADF of one GaAs/GaSb NW. (b-g) 3D atomic model of the NW viewed along different directions. The core-shell-like morphology of the interface is clearly shown in (f-g). An animated movie of the 3D atomic model can be found at `http://gaen.cat/index.php/research/242`

ical calculations (5.2), meaning that the GaSb lattice is fully relaxed. Notice that the dislocation periodicity is broken through the edges of the NW where dislocations are more spaced (mainly on the right side of the present example), or even do not show up. Interestingly, at the interfacial region near the edges of the NW there is a noticeable plane rotation with opposite sign at both sides of the NW, compensating the lack of dislocations through elastic deformation.

A closer look at the heterostructure allows the visualization of the atomic columns making possible the misfit dislocation detection at glance (see Fig. 5.13-a). Analyzing the lattice distortion at higher magnification around the dislocations reveals that, despite the interface abruptness, the first 1-2 nm of the GaSb segment are slightly compressed. Comparing the experimental results with the simulations performed in a fully relaxed system, the small discrepancy is evident: while the simulated relaxed system acquires the characteristic GaSb lattice parameter immediately; experimentally, just after the dislocated interface, the first $\sim$ 1.5 nm of the GaSb are only 7% expanded reaching the 7.8% difference afterwards (Fig. 5.13-h). As a consequence, the mean experimental dilatation at the GaSb region near the interface is 7.6% (Fig. 5.13-b). Thus,

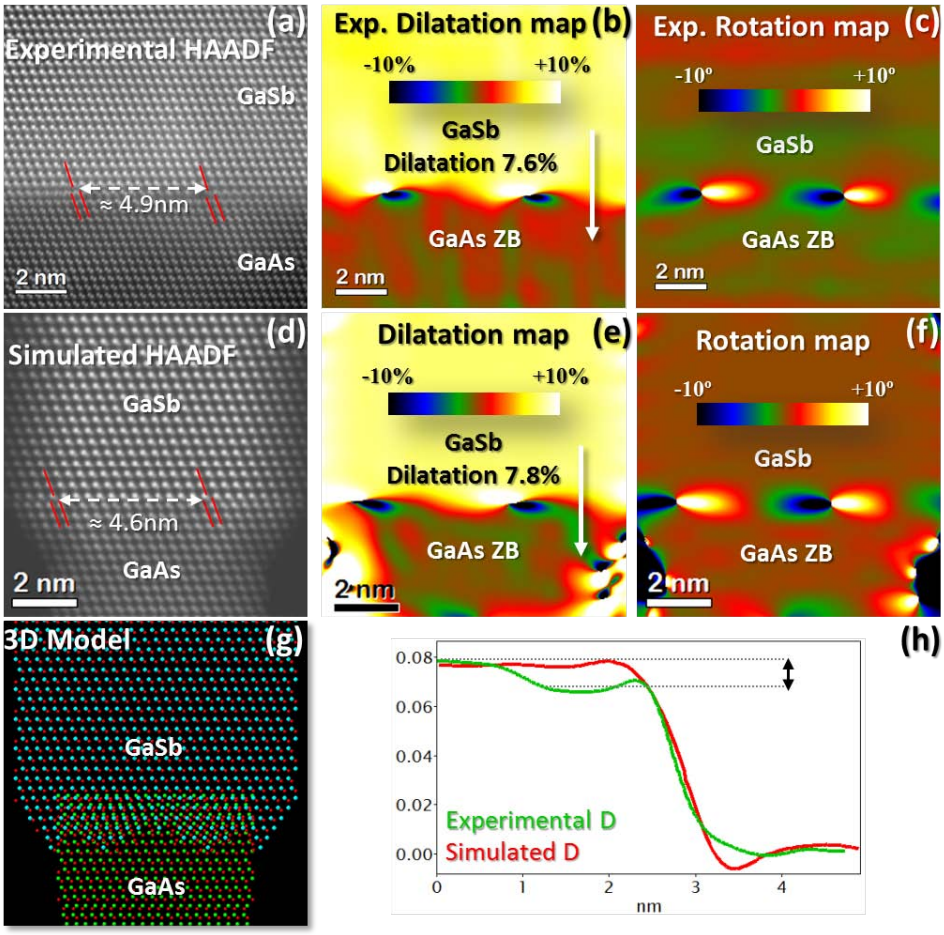

Figure 5.13: (a/d) Experimental/simulated HAADF images. The image simulation has been performed on a fully relaxed model, shown in (g). (b/e) Experimental/simulated GPA dilatation maps for the (-11-1)plane. (c/f) Experimental/simulated GPA rotation maps for the (-11-1)plane. (h) Profiles taken along the white arrows in (b) and (e), displayed in green and red, respectively.

the relaxation of the GaSb lattice takes place mainly through the formation of almost periodic misfit dislocations adapted to the convex shape of the interface, as in the case of the planar growth [256, 257]. Through the edges of the NWs, their filamentary morphology allows the partial elastic relaxation by plane bending decreasing the number of dislocations needed to accommodate the mismatch between both phases. The results are reported elsewhere in ref. [258].

5.2.3 Completely Relaxed Systems: Accounting for Intermixing and Diffusion

Until now, we have seen how the mismatch strain can be released in a NW when two materials are connected through chemically sharp interfaces. However, in some cases the undesirable formation of intermediate compounds at the interfaces can occur, as we

will see in the following. In addition to the cases of anionic/cationic exchange interfaces where the anion/cation can be diffused into the other side of the interface, heterosystems where the alloying composition is used to tune the sought properties are especially prone to show graded interfaces that should be investigated. Thus, continuing with the binary heterostructures, we will focus on the mechanism mediating the relaxation at InAs/InSb axial NWs [258].

Axial InAs/InSb

The next axial arsenide/antimonide NW example consists on indium based compounds. The heterostructures are created from the former growth of InAs NWs as template stems for the further growth of InSb on their top. Regarding their morphology, the NWs show hexagonal cross-section, faceted by equivalent $\{11\bar{2}0\}$ or $\{110\}$ planes (in the hexagonal and cubic phases, respectively). Despite the NW broadening when switching from InAs to InSb, the hexagonal section extends from the base to the tip, in contrast to other reported works on the same system, where the upper InSb hexagonal section is 30^{o} rotated respect the hexagonal section of the InAs stems [259], due to a different faceting for the InAs, i.e., $\{1\bar{1}00\}$ lateral facets. Such rotation can be used to explain the observed diameter broadening of the antimonide region, but this argument is not acceptable in our case since our NWs are hexagonal prisms from bottom to top, as evidenced by the intensity profiles taken along both regions (Fig. 5.14(b)). However, we can relate the diameter widening with the volume expansion of the catalyst droplet promoted by its compositional variation when switching the growth conditions and the In is uptaken [212, 213].

The droplets here observed are faceted by low index planes, in contrast to the GaAs/GaSb case where droplets were spherical. The particle is found to be purely $AuIn_2$ after cooling down, as expected if considering the ternary Au-In-Sb phase diagram, and shows an abrupt interface with the underlying InSb section. The 1:2 Au:In stoichiometry can be deduced from the aberration-corrected HAADF images, as every Au atomic column, much brighter than the In, is surrounded by two In columns, as shown Fig. 5.14(e) where the experimental image is displayed along with the simulated model. Moreover, we find that the particle matches perfectly with the InSb showing the following $(\bar{1}11)[110]_{AuIn_2}||(1\bar{1}1)[110]_{InSb}$ epitaxial relationship. No misfit dislocation are observed along the particle-NW interface, as expected for the low mismatch of the $AuIn_2/InSb$ system (0.4%) and the reduced dimensions of the interface. Note that the 0.4% lattice mismatch would induce dislocations 88 nm apart, while the width of the interface is roughly 50 nm.

Moving to the structural characterization, the InAs section crystallizes in the WZ

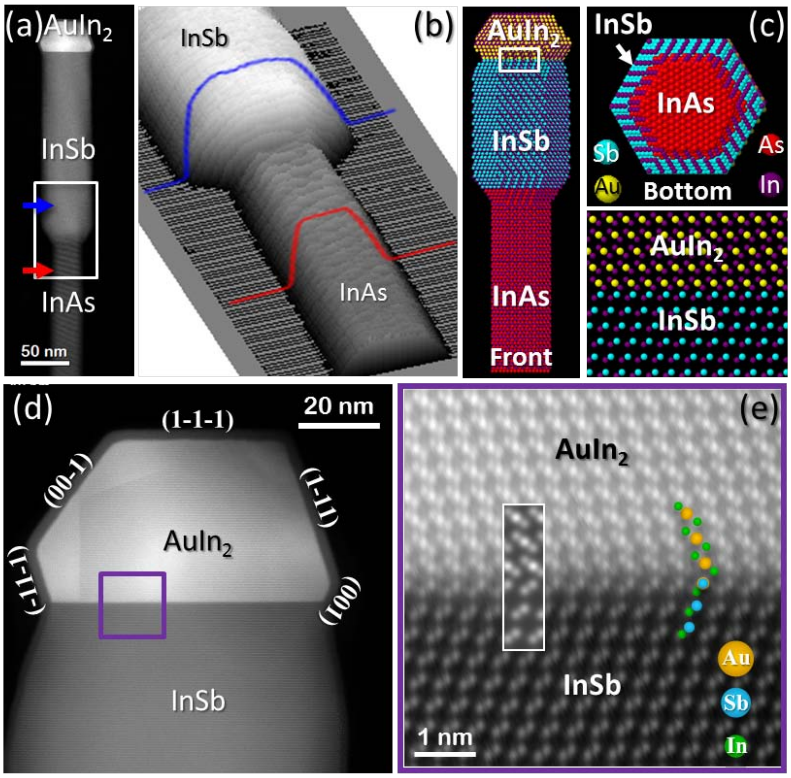

Figure 5.14: (a) Low magnification HAADF image of an InAs/InSb NW. (b) Intensity surface plot of the InAs/InSb heterointerface. Red/blue curve corresponds to the intensity profile taken along the red/blue arrow in (a).(c)3D atomic model of the NW viewed along different directions. An animated movie of the atomic model can be found at `http://gaen.cat/index.php/research/242`. (d) Low magnification image of the NW tip. (e) Atomic resolution HAADF image of the interface between the droplet and the InSb. The inset corresponds to the simulated images.

hexagonal structure [91] and grows along the $[000\bar{1}]$ direction (As-polar) and the InSb segment shows zinc-blende (ZB) cubic structure [91] growing along the $(1\bar{1}1)$ plane, which is Sb-polar (Fig. 5.15(b-d)). Thus, the anionic polarity (As or Sb) is preserved across the interface. Interestingly, when performing the strain measurements on the $(\bar{1}1\bar{1})$ ZB planes, we find the first 3-4 nm of the ZB region 5.5% compressed (Fig. 5.15(g)). Going from the interface to the tip, after these compressed 3-4 nm, the InSb recovers its characteristic lattice parameter and it becomes completely relaxed. The strain induced by the compressed region is suddenly released by the formation of misfit dislocations at about 3-4 nm from the interface, as shown in the GPA deformation map included in Fig. 5.15(g),(h). We can even detect them from the aberration corrected HAADF images, as shown in Fig. 5.15(f), where the vanishing of one $(\bar{1}1\bar{1})$ plane from the lower part of the NW can be observed. However, presence of dislocations is restricted to the central part of the NW, while the edges are defect-free even though based on the misfit spacing calculations (5.2) they are expected to show up. Instead,

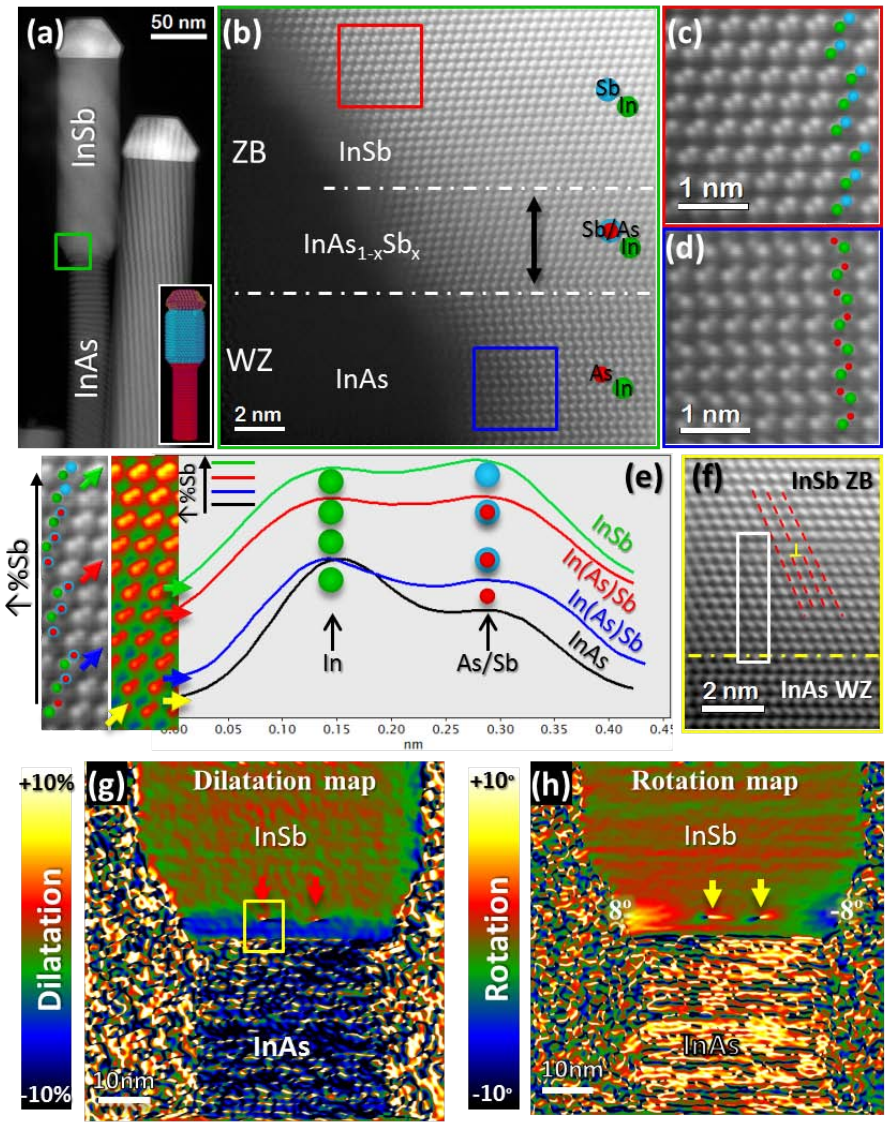

Figure 5.15: (a) Low magnification HAADF image of an InAs/InSb NW. (b) Atomic resolution HAADF image at the interfacial region. (c/d) Magnified details of the InSb ZB /InAs WZ structure, where the atomic columns have been identified, in agreement with an anionic growth front. (e) Intensity profiles along different dumbbells taken within the with squared area in (f). Atomic resolution HAADF image of around misfit dislocation. (g/h) Dilatation/rotation map obtained by applying GPA at the $(\bar{1}1\bar{1})$ planes of the ZB structure. Dislocations are pointed by arrows.

paying attention to the rotation map we can notice a clear symmetric plane rotation with opposite sign at both visible edges, which elastically releases the mismatch strain at those areas (Fig. 5.15(h)). Here, shape constrictions allow for the accommodation of such large strain, avoiding the formation of more dislocations by the release achieved through plane bending up to 8º.

If we consider the formation of pure InAs ZB before the transition to the InSb ZB (sharp interface), a 6.5% lattice difference, higher than the 5.5% experimentally found, would be expected, according to the simulations shown in Fig. 5.17(d-f). In order to elucidate the origin of the observed ZB compression and the location of the dislocation apart from the phase transition interface, we again take advantage of the chemical contrast offered by the HAADF [116, 260, 261] to identify the dumbbell constituents. We have already shown that both, the InAs stems and the InSb upper sections grow along the anion-polar directions, meaning that the In atomic column is always placed below thee As or Sb one. Thus, as the As intensity is dimmer than the In one for the InAs dumbbell (Z_{In}>Z_{As}, see AppendixB), while the Sb is brighter than the In for the InSb dumbbell (Z_{In}<Z_{Sb}), there should be a dumbbell intensity reversal if taking the profiles along the same direction. Analyzing the dumbbells [69, 127, 189, 201] in the concerned compressed region we can notice a progressive intensity inversion in the profile, evidencing an Sb gradient (Fig. 5.15(e)). Compared with other reported works on the same system [212], graded interfaces with an Sb gradient could be detected by EDX; but, due to the interface abruptness and the poor spatial resolution of the technique, the authors claimed the absence of Sb interdiffusion. However, our atomic resolution experiments support the reliability of the previous EDX results, suggesting an Sb gradient along few nanometers after the phase transition. We conclude that the sudden change from WZ to ZB phases takes place after the incorporation of small Sb quantities into the lattice, resulting in a sharp interface among the hexagonal and cubic phases (phase transition interface). This fact is not surprising, since III-antimonides tend to crystallize in pristine ZB phase, even in the case of ternary compounds with low Sb content (i.e. $GaAs_{1-x}Sb_x$, $InAs_{1-x}Sb_x$) [115, 262, 263]. Therefore, the discrepancy found among the experimental and theoretical mismatch values, 5.5% in front of 6.5%, is induced by the Sb incorporation into the InAs lattice. The larger size of the Sb compared to the As forces the lattice expansion of the pristine InAs ZB and, thus, decreases the lattice mismatch respect the pure InSb. Assuming a Vegard's law behavior for the InAs-InSb system, (and based on the experimental mismatch values), we calculate an atomic Sb content around 15% in average, implying that the concerned area is $InAs_{0.85}Sb_{0.15}$ instead of pure InAs or InSb. As our strain study is based on the analysis of the {111}planes, we performed the fitting with such planes, resulting in:

$$\mathrm{d} = 3.499 + 0.00242\mathrm{x}$$

Lattice compression	Atomic Sb%	Misfit spacing (nm)
0	100	∞
0.5	92	73.3
1.0	85	37.4
1.5	77	24.7
2.0	69	18.3
2.5	61	14.6
3.0	54	12.0
3.5	46	10.5
4.0	38	9.0
4.5	31	7.6
5.0	23	7.1
5.5	15	6.4
6.0	7	6.0
6.5	0	5.2

Table 5.3: Calculated values of the Sb content and misfit spacing for different lattice mismatches of the $InAs/InAs_{1-x}Sb_x$ system, used to built the plot in Fig. 5.16

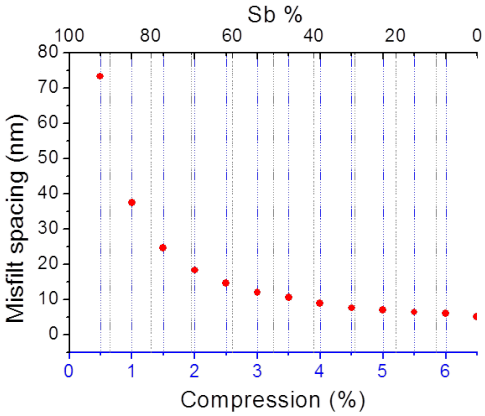

Figure 5.16: Misfit spacing among pure InAs and $InAs_{1-x}Sb_x$ ($0 \leq x \leq 100$), in terms of the Sb content (top axis) and lattice compression (bottom axis).

where d is the spacing of the {111}planes in the $InAs_{1-x}Sb_x$ region and x is the Sb atomic content (being x=0 for pure InAs and x=1 for pure InSb). On one hand, the maximum compression we can find at the $InAs_{1-x}Sb_x$ region is reached when there is no Sb content (x=0) and it corresponds to the theoretical mismatch between the pure InAs and InSb lattices, where misfit dislocations are expected to appear every 5.2 nm. On the other hand, the minimum compression would happen in the case of an absolute

absence of As (pure InSb), being the mismatch 0 % and the misfit spacing infinite (InSb homoepitaxial system). For intermediate compressions (0-6.5 %) the misfit spacing decays exponentially (inverse function) with the Sb content, as plotted in Fig. 5.16 (values accounted for the plot are gathered in table 5.3).

To fully understand the strain release mechanism, we model the $InAs$ WZ/$InAs_{.85}Sb_{.15}$ ZB/$InSb$ ZB system, as we did for the InAs WZ/InAs ZB/InSb ZB system, considered previously. The simulated images, calculated strain deformation maps and experimental results are displayed in Fig. 5.17. While considering the direct transition from InAs ZB to InSb ZB, dislocations should appear 5.2 nm spaced, induced by the 6.5% mismatch among phases (Fig. 5.17(d-f); accounting for the creation of a $InAs_{0.85}Sb_{0.15}$ ZB insertion in between the pure InAs and the pure InSb, results in a ZB compression of 5.5% at the intermediate ternary layer (Fig. 5.17(g-h), in good agreement with the experiments ((Fig. 5.17(a-c)). We compare the two modeled systems with the experimental results by plotting the difference in the $(\bar{1}1\bar{1})$ d spacing at both sides of the heterointerface in the three cases (Fig. 5.17(k)), enhancing the similarities between the experiment and the simulated graded interface. Similar observations have been reported in ref. [244]], where the authors found a compressed ZB region above the heterointerface in axial InAs/GaSb NWs, due to high In/Ga intermixing at the interfacial region, that results in the formation of a $In_{0.5}Ga_{0.5}As$ layer in between both pure phases.

So, the Sb incorporation promotes the sudden phase transition from WZ to ZB. From there, the Sb is gradually introduced into the structure and after 3-4 nm showing a $InAs_{0.85}Sb_{0.15}$ mean composition, the system gets the right InSb stoichiometry. The lattice mismatch between the $InAs_{0.85}Sb_{0.15}$ and InSb is around -5.5%, inducing the formation of misfit dislocations spaced 6.4 nm at the interface with the InSb. In the central region of the interface we find the expected misfit dislocations; but, closer to the edges there is a symmetric plane rotation instead. This plane rotation, up to $\pm$ 8º in the analyzed example at the $InAs_{0.85}Sb_{0.15}$ segment, releases the strain elastically, being the rest of the NW relaxed. In this way, both relaxation mechanisms may coexist at the same interface to allow the complete strain release: plastic deformation by formation of misfit dislocations at the central part of the NW, and elastic deformation through plane bending near the edges.

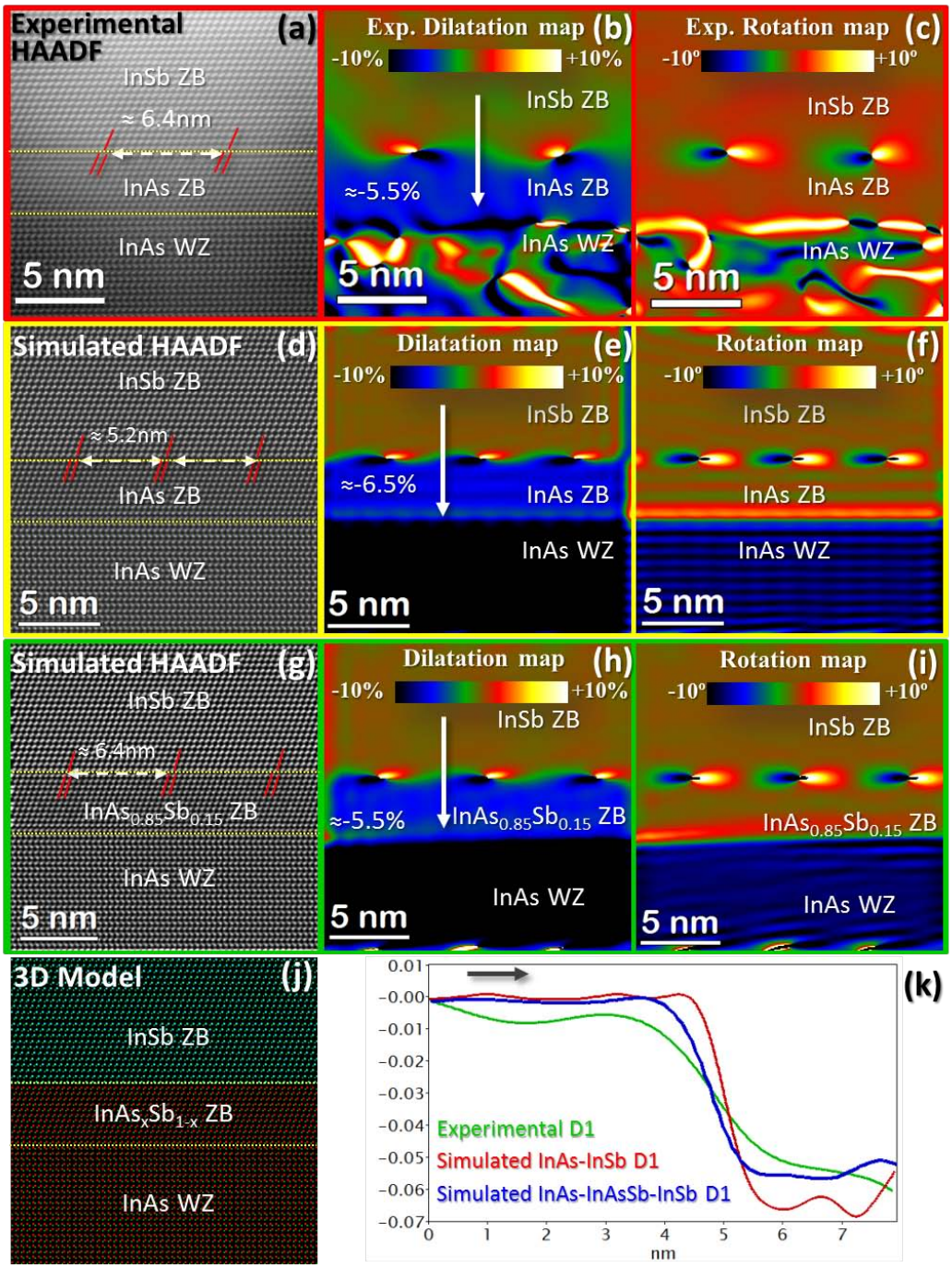

Figure 5.17: Left column contains HAADF images while middle/right column contains dilatation/rotation maps obtained by GPA on the $(\bar{1}1\bar{1})$ ZB planes. Top red panel (a-c): Experimental relsuts. Second row yellow squared (d-f): Simulation neglecting Sb diffusion. Third row green framed (g-i): Simulated system accounting for an intermediate layer with 15% Sb. (j) Atomic 3D model of the interface. (k) Profiles taken along the dilatation maps to enhance the similarities and discrepancies of the different models.

5.3 Conclusions

NWs can be used as templates for the combination of strongly mismatched materials under two different configurations, radial and axial. Although the NW geometry offers the possibility of an efficient elastic lateral strain release, there is a coherency limit dependent on the mismatch and dimensions of the system. Therefore, different mechanisms mediate the strain release at heterostructured NWs in order to achieve the partial or total lattice relaxation. We find out that:

- Thin GaAs shells around InAs NWs are highly expanded by the tensile effect promoted by the underneath InAs, despite the plastic contribution to the strain relaxation at the heterointerface and the elastic deformation at the shell.

- The axial cases analyzed reach the total relaxation following different paths: while GaN/InN and GaAs/GaSb mainly suffer from plastic deformation showing junctions plenty of dislocations, distributed adopting the blunt interface morphology; the InAs/InSb system shows a strained ternary transition layer separating the pure phases.

- On the one hand, the GaAs/GaSb system shows a core-shell interface due to GaSb overgrowth around the GaAs stem, which shows rounded tip. Thus, the shape of the interface is curved and full of almost periodic dislocations, especially at the central part of the NW. Similarly in the case of the GaN/InN system, the plastic deformation is strong, presenting a periodical array of misfit dislocations.

- On the other hand, in the InAs/InSb NW case, we have found an abrupt phase change from WZ to ZB, promoted by the introduction of Sb along the last 3-4 nm (Sb gradient) of the InAs phase (thus, resulting in $InAs_{1-x}Sb_x$). Therefore, in this case, the strain relaxation takes place at the interface between the $InAs_{1-x}Sb_x$ and the InSb. This region is 5.5 % compressed compared to the pure InSb section, which is compensated by the creation of misfit dislocations in the central area of the NW (plastic deformation) and by a large plane bending through the edges (elastic deformation). After the interface, the NW is completely relaxed. Thus, once again, the strain release occurs partially by the creation of dislocations (contrary to what was stated in most of the previous works found in the literature), along with plane bending.

The present results show with unprecedented resolution the different mechanisms that may combine for strain relaxation in a complex NW interface, allowing a fully epitaxial growth of the heterostructures. The 3D atomic models obtained can be extremely useful in order to compute and understand the final physical performance of the interfaces studied.

CHAPTER 6

Quantum Confinement in Nanowires: GaN/AlN System

6.1 Introduction

III-nitrides, namely AlN, GaN and InN, are attractive materials for the study of physical phenomena as well as for their integration on devices due to their outstanding optoelectronic properties. They have direct band gaps, covering a wide spectral range from the UV to the IR. Typically growing in the hexagonal WZ polytype, they are piezoelectric materials, showing spontaneous polarization, too. In the NW morphology they have been reported to be aplicable in diverse fields, as electronics [264], optoelectronics [265], energy conversion [266, 267] or sensing [26].

In addition, synthesized as NWs, their alloys and binary combinations can be exploited in innumerable ways, allowing the creation of self-assembled quantum structures (QSs) [51,56], tunable also, by strain engineering and doping. For instance, in the particular case of GaN, the ZB/WZ polymorphism can be tailored by Mg doping [93, 268, 269].

Importantly, by changing the dimensionality of the structures, the density of states (DOS) is modified due to changes in the confinement, as shown in Fig. 6.1. 2D (quantum wells, QWs), 1D (quantum wires, QWRs) and 0D (quantum dots, QDs) quantum structures within a NW are schematically displayed, along with experimental images and their corresponding DOS.

Thus, the creation of quantum structures is achieved by spatially confining the carriers through the growth of proper barriers. Then, in addition to the spontaneous polarization, arising from their bonding asymmetry (c/a ratio deviates from the ideal $(8/3)^{1/2}$ value as explained in Sec. 3.1), the 3D strain distribution within the NWs leads to the presence of piezoelectric polaritation-induced electric fields. Although detrimental for the optical performance, these fields can be screened by doping the quantum structures with Ge [270]. Moreover, Ge incorporated to the GaN lattice behaves as donor, increasing the conductivity as function of the donor concentration.

Given the tempting properties of GaN NWs, this chapter is devoted to the analyses of this material system in a variety of quantum architectures, correlating atomic characterization studies to their optical properties. From the growth of GaN NWs, the addition of AlN barriers allows the growth of isolated or manifold GaN nanodiscs (NDs), which are presented in the following. In addition, formation of self-assembled GaN QSs is observed, whose actual morphology is intensely analyzed. By detailed STEM characterizations combined with cathodoluminescence spectroscopy (CL), a better understanding of the optical response of the systems is provided. All the structures here analyzed have been grown by catalyst-free PAMBE on (111) Silicon substrates and under N-rich conditions [52].

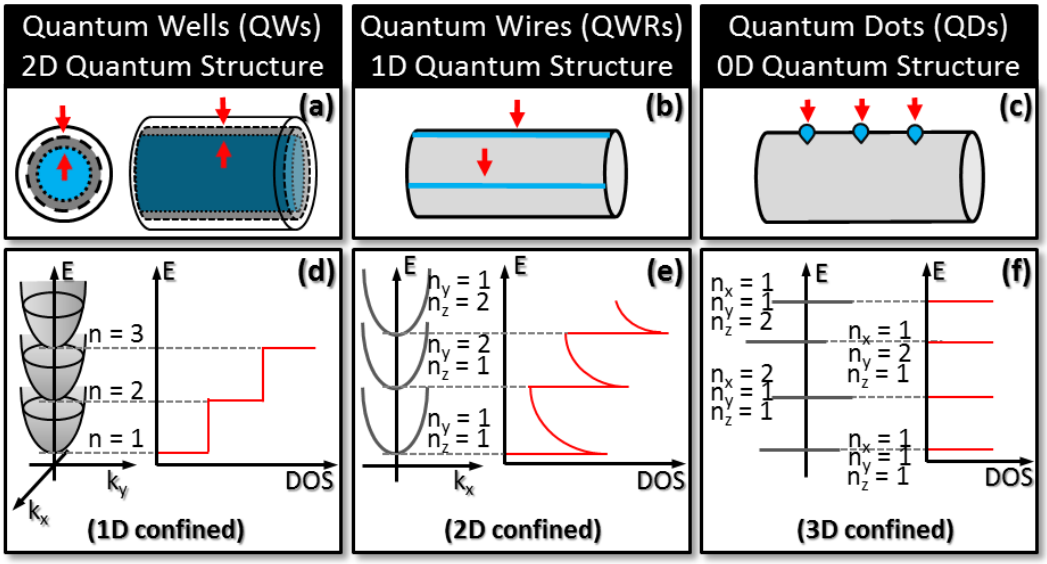

Figure 6.1: Different quantum structures in a NW classified by their dimensionality: (a) Quantum Wells or 2D structures (QWs); (b) Quantum Wires or 1D structures (QWRs); (c) Quantum Dots or 0D structures (QDs). (d-f) Experimental STEM and HRTEM images of QWs, QWRs and QDs embedded in NW. (g-i) Electronic density of states and corresponding energy levels for the QWs, QWRs and QDs, respectively. Adapted from ref. [42].

6.2 GaN/AlN Superlattices Contained in NWs

GaN NWs can be used as templates for the integration of GaN nanodisc (ND), embedded in axial AlN barriers, providing quantum confinement. These heterostructures are typically created by firstly growing GaN NWs used as stems (cores of the systems) for the growth of axial AlN barriers which contain the GaN NDs. It is worth mentioning that the parasitic radial overgrowth observed while growing the axial barriers leads to the formation of an AlN shell around the GaN sections (see Fig. 6.3). As a consequence, the inner GaN lattice is compressively strained since the lateral elastic relaxation through the NW sidewalls is constrained.

Along this section, we analyze systems consisting in combinations of several GaN NDs between AlN barriers, axially stacked. The GaN NWs initially synthesized fixed the overall geometry of the systems, which will contain 40 period GaN/AlN insertions. The GaN NDs are Ge doped, allowing the correlation of its doping effect on the carriers recombination, as explained in the following.

It should be mentioned, that the unintentionally AlN shell created has a thickness gradient along the length of the wires (thicker near the stem and thinner close to the tip), correlated to the appearance of axial strain gradients, and resulting in different

emission energies of NDs contained in the same NW [52]. Additionally, the coating provides an effective capping that prevents surface recombination processes. Note that also a lateral strain profile is enhanced by the lateral shell. This has important impact on the optical properties, as was demonstrated by [271].

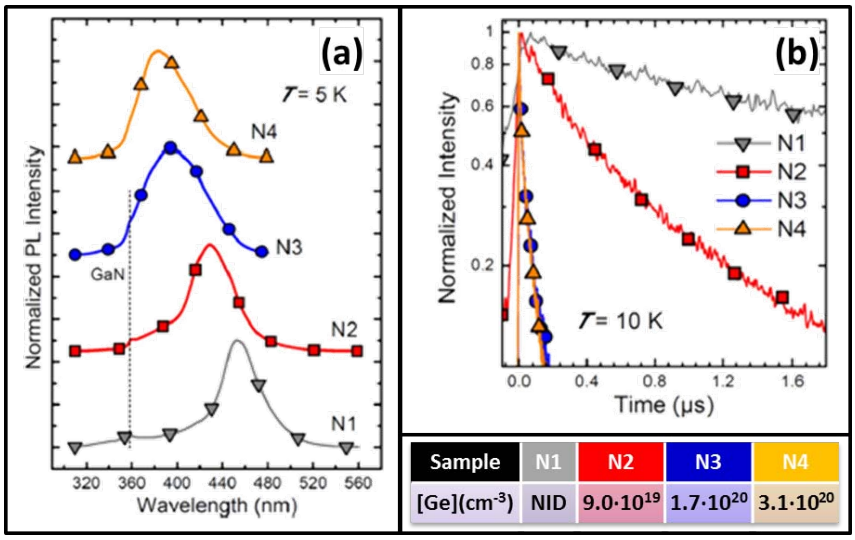

Figure 6.2: (a) Normalize PL spectra for samples N1-N4 obtained at 5K. The sample description is presented in the inset table (NID means non intentionally doped). Note the energy blue shift with the increasing Ge doping. (b) PL decay times measured at 10 K, for the same set of samples. Adapted from ref [271].

Moreover, by changing the dopant (Ge) concentration, the radiative recombination dynamics are strongly modified. This is due to the screening of the weak coaxial electric field promoted by the Ge incorporation, that leads to the radial centralization of electrons and holes and, thus, faster radiative recombination processes, along with an energy blue shift. Both facts are illustrated in Fig. 6.2, based on PL measurements performed on samples with Ge concentrations ranging from non intentionally doped to $3.1 \cdot 10^{20} cm^{-3}$.

Sharp axial interfaces between the GaN NDs and the AlN barriers are distinguished in the mapped EELS signal shown in Fig. 6.3, without intermixing of the Ga and Al constituents. In this example, the NDs have been grown during 0.5 minutes. The growth time of the AlN barriers is 1.43 min, resulting in 4.2 nm axial barriers. The mean experimental height found for the NDs is 2.5 nm. Atomic resolution images of these wires under two orthogonal zone axes are displayed in Figs. 6.4 and 6.5.

As commonly observed in GaN NWs, thin wires growing close to others are prone to merge together, leading to systems with several "legs". Depending on their thickness and proximity, they can become one single wire at the first stages while still growing

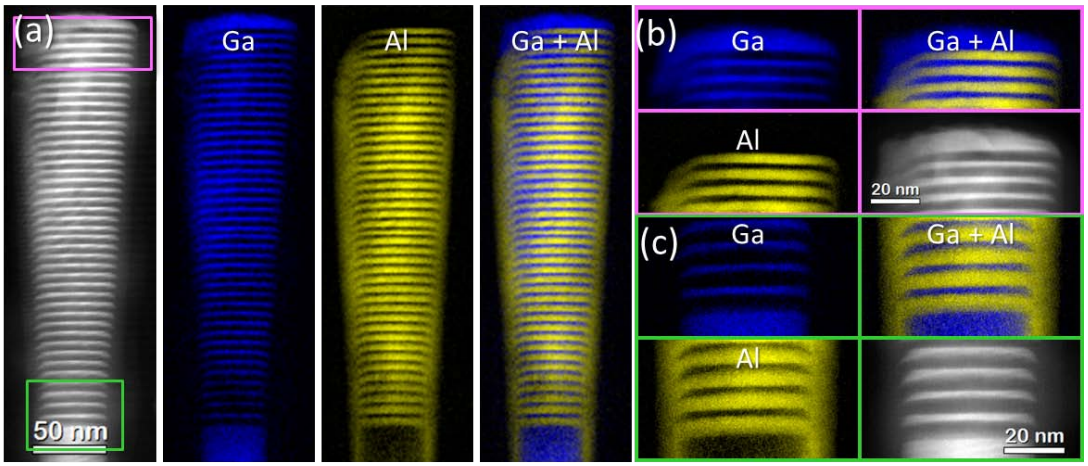

Figure 6.3: EELS mapping of the 40 period GaN/AlN heterostructure in a NW. STEM images are included in grey contrast scale, while the EELS signal are colored (Ga in blue and Al in yellow). (a) shows the 40 periods, and (b) and (c) correspond to the tip and first NDs grown, respectively.

the GaN stems (see Fig. 6.3(a)), or at the upper region, where the NDs are embedded (Fig. 6.5(a)). In the latter case, the discs and barriers tend to be aligned, inducing certain asymmetry on both. As mentioned in Sec. 3.1, the projection along the $[1\bar{1}00]$ direction, perpendicular to the flat sidewalls of the wires, does not allow the distinction of the crystallographic phases. In contrast, the perfect WZ structure of both phases is clearly seen in the $[11\bar{2}0]$ projection, normal to the corners where two facets meet. As commonly when growing under PAMBE conditions, both phases grow along the anionic $[000\bar{1}]$ direction. Interestingly, both dumbbell constituents can be observed after data treatment, based on a noise removal by means of a wiener filter and extracting the probe size effects by a deconvolution process, as explained in Sec. 2.5. The extensive inspections at the interfaces do not reveal misfits. In agreement, only one set of spot reflections is seen in the FFT, indicating that the system should be strained, as expected for pseudomorphic growth without dislocations.

The presence of GaN QS within the lateral AlN barrier is observed from both analyzed zone axes. The formation of similar structures has been previously explained elsewhere [56]. The authors reported the formation of quantum wires (QWRs) extending along the axis of the wires, starting from GaN insertions and slipping down within the AlN shell (see Fig. 6.6). Their formation is possible since the barriers tend to expose $\{11\bar{2}0\}$ lateral facets, in addition to the $\{1\bar{1}00\}$ bordering the GaN cores. In fact, those $\{11\bar{2}0\}$ surfaces permit the growth of GaN on them (otherwise inhibited or much slower on the $\{1\bar{1}00\}$ planes), allowing the self-assembly of GaN quantum structures while growing the NDs, as reported elsewhere [56]. Unfortunately, their dimensionality cannot be confirmed without analyzing a cross-section of the NWs. This issue is ana-

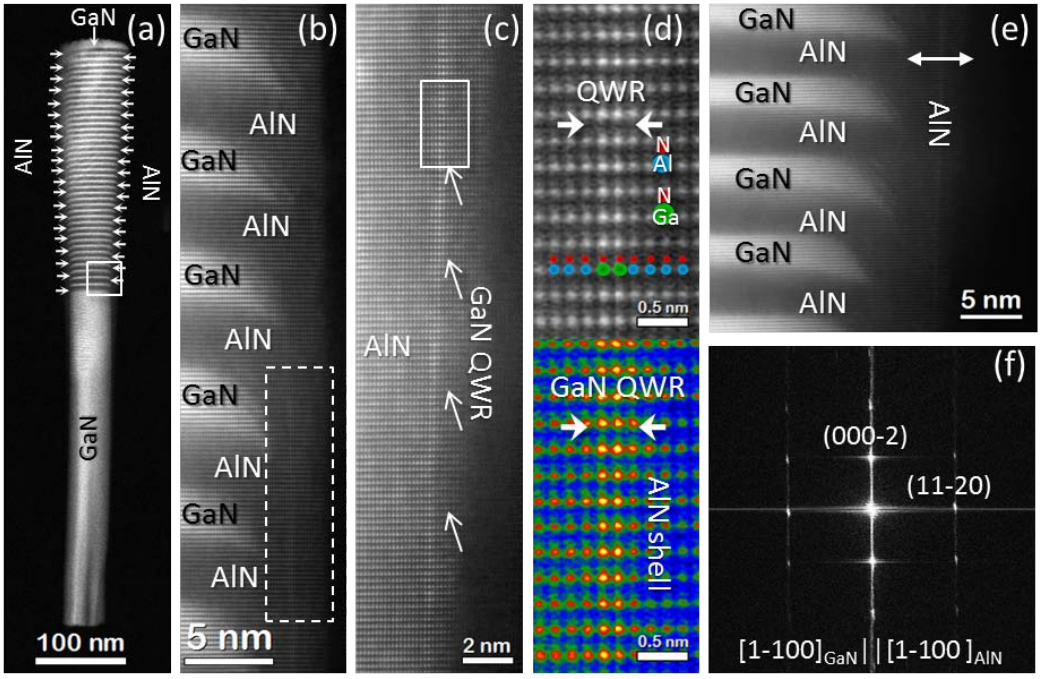

Figure 6.4: Structural charaterization of a 40 GaN/AlN NW along the $[1\bar{1}00]$ zone axis. (a) Low magnification image of one entire NW anlyzed, and atomic resolution details of different parts (b-d). The lateral AlN barrier with an increase thickness from the tip to the base is observed (e). Brighter areas in the barrier correspond to GaN QSs. No dislocations are detected and the FFT shows only one set of reflections (f).

lyzed in detail in Section 6.3, but referred to systems with one single GaN insertion.

The optical response of the structures is measured by CL-STEM, at both, room temperature and low temperature (96 K). The experiments are carried out at 120 kV, sacrificing the image resolution in the benefit of reducing the induced beam damage. The panchromatic collected emissions at both temperatures in different areas are shown in Fig. 6.7, where the observed signal comes from the upper region of the NWs containing the 40 Ge doped GaN NDs.

The monochromatic CL preformed in individual NWs allows higher spatial resolution and, consequently, different NDs within the active region can be identified. Line scans acquired along the length of the NWs, as schematically illustrates Fig. 6.8(a), show bright CL emission from the Ge doped GaN NDs in the 3.0-4.0 eV energy range. Two line profiles acquired at the same NW at room temperature and at 96 K are displayed in Fig. 6.8(b) and (c), respectively. The electron beam induced carriers when the probe is located on a GaN insertion are confined within the NDs region, where they combine together, resulting in the observed emission. The carrier recombination within

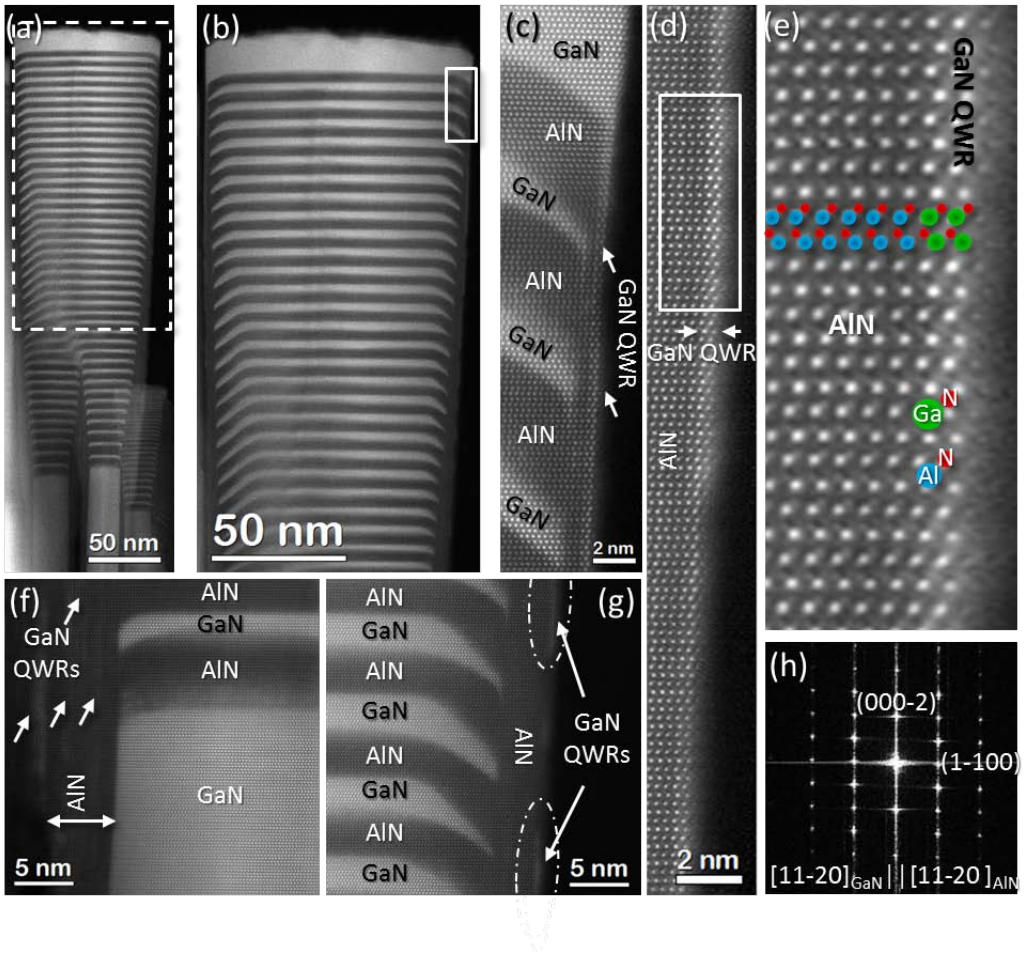

Figure 6.5: Structural charaterization of a 40 GaN/AlN NW along the $[11\bar{2}0]$ zone axis. (a, b) Low magnification images of the 40 period GaN/AlN. (Atomic resolution images of different parts of the system. Thin wires of GaN draining from the disc along the barrier are evident. (h) FFT of the system.

the barrier takes place at the UV region, out of the studied energy range and, therefore, invisible to the technique. Thus, the spatial fluctuations visible on the CL intensity emission are due to the presence of GaN NDs. Comparing both spectra, an energy blue shift when cooling down is appreciated, accordingly to the bandgap widening induced by the thermal lattice contraction.

According to the statistics performed on the (S)TEM data, the NDs height developed while growing during 0.5 min is 2.5 ± 0.4 nm (5 nm/min axial growth rate), while the AlN barriers, growing during 1.43 min achieved a 4.2 ± 0.6 nm (2.9 nm/min axial growth rate) height. The spatial resolution of the CL experiment here reported is the 2 nm, hampering their single detection, but still visible, as shown in Fig. 6.8.

In addition to line scans along the NWs, we analyzed the 2D energy distribution

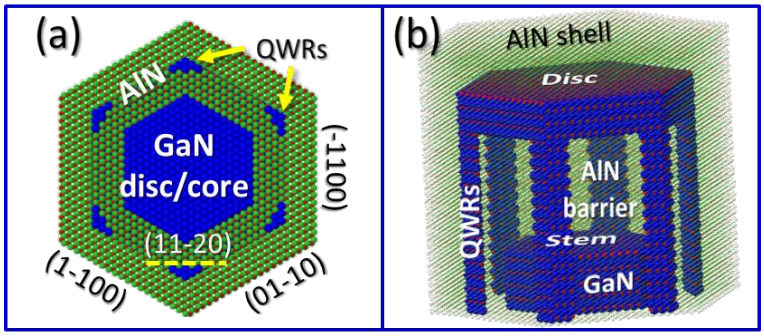

Figure 6.6: 3D atomic model of the self-assembled GaN QWRs on the truncated corners of the AlN shell, as explained in the text. (a) Top view of the GaN/AlN system shown in perspective in (b). Adapted from ref. [56]

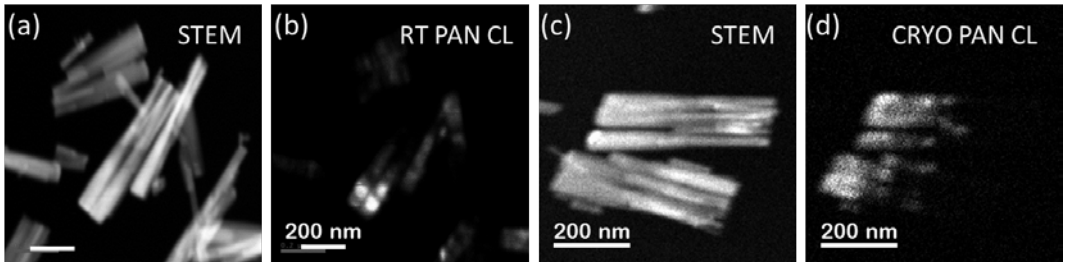

Figure 6.7: Panchromatic spectra collected at room/cryo temperature (b/d) in the area shown in (a/c).

by acquiring spectra imagining (2D CL emission maps). The CL maps included in Fig. 6.9 were acquired at a temperature of 96 K at the upper region of one NW, where the 40 GaN NDs are stacked within the AlN barriers. In the figure, the CL emission maps within 3.2-4.1 eV energy range are displayed. The bright emissions axially stacked correspond to the location of the GaN NDs, which clearly suffer a blue emission shift when going from the tip (3.3 eV) to the bottom (3.9 eV). This fact is understood under the consideration of the thicker AlN radial shell surrounding the NDs closer to the GaN stem than those near the tip. Since the first grown NDs are exposed to more AlN growth periods, they experiment further AlN covering, resulting in larger lattice compression and higher emissions energies [52].

At this point, it should be noted that observed polarization effects result from the interplay of different parameters and the additional influence of the Ge doping, as reported in ref [271]. While the radial fields are only caused by a lateral strain gradient, the axial fields are caused by polarization discontinuities at the heterointerfaces. As consequence of the lattice compression, the electrons are pushed to the center of the NDs, while the maxima of the valence band is located at the NW sidewalls. Therefore, apart from the axial electron-hole separation (with most of the electrons located at the

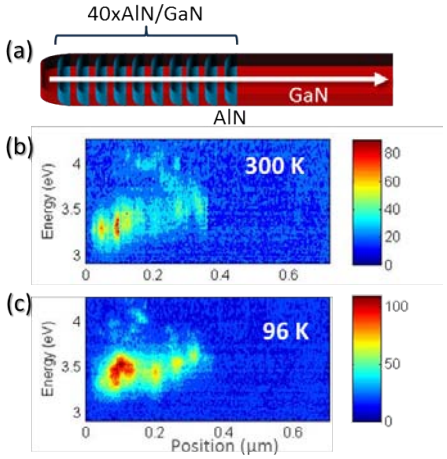

Figure 6.8: CL line profiles along a GaN NW with 40 AlN/GaN:Ge axial insertions as shown in the sketch in (a), obtained at room temperature (b) and at 96 K (c).

bottom of the discs, within the conduction band, and holes into the valence band at the top of the discs), the geometry of the system leads to a 3D strain distribution within the NDs that further separates the carriers radially (electrons through the center and holes through the edges or the other way around, depending on thickness of the AlN shell). Consequently, slow PL decay times of few microseconds at 5 K are observed in non doped systems. Interestingly, the radial electric field can be screened by Ge doping at the NDs in the range of $9 \cdot 10^{19} - 3.1 \cdot 10^{20} cm^{-1}$. The hole wave function is then shifted towards the center of the wire, being vertically aligned with the conduction band maxima, resulting in a better overlapping of electron-hole wave functions. The screening of the electric fields can be detected in the PL measurements. Whereas the main effect of the radial screening is related to the PL decay time, the axial screening effect is noticeable by the blue shift of the emission energy. Non-doped systems have shown PL lifetimes two orders of magnitude longer than doped Ge wires, within the range of doping level analyzed. Thereby, the radiative recombination lifetime is strongly dependent on the doping level and a huge control of the exciton dynamics is achievable by accurately doping the material.

The same trend is observed for NDs with longer growth times, where the discs reach a mean height of 7.8 ± 1.1 nm, while the same growth time of 1.43 min is used for growing the AlN barriers. The obtained CL line scans performed along individual NWs show how those discs closer to the NW stem (right side in Fig. 6.10) emit at higher energies than those close to the tip of the wires. Thus, the NDs close to the tip have narrower gaps, with lower emission energies (left side in the figure), than the ones closer to the base. Again, this fact can be explained accounting by the internal strain distribution, with an axial modulation of the radial component along the length of the structure.

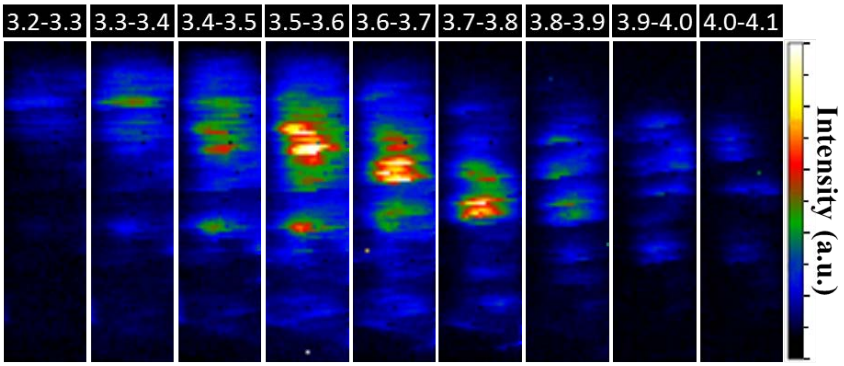

Figure 6.9: CL maps of the 40 period GaN/AlN region of one NW in the 3.2-4.1 eV energy range, every 0.1 eV. The spectra were acquired at 96 K.

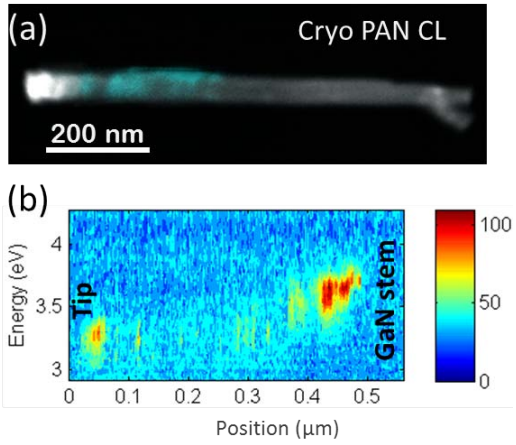

Figure 6.10: CL measurements performed in individual NWs at 120kV and 96 K. (a) Superposition of the panchromatic map (cyan colored) with its STEM image. (b) CL emission collected along a line scan crossing the 40 GaN/AlN insertions in a NW.

In addition, the compressive uniaxial strain induced by the lateral AlN shell blue shifts the interband optical transition while almost does not disturb the intraband transition. The calculated band diagrams show a dependency on the applied axial strain, which scales with the thickness of the radial AlN layer, and the presence of surface states to reproduce the experimental behavior [272].

The further PL analyses performed in these NWs have allowed addressing many interesting effects of the Ge doping on the carriers behavior. On one hand, the polarization induced internal electric fields within these heterosystems can be efficiently screened by Ge doping the discs. The induced electric fields red shift the emission according to the quantum confined Stark effect. However, the increasing Ge doping of the

discs results in the blue shift of the PL emission [270].

6.3 Single GaN Discs Contained in NWs

Along this section, we characterize the structural and optical properties of GaN NWs, each of them containing a single GaN disc embedded in axial AlN barriers. We analyze the formation of self-assembled GaN QSs, following the approach described in Section 6.2, and reported elsewhere [56]. The growth was optimized by varying the experimental conditions, as the beam equivalent pressure of the gallium effusion cell (BEP_{Ga}) or the growth time to develop the AlN barriers (t_{AlN}). The heterostructures are created stacking axial AlN barriers which contain the GaN NDs, on top of GaN stems. Once again, the AlN shell surrounding the discs strains compressively the GaN lattice, since the lateral elastic relaxation through the NW sidewalls is constrained.

Therefore, up to three optically active regions could be expected in these systems: the GaN core itself, the GaN disc and the possible GaN quantum structures, QS (quantum wires, QWRs, or wells, QWs), with different energy emission as corresponds to their different degree of quantization and their relative morphological constrains. However, in practice, the GaN discs here analyzed would not show much difference compared to the GaN core, since they are too thick to exhibit confinement.

The creation of the nano and quantum structures within a NW relies on the ability to design and grow the proper barriers. Fig. 6.11(a-d) shows several GaN NWs containing the *AlN barrier/GaN disc/AlN barrier* sequences from a set of samples changing the growth time t_{AlN} of the AlN barrier separating the GaN core and the ND. We find a linear relationship between the AlN growth time and the height reached by the barriers, and even the shorter AlN growth times employed (3 min, shown in Fig. 6.11(e)) result in barriers thicker than 10 nm, enough for isolating the GaN NDs. We can detect the presence of lateral QS in all the samples varying the AlN thicknesses, although not all of them are optically active, as extracted from the PL and CL analyses. The peak at 3.9-4.0 eV shown in the PL emission at 4K, plotted in Fig. 6.11(f), evidences quantum emission for samples with thicker barriers (black and red curves, corresponding to t_{AlN} of 18 and 13.5 min), while samples with shorter t_{AlN} lack emission at this energy range. Such fact can be tentatively attributed to the shorter length of those QSs assembled around the facets of the first barrier for the shorter growth times.

Therefore, we will be concerned about those samples grown with longer AlN deposition times, while modifying the precursor fluxes by checking different BEP_{Ga} during the ND growth. Two different Ga partial pressures, BEP_{Ga} of $3.9 \cdot 10^{-7}$ and $5.1 \cdot 10^{-7}$ mbar, are analyzed in the following.

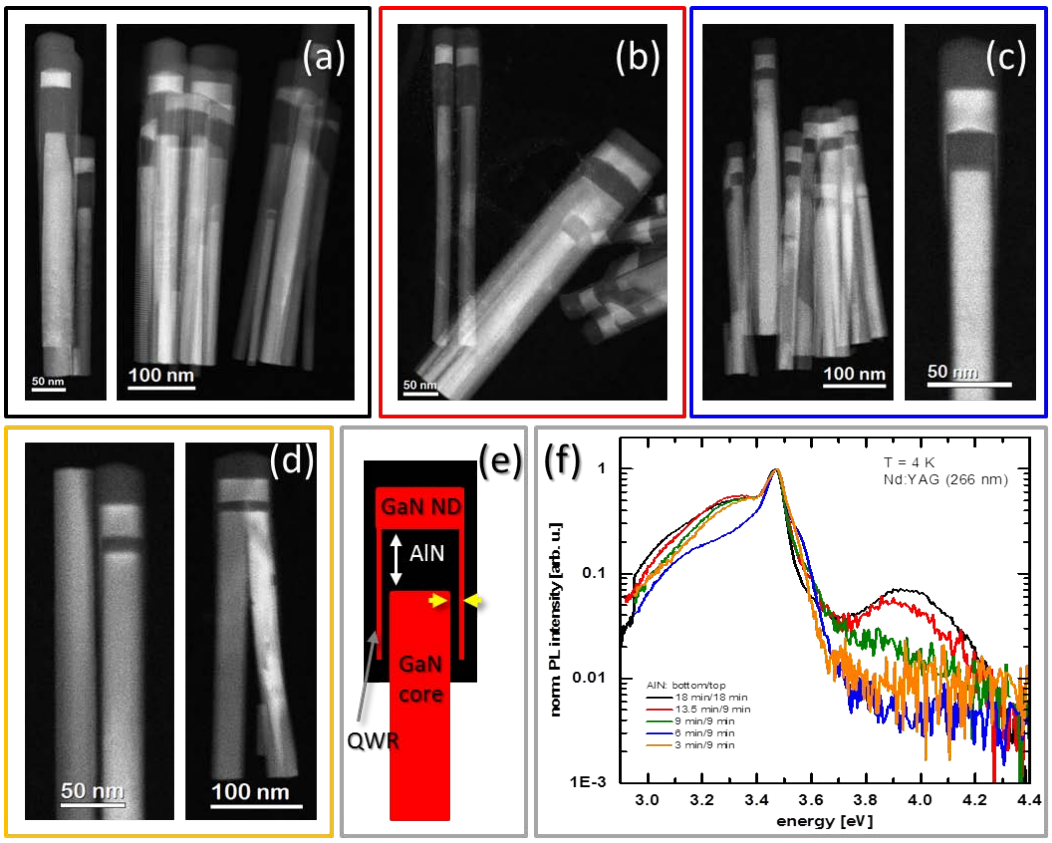

Figure 6.11: Low magnification ADF images of GaN/AlN NWs synthesized varying the AlN growth time: 18 min(a), 13.5 min (b), 6 min (c) and 3 min (d). (e) Sketch of the obtained structures. (f) PL results obtained at 4K by using a Nd:YAG laser ($\lambda = 266$ nm).

The main results of the structural characterization of a sample grown by setting the BEP_{Ga} at $3.9 \cdot 10^{-7}$ mbar while keeping the t_{AlN} at 18 min are summarized in Fig. 6.12. The brighter sections on the wires correspond to the GaN regions, while the dark areas are the AlN barriers.

AlN and GaN grow in the WZ phase following the $[000\bar{1}]$ direction. No crystalline defects are observed on the structures or at the interfaces. The presence of AlN surrounding the GaN core evidences the already mentioned AlN radial growth when creating the axial barriers (Fig. 6.12(d)). In addition, we detect the existence of GaN QS within the AlN shell below the discs, which resemble QWRs along the projected direction ($[11\bar{2}0]$ zone axis).

Paying attention to the ND morphology, we find well defined lateral planes but blurred top and bottom facets bordering the disc (Fig. 6.12(b)). However, a closer look at the structure properly focused reveals the presence of crystallographic planes

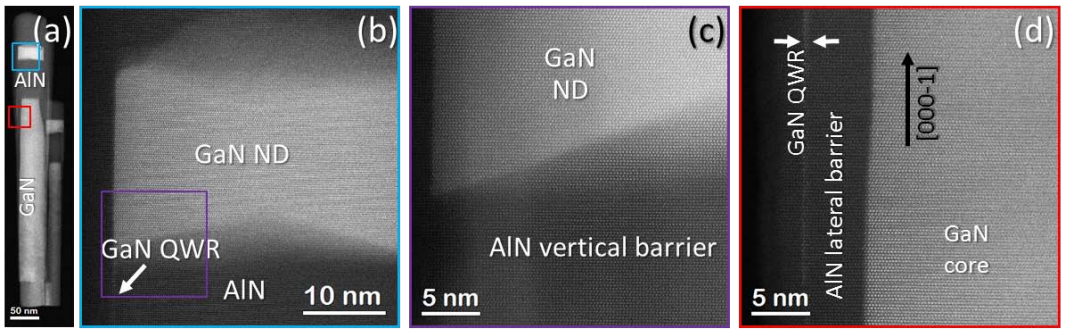

Figure 6.12: HAADF images of the GaN/AlN NWs. (a) Low magnification image of an entire NW. (b-d) Atomic resolution details at different locations of the NW, showing the ND (b,c) and QWRs separated from the GaN core by lateral AlN barriers.

limiting the ND, as illustrates Fig. 6.12(c). Therefore, it is apparent that NDs are not simple flat insertions but have a more complex faceting along the growth direction. Their cross-section is hexagonal as the GaN NWs are, six-folded bordered by $\{1\bar{1}00\}$ planes, and in addition to the flat $\{0001\}$ bottom and top facets, they show $\{1\bar{1}0\bar{l}\}$ planes at the edges. These semi-polar planes faceting the NDs have been observed in InGaN/GaN superlattices contained in NWs, too [51]. The InGaN insertions reported exhibit $\{10\bar{1}l\}$ planes, with l = -1, -2 and -3, following the faceting of the underlaying GaN insertion. We find l to be 4 most of the times, but other facetings are also possible. By considering this geometry, the resulting NDs show a downwards bended shape, with a "lump"on the top and a "cavity"on the bottom, as shown in the 3D model in Fig. 6.13. The similarities between the proposed model and the experimental data become clearer by calculating the simulated images, which nicely reproduced the blurring due to the overlapping of the GaN ND shape with the surrounding AlN barriers. Simulations of the system along the two most common zone axis employed for characterizing the samples, i.e. $[11\bar{2}0]$ and $[1\bar{1}00]$, are displayed in Fig. 6.13(c,f). Similar island shapes are developed when stacking axially InGaN and GaN insertions in a NW, which formation has been related to the contained elastic strain inducing the formation of 3D island-like structures rather than 2D flat discs [273].

We conduct further structural investigations on another sample synthesized under the same growth conditions but increasing the BEP_{Ga} to $5.1 \cdot 10^{-7}$ mbar while creating the disc. The same structural issues concerning the previous sample are observed here, without noticeable differences. The materials grow defect-free on the hexagonal phase along the $[000\bar{1}]$ direction. The overall system again has a hexagonal cross-section created by $\{1\bar{1}00\}$ planes, showing also the same kind of ND faceting (see Fig. 6.14). Lateral QS embedded within the AlN shell are also present in these wires, as pointed in Fig. 6.14(c,g). Though most of the structures show sharp transitions between the

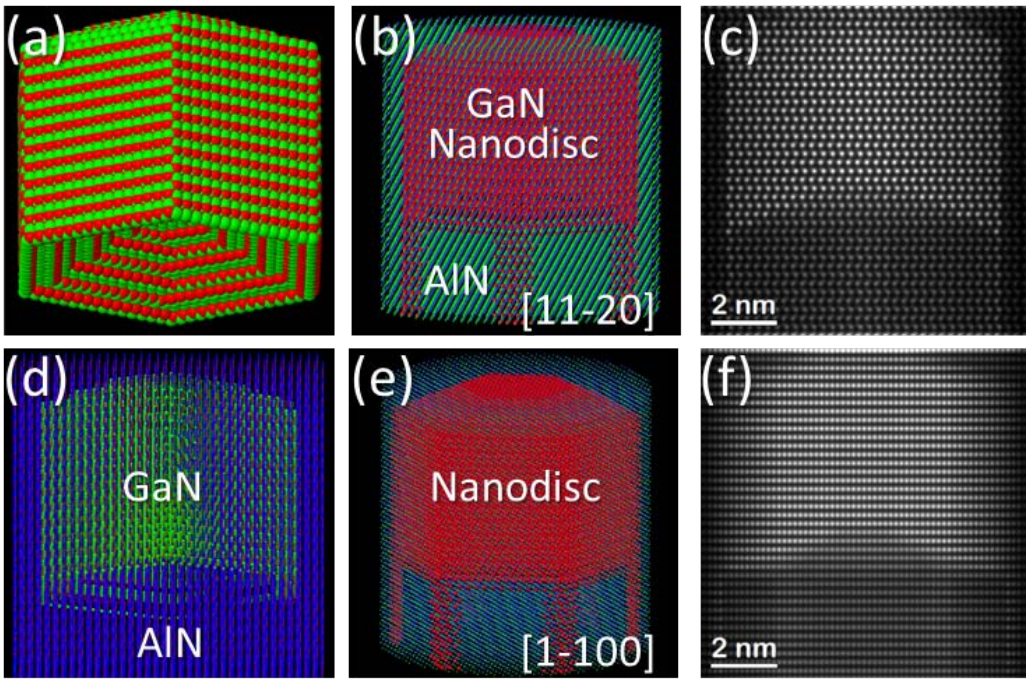

Figure 6.13: Modeling and simulations of the GaN NDs/AlN barrier system, containing GaN QWRs. (a/d) 3D Atomic model of the ND without/showing the AlN barrier. (b/e) GaN NDs and QWRs embedded on the AlN shown along the $[11\bar{2}0]/[1\bar{1}00]$ zone axis and the corresponding HAADF image simulations (c/f).

AlN and GaN phases, we find some examples of Al-Ga interdiffusion in both samples (growing under different BEP_{Ga}), as shown Fig. 6.14(g,h). It is worth to mention the high merging tendency shown by wires growing side by side, as illustrated in Fig. 6.11 or 6.14(a,f). Despite the merging, in most of the cases they coherently grow aligning the NDs and barriers at roughly the same height, creating bigger (thicker) structures. Such fact can be observed, for instance, in Fig. 6.11(b,d), showing different NWs resulting from the merging of thinner ones to create a wider structure. If the merging takes place during the early stages of growth, while creating the GaN stems, only one GaN disc will cover the whole diameter. However, NWs merging while growing the barriers or discs will result in more asymmetric systems, since the barriers and disc axially shifted will be forced to match together, 6.11(a,c).

In spite of the structural similarities found at the samples growing with different BEP_{Ga}, subtle discrepancies can be found at their PL spectra above 3.7 eV. While the lower Ga flux leads to a PL emission at 3.927 eV with a FWMH of 297 meV, the systems growing with the higher BEP_{Ga} emit at lower energy, 3.833 eV, but showing a narrower peak (FWMH = 199 meV). The large energy blue-shift of the observed emis-

sion compared to bulk GaN (3.4 eV) is attributed to the quantum confinement. The relatively large widths of the PL emission peaks can be understood accounting for the formation of inhomogeneous QSs, with different lengths and thicknesses. Indeed, the issue of which is the actual morphology of the QSs, i.e., elongated QWRs or 2D-like thin coaxial QWs, remains unclear at this point. To fully characterize the systems and get more insights on the optical emission of the NWs, we measure the CL response on STEM mode in the first sample presented, grown with a BEP_{Ga} of $3.9 \cdot 10^{-7}$ mbar.

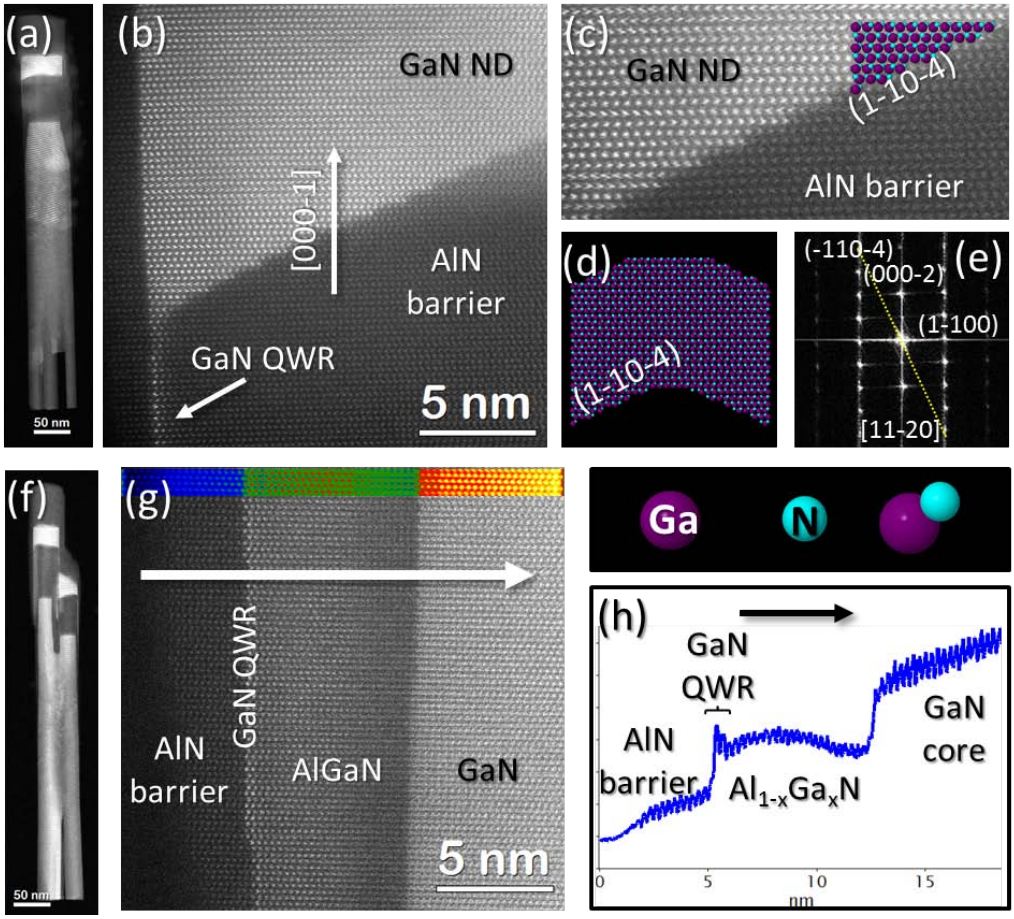

Figure 6.14: (a/f) Low magnification HAADF images of the couple of NWs atomically analyzed in (b-e) and (g,h), respectively. Presence of GaN ND and QWRs are indicated. The experimental ND in (b,c) shows a $1\bar{1}04$ bottom faceting, in good agreement with the 3D model. (g,h) evidence the Ga diffusion within the barriers, observed in some of the NWs.

The measurements were performed at 120 kV acceleration voltage to prevent the sample damage observed at 200 kV, slightly degrading the STEM spatial resolution. The main CL results obtained are displayed in Fig. 6.15. The panchromatic CL spectrum of the wire shown in Fig. 6.15(a) is included in (b), evidencing the emission around the location of the AlN layer, mainly through the edges; while no emission from the

GaN disc or stem is detected. Similarly, only emission from the supposed AlN barriers are detected at the bunch of NWs shown in (c), where the panchromatic emission is red colored and superimposed to the STEM image. The resulting emission is found to occur at about 3.9 eV, as can be seen in the line scan taken across the NW diameter (following the white arrow), where up to three separated emissions can be identified. On one hand, as the emission is not continuous across the NW, we may discard the formation of a uniform coaxial well. On the other hand, although we can distinguish spatially separated active regions emitting (labeled as 1, 2 and 3 in Fig. 6.15(d)) across the diameter, we cannot ensure if they correspond to QWRs or inhomogeneous wells.

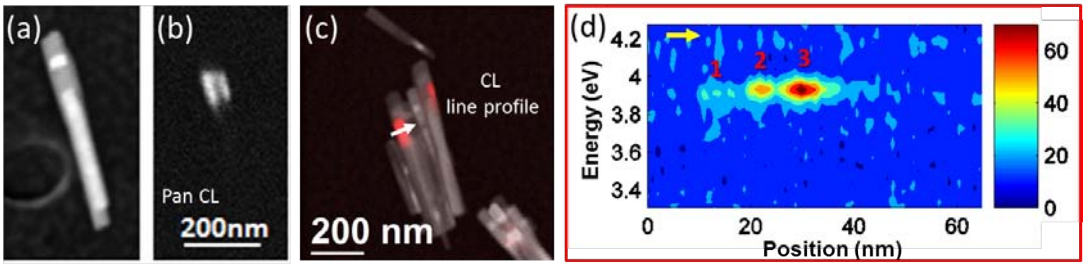

Figure 6.15: ADF image (a) of one GaN NW with one GaN ND separated by AlN barriers, along with its panchromatic image (b) showing CL emission near the two sidewalls of the AlN layer, corresponding to the presence of lateral quantum structures along the barrier. Note that both merge to some extent near the top. (c) Image indicating the position of the CL line profile displayed in (d). (d) CL profile showing emission at about 3.9 eV spatially separated into at least two clear regions.

So far, we have identified the presence of QS at every sample analyzed, but their real shape cannot be unambiguously determined unless analyzing a cross-section of the NWs perpendicular to their growth axes. For this goal, the sample is axially sectioned by FIB, allowing the analysis of the structures along their growth axes, as shown in Fig. 6.16. Since we do not know the exact place where the cut was performed, we cannot ensure if the bright hexagons are the GaN stems or the NDs. Anyhow, the GaN distribution within the AlN barrier is unarguably inhomogeneous, covering most of the AlN lateral facets but still leading some opened spaces between the walls. Moreover, its thickness is neither constant, being as thin as one monolayer in some regions, while exceeding the 10 in some others. A tendency towards the GaN accumulation at the available {11-20} facets can be observed, in agreement with ref. [56].

In the light of the observed GaN distribution around the AlN barrier, we can better understand the optical measurements. Since the NWs are pretty thin but not enough to exhibit quantum confinement, their weak bulk-like emission could not be detected by CL. However, higher emission efficiencies of confined states are seen around the AlN barrier region, where the self-assembled inhomogeneous GaN wells are embedded. Typ-

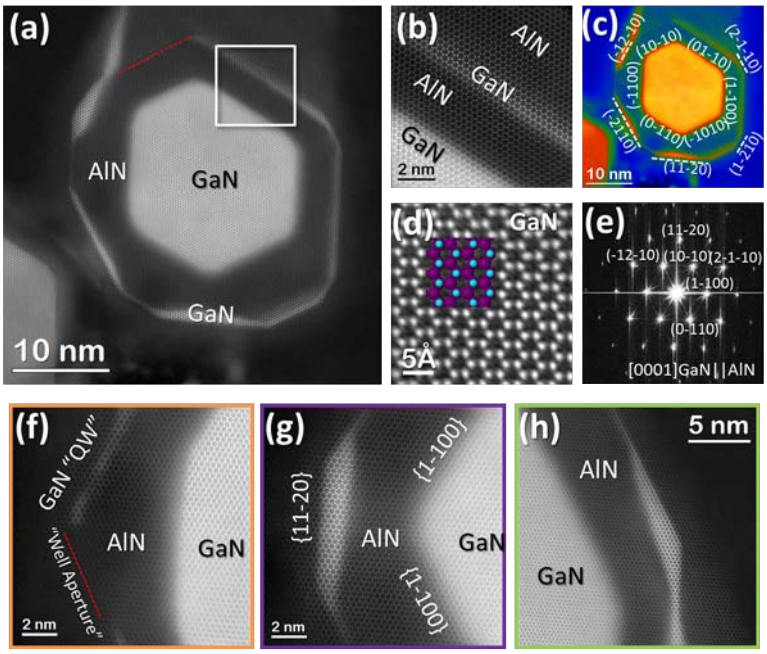

Figure 6.16: Atomic resolution HAADF images of the cross-section of GaN NWs (a), along the [0001] direction (d, e) . The central bright art is the GaN ND/core of the wires, surrounded by AlN barriers. Embedded in the AlN, there are GaN quantum wells (b) partially covering the NW diameter (c, f). At some $\{11\bar{2}0\}$ corners, GaN accumulations can be detected (g, h).

ical signals collected there reach energies up to 3.9 eV, in agreement with the presence of GaN quantum states. The optical response of the same system intentionally n-doped is discussed in the following section.

6.3.1 Intentionally n-Doped Systems

The incorporation of impurity atoms within the crystalline lattice of a semiconductor material may introduce additional energy levels within the gap, modifying its optical response. n- or p- doping can be achieved depending on whether the foreign atoms incorporated at the lattices contribute with more or less electrons to the guest material, acting as a donor or acceptor, respectively. For the specific case of GaN, Si is usually used as a donor while Mg is the most common acceptor. This can lead to the localization of excitons at the impurities, and the presence of free carriers can influence the emission properties.

Germanium, as the closest gallium neighbor on the periodic table, represents a suitable element for the n-type doping of GaN. Due to their similar sizes, Ge incorporation at doping concentrations should not distort significantly the GaN lattice. Although reports can be found on the Ge doping of GaN thin films; it was not until 2013 that we

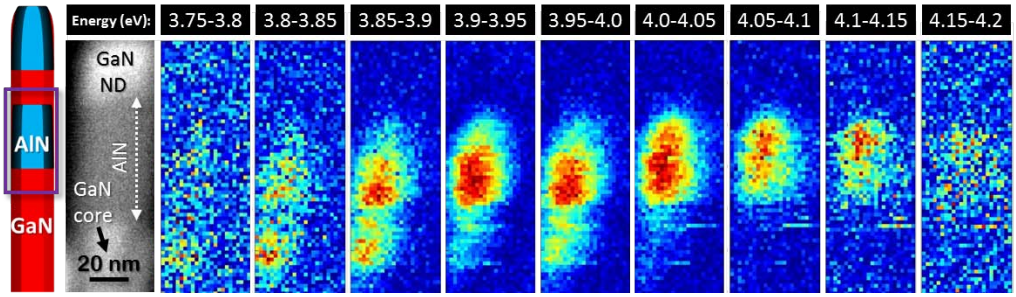

Figure 6.17: CL emission mapped at the NW shown on the left (ADF image), acquired around the AlN barreir as shown in the sketch (purple frame). A wide range of CL emission is observed, ranging from 3.8 eV up to 4.1 eV, indicative of quantum confinement. The spatial location is mainly centered at the supposed AlN barriers, presumably containing GaN quantum structures.

published the first report on Ge doping of GaN NWs [274]. The resulting wires keep the crystalline perfection of the non intentionally doped ones, also preserving their prismatic section and high aspect ratio. Contrary to what is reported for the use of Si doping, which asymmetrically widens the NW diameter leading to conical wires [275], the axial/radial growth rate when doping with Ge is mostly unchanged, and non-tapered NWs are obtained within the doping regime employed. The amount of Ge incorporated into the lattice can be controlled by adjusting the BEP_{Ge}, which effectively modifies the Ge flux during growth. Moreover, within the BEP_{Ge} range employed (from $1.5 \cdot 10^{-11}$ to $1.3 \cdot 10^{-9}$ mbar), secondary ion mass spectrometry measurements show that the Ge content within the lattice is directly proportional to the BEP_{Ge} employed. The linearity among the employed pressure and the final Ge concentration is indicative of a complete dopant incorporation, at least up to $3.3 \cdot 10^{20} cm^{-3}$ Ge content. The continuous increase in conductivity with increasing Ge doping is also demonstrated by the electrical measurements performed (the resistance from the contacts is eliminated by using a 4-point geometry).

Known the capability of Ge doping GaN NWs grown by PAMBE, the procedure can be implemented to selectively dope part of the systems. The samples analyzed here consist, as in the previous section, in single GaN discs inserted in AlN barriers, created on top of GaN NW stems. In order to selectively dope the discs, the Ge effusion cell is switch on while they are growing, at two different partial pressures. The lower BEP_{Ge} employed corresponds to $5.7 \cdot 10^{-12}$ mbar, while the highest pressure concerned is $8.7 \cdot 10^{-10}$ mbar.

CL analyses of the lighter doped sample are summarized in Fig. 6.17, where emission maps displayed every 50 meV corresponding to the region of interest of one NW (between the GaN core and the GaN Ge-doped disc) are included. A dim luminescence

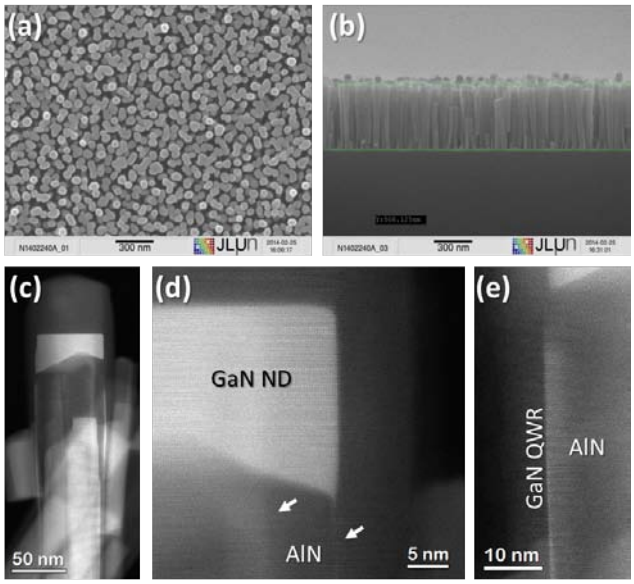

Figure 6.18: Top (a) and frontal view SEM images of the GaN/AlN NWs as grown on the substrate. (c-e) HAADF images of the NWs, identifying the GaN ND and presence of GaN quantum structures at the AlN barrier.

is detected at 3.85-3.95 eV around the core region, but again, the main signal is found where the AlN is located. Such fact is not surprising if invoking the observed formation of almost 2D coaxial GaN shells around the AlN barriers (Sec.6.3), and the negligible impact of the Ge incorporation into the lattice on the morphological and crystalline aspects [274]. Indeed, we attribute the strong emission at 3.85-4.1 eV to the presence of GaN coaxial layers, embedded within the AlN shell, mainly developed on the left side of the present wire.

Regarding the heavily doped NDs, structural inspections do not show noticeable differences respect to the non-doped samples. Once again, the AlN and GaN crystallize under WZ structure, also in the discs where the doping is intended. The wires are found to grow along the $[000\bar{1}]$ direction, and the lattice perfection is kept along their entire length. They also follow the same merging trend (evident in top view SEM image included in Fig. 6.18), leading to thicker wires which try to align barriers and discs axially, inducing certain asymmetry in most cases. Finally, in agreement with other samples, too, we can detected presence of GaN QS contained within the AlN shell, as shown in Fig. 6.18(c-e).

CL-STEM analyses obtained on the sample can be found in Fig. 6.19. We find some emitting discs at about 3.7 eV 6.19(a,b) but once again the spectra are dominated by the emissions originated through the sides of the AlN barrier regions (Fig. 6.19(a,c))i

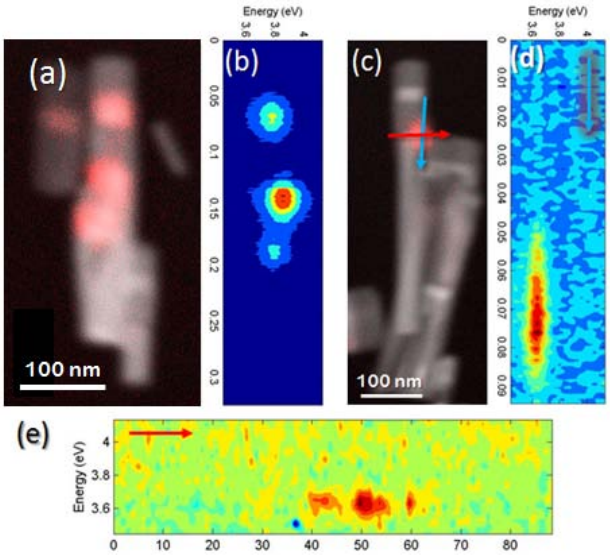

Figure 6.19: (a) Panchromatic CL superimposed (red colored) to the STEM image. (b) CL map of the image in (a). (c) STEM image and panchormatic CL, superimposed in red, at another NW. CL profiles along perpendicular directions have been taken along the region of interest, pointed by blue and red arrows and respectively displayed in (d) and (e).

in agreement with panchromatic images. CL line scans along two orthogonal directions within the optically active side (following the arrows in the STEM image in (c)) are plotted in Fig. 6.19(d,e). The emission at 3.6 eV appears homogeneously distributed axially (d), while it is not continuous radially. Such GaN distribution within the AlN barrier explains the observation of projected QWRs when analyzing the crystalline structure along the NW (i.e., $[11\bar{2}0]$ or $[1\bar{1}00]$), which in fact have a certain lateral extension.

Therefore, the controlled introduction of Ge doping within GaN NWs grown by PAMBE can be achieved. The resulting Ge concentration is proportional to the BEP_{Ge} supplied at the working regime. The obtained Ge:GaN NWs retain the main structural and morphology aspects shown by non-doped GaN NWs grown under similar conditions. The procedure can be implemented by doping single GaN NDs contained in AlN barriers axially grown on top of GaN NWs. The structural and optical measurements performed evidence the presence of 2D GaN QS within the barriers, as happened in the non-doped samples. For the highest doping intended (by using a BEP_{Ge} of $8.7 \cdot 10^{-10}$ mbar), ND luminescence at energies above 3.7 eV are detected. As the QSs are created while growing the discs and assuming a homogeneous incorporation of the dopant on the lattice, it is expected that the QSs will be doped when the discs are.

6.4 Conclusions

Summarizing, several types of GaN NWs containing GaN NDs confined by axial AlN barriers have been intensively analyzed, with respect to their structural properties. Where possible, the structural characteristics are related to the optical properties.

The former inspected systems are 40 fold period GaN /AlN heterostructures axially stacked within NWs. The development of a lateral AlN shell, results in the complete encapsulation of the NDs, giving rise to the carriers confinement. The lattice strain is induced by the asymmetric distribution of the radial AlN covering along the NWs, that additionally blue shifts the interband transition according to the coverage thickness. Consequently, the CL measurements performed show lower emission energies for those discs closer to the tip of the NWs than those near to the GaN stem.

In addition, the analyses of a series of samples with varying Ge concentrations, allows the study of the dynamics of the radiative processes in the 40 fold GaN / AlN NW system. The crystal quality is preserved despite of the inclusion of Ge dopant atoms. The long PL decay times of non doped samples are related to the radial component of the internal electric fields, mainly due to the uniaxial strain induced by the AlN coverage. However, the effect of internal electric fields (polarization induced) can be efficiently screened by Ge-doping, which also will affect the exciton lifetime, showing quick decays with increasing Ge concentrations.

The other type of structures analyzed deal with one single GaN disc in every NW, where we detailedly depicted the morphological aspects of the system, including the formation of self-assembled QSs. First, the influence of the growth time has been directly related to the obtained length of the forming sections. The faceting of the NDs, which are not hexagonal flat discs but dome-like axial segments, has been depicted. Based on the experimental observations, we find out that $\{1\bar{1}0\bar{l}\}$ planes complete the upper and bottom faceting, in agreement with the modeling and simulations performed.

Moreover, GaN self-assembled quantum structures developed within the AlN barriers are observed in both, the structural analyses and the CL spectra. The actual shape of such formations has been assessed by high resolution measurements performed in cross-sectional samples, obtained by cutting the NWs perpendicular to their axes, showing that the spontaneously formed GaN QSs within the barriers resemble wells partially surrounding the heterostructures. It is noteworthy to mention that the parasitic radial overgrowth of the AlN barrier while growing axially is connected to the induced strain of the disc by such covering.

Ge doped GaN single NDs have bee analyzed, too. The undoped and the doped NWs do not show structural differences at the atomic scale, while slightly higher emission energies are detected for Ge-doped samples, reaching 4.1 eV. Note that those bright emissions are mainly located within the AlN barriers, meaning that they are emerging from the GaN QSs present there.

CHAPTER 7

Conclusions and Outlook

7.1 General Conclusions

In this work we present a detailed characterization at atomic scale of a variety of non-planar semiconductor nanostructures. The analyses performed allow a better understanding of the growth mechanisms and electro-optical properties at the nanoscale of binary compound semiconductors, namely II-VI and III-V combinations. The atomic scale characterization is achieved by the use of (S)TEM techniques, mainly aberration-corrected HAADF and ABF. Such tools provide valuable information of the atoms in the structure, as the dumbbell orientation (polarity) or the lattice distortions (strain), that influence the growth as well as the final properties. We present the experimental results along with computer simulations calculated from atomic 3D models. Thanks to that, we can depict the morphological details of the systems, and achieving a deep understanding about their development. We started our study focusing on the unidirectional polar growth driving the formation of NWs and related branched nanostructures, continuing with the polarity influence in 2D like nanostructures. Then, we moved to the characterization of hetrostrucutres, where different materials are combined within the same NW, from radial/axial heterostructured wires, to quantum structures self-assembled in more complex systems. In the following, we present the main general conclusions achieved in this study.

In Chapter 3, we have conducted STEM experiments to address the polarity along the growth direction in NWs for the most commonly synthesized III-V and II-VI compounds. We have established a tandem procedure based on simultaneous HAADF and ABF imaging to resolve and identify the constituents of the dumbbells in a direct and accurate way. The analyses include GaN, GaP, GaAs, GaSb, InN, InAs, InP, InSb, ZnO, ZnTe, CdS, CdSe and CdTe NWs. We found out that, most of the compounds tend to grow along B-polar directions, except ZnO, which grows along A-polar and GaN, which shows one or the other depending on the sample. In fact, ZnO, GaN and InP are controversial materials in this context, since they have been reported to grow following both polarities. In our sought for a comprehensive explanation ruling the polar growth at the nanoscale, we have inspected several intrinsic parameters of the material constituents, that are related to the compound crystallography, such as the radii ratio of the constituents (comparing the covalent, ionic and atomic radii, separately) and the compound ionicity (following Pauling's and Phillips' definitions). Unfortunately, we have not identified a direct relationship between any of the properties analyzed and the observed unidirectional growth. However, the covalent ratio of the constituents might suggest a trend to growth following both polarities for the lowest relationships calculated (e.g., GaN, InN, InP), but it is not conclusive.

Hence, we have extended the study to the influence of the extrinsic parameters, as

the employed growth procedure. Interestingly, we could notice that the wires following opposite polar growths are usually governed by different thermodynamics/kinetics. After systematic comparisons of our experimental results with the literature, it is likely the growth procedure may influence the polarity of the structure (i.e., we have noticed that most of the wires growing under VLS conditions are B-polar while SAG procedures tend to result in A-polar wires). However, the local growth conditions around the growing event may differ from the overall used conditions, hindering the complete understanding.

Additionally, accounting for the preferred polarity observed for these materials, along with the polytypism and twinning phenomena, we have depicted the formation of a variety of nanostructures. In this context, we have presented the growth mechanisms of ZnTe NWs, tripods and tetrapods on non-polar substrates, i.e., mica. Therefore, the substrate will not induce any preferential polarity to the nucleation seeds, allowing the development of different nanostructures governed by the ruling polarity under the growth conditions used:

- ZnTe NWs synthesized at lower temperatures allow the formation of {110} lateral facets, resulting in hexagonal cross-setions, growing along ⟨111⟩B directions.
- At higher temperatures, the energy barrier for the formation of twin boundaries can be easily overcome. Consequently, the wires show high density of twin boundaries, that avoid the formation of lateral {110}, and lead to the growth of NWs with circular cross-sections. Despite the huge amount of twin boundaries observed, the B-polarity of the wires along the growth direction is always preserved.
- The formation of ZnTe tripods can be explained from the observation of A-polar nucleus and B-polar legs. A-polar nucleation events result in the formation of ZnTe {111} faceted octahedral seeds, exposing three available B-polar planes (the fourth one faces the substrate), allowing the growth of the legs of the tripods.
- ZnTe tetrapods are created from truncated octahedral nucleation seeds, where the occurrence of a twin boundary allows the formation of a complete octahedron attached to the former seed. The development of the four B-polar legs takes place along the {111}B polar facets of the seed.

In Chapter 4 we have expanded the polarity study to the cases of 2D-like nanostructures, such as ZnTe nanobelts and nanosheets, InAs V-shape membranes and InSb nanosails, with especial emphasis on the role of crystalline defects. We have also included one example regarding non-polar growth, Bi_2Te_3 nanoplates.

- Both, ZnTe nanobelts and sheets show an excellent crystal quality, achieving up to 7th order longitudinal optical phonon emission at room temperature. The main difference found in the optical response between both is the higher intensity of the

nanobelts compared to the nanosheets. Regarding their crystallinity, nanobelts follow {111}B polar growth, showing quasi periodic spaced twin boundaries perpendicular to their axes; whereas the less symmetric nanosheets grow along the non-polar $[1\overline{1}2]$ direction, showing longitudinal twins also along {111} planes. The lateral tapering of the sheets is observed mainly on the Te-polar lateral facet of the sheets, again in agreement with the B-polar preferred growth for the material.

- We have analyzed InAs V-shape nanomembranes, growing from triangular ZB nucleation seeds lying with the base on the substrate and laterally bordered by two {111}B planes, that allows the further elongation of the "wings"of the membrane. As consequence of the B-polar growth following divergent directions, there is an inversion boundary domain where both wings merge together. We have evaluated the influence of polar defects by first-principles calculations on the electronic structure and conductivity, showing the strong impact of the polarity reversal on the carrier transport.

- Also focusing on the crystallographic defects, we could understand the formation of InSb nanosails, due to the occurrence of one {111} twin boundary at one of the sides (extending parallel to one of the facets of the sail) that opens the growth front allowing the lateral expansion of the structure. We have achieved a huge understanding of the faceting by intensive inspections along with the development of an atomic 3D model, generalized for all the cases. The structures show unprecedented electrical properties, as electron mobilities four times larger than the best reported value for equivalent systems and 1D type transport, never reported for free-standing InSb systems.

- The formation of Bi_2Te_3 nanoplates is studied, mainly based on structural (atomic resolution HAADF) and compositional analyses (EELS). Despite of growing on top of thick amorphous layers (SiO_2), the plates are attached to the underlaying crystalline substrate (Silicon) by Te pinholes penetrating into the oxide coating. We have correlated the observation of these pinholes with the formation of a Te-rich vapor at the first stages that may create Te accumulations on the substrate, possibly diffusing into the oxide. After crystallizing, the Te pinholes act as seeds for the nucleation of the plates, that grow along the c-axis of the material.

In Chapter 5 we moved to the characterization of herostructured systems, i.e., NWs, combining highly mismatched materials stacked either radially or axially. We atomically analyzed the strain release mechanisms, which usually involve plastic and elastic lattice deformations. Importantly, some of these systems are reported to lack misfit dislocations, although they are theoretically predicted. The specific cases analyzed are summarized in the following:

- Radial InAs@GaAs core@shell NWs. Both materials crystallized in the WZ structure, growing along the $[000\bar{1}]$ directions. The GaAs lattice is strongly expanded (2.7 %) by the effect of the tensile strain induced by the lager InAs lattice structure in the core. The mismatch strain is partially released by the formation of misfit dislocations at the interface and a slight rotation of the growing plane in the InAs shell.

- Axial GaN/InN NWs. Both, the GaN and the InN lattices are completely relaxed (despite of the mismatch of $\sim$ 11 %) apart from the heterointerface, which is decorated with almost periodic misfit dislocations. Accounting for the dumb shape of the GaN tip at the interface with the InN allows a better interpretation of the data.

- Axial GaAs/GaSb NWs. Similar to the previous case, the morphology of the interface is not flat, as the GaAs stem firstly grown shows slightly sharp tips that are completely covered by the GaSb later grown, leading to a "core-shell" heterojunction. Both structures are completely relaxed (mismatch of 7.8 %) by the creation of misfit dislocations adopting the shape of the junction, and a small plane rotation through the edges of the NWs, especially are those regions with less dislocations.

- Axial InAs/InSb NWs. A flat interface defines the change from WZ to ZB in the structures, when switching the growth from the arsenide to the antimonide, creating a graded interface along the first 3-4 nm of the antimonide compound, which is actually $InAs_{1-x}Sb_x$ at that region. Assuming a Vegard's law behavior of the arsenide-antimonide system we could estimate the mean Sb concentration (15 % at. Sb). Another flat interface, but with dislocations radially centered separates the compressed ZB ($InAs_{1-x}Sb_x$) of the completely relaxed lattice (InSb). Through the edges of the wires, instead of dislocations, the relaxation is mainly elastic, as indicated the strong plane bending detected (8^o).

In Chapter 6 we deal with more complex heterostructures, created to spatially confine the carriers. The systems studied combined GaN active regions isolated by AlN barriers, created on top of GaN NW stems. Two different type systems were analyzed structurally and optically characterized, by means of aberration-corrected HAADF and CL-STEM techniques respectively.

- 40 fold period GaN NDs / AlN barriers axially stacked on top of GaN stems. The parasitic radial overgrowth of the AlN barrier results in the formation of an AlN shell burying totally the NDs, with a thickness gradient along the axis of the wire (thicker close to the stem and thinner through the tip), inducing an strain gradient to the GaN lattice. Thus, the NDs near the tip are less compressed and consequently emit at lower energies (CL emission) than those closer to the GaN

stem. Moreover, the relatively weak radial internal induced electric fields by the AlN shell, can be effectively screened by Ge doping, correlated, by the changes in the PL response. By increasing the Ge concentration within the tested range (up to $3.1 \cdot 10^{20} cm^{-3}$), the electrons and holes are radially confined through the center of the wires, resulting in shorter decay times, in addition to the observed blue shift.

- Single GaN disc contained in NWs grown on top of GaN/AlN NWs. In order to take advantage of the self-assembled approach just mentioned, samples with AlN barriers of different length and one thick GaN disc contained in each wire, were synthesized and characterized. The CL measurements performed, revealed the emission at the typical energy of GaN quantum structures around the AlN barrier region. The structural analyses at atomic scale performed, evidenced the presence of lateral GaN structures at the AlN region. However, the longitudinal projection of the wires do not allow the distinction among quantum wires and quantum wells. The ambiguity could be solved by studying the cross-section of a bunch of wires, that clearly shown the presence of inhomogeneous coaxial wells. A model regarding the morphology of the disc, which is not flat but convexed is also included. Similar samples but Ge-doped were analyzed, leading to the observation of luminescence from the disc for heavily doped samples.

7.2 Outlook

Our approach regarding the unidirectional polar growth at the nanoscale should be validated. However, the many parameters playing a role during the growth turn the task into a real challenge. Systematic in depth studies are needed, covering huge sets of growing conditions, in order to investigate as many scenarios as possible, and try to understand what and why can effectively induce one polar growth over the other.

Undoubtedly, the latter advances in STEM techniques and computer simulations, allow much detailed analyses, unveiling structural, chemical or morphological features, unnoticeable few years ago. Therefore, an enriched knowledge can be achieved both, over systems previously studied, or in newer synthesized systems.

In this context, it would be insightful to analyze the growth of nanostructures by using the newer or future *in-situ* instruments, achieving atomic resolution, while reproducing, as far as possible, the growth conditions achieved by the different procedures, in order to shed light into the reported issues here, as the polar growth, the defect formation and development of the structures, or the matching between different materials.

Moreover, more work must be done to experimentally address the effect of a polarity inversion within these nanometric structures in their transport properties, theoretically predicted to be dramatically affected.

Bibliography

[1] I Vurgaftman, J R Meyer, and L R Ram-Mohan. Band parameters for III-V compound semiconductors and their alloys. *Journal of Applied Physics*, 89:5815, 2001.

[2] D W Palmer. The Semiconductor-Information Web-Site, 1999. http://www.semiconductors.co.uk.

[3] P Rinke, M Scheffler, A Qteish, M Winkelnkemper, D Bimberg, and J Neugebauer. Band gap and band parameters of InN and GaN from quasiparticle energy calculations based on exact-exchange density-functional theory. *Applied Physics Letters*, 89:22–24, 2006.

[4] H J Queisser. Defects in Semiconductors: Some Fatal, Some Vital. *Science*, 281:945–950, 1998.

[5] C D Bessire, M T Björk, H Schmid, A Schenk, K B Reuter, and H Riel. Trap-assisted tunneling in Si-InAs nanowire heterojunction tunnel diodes. *Nano Letters*, 11:4195–4199, 2011.

[6] M Hjort, S Lehmann, J Knutsson, R Timm, D Jacobsson, E Lundgren, K A Dick, and A Mikkelsen. Direct Imaging of Atomic Scale Structure and Electronic Properties of GaAs Wurtzite and Zinc Blende Nanowire Surfaces. *Nano Letters*, 13:4492–4498, 2013.

[7] Z Ikonić, G P Srivastava, and J C Inkson. Electronic properties of twin boundaries and twinning superlattices in diamond-type and zinc-blende-type semiconductors. *Physical Review Bl*, 48(23):17181, 1993.

[8] Z Ikonić, G P Srivastava, and J C Inkson. Optical properties of twinning superlattices in diamond-type and zinc-blende-type semiconductors. *Physical Review B*, 52:1478–1485, 1995.

[9] R E Algra, M A Verheijen, M T Borgström, L-F Feiner, G Immink, W J P van Enckevort, E Vlieg, and E P A M Bakkers. Twinning superlattices in indium phosphide nanowires. *Nature*, 456:369–372, 2008.

[10] M H Huang, S Mao, H Feick, H Yan, Y Wu, H Kind, E Weber, R Russo, and P Yan. Room-Temperature Ultraviolet Nanowire Nanolasers. *Science*, 292:1897–1899, 2001.

[11] J C Johnson, H-J Choi, K P Knutsen, R D Schaller, P Yang, and R J Saykally. Single gallium nitride nanowire lasers. *Nature Materials*, 1:106–110, 2002.

[12] X Duan, Y Huang, R Agarwal, and C M Lieber. Single-nanowire electrically driven lasers. *Nature*, 421:241–245, 2003.

[13] L Novotny and N van Hulst. Antennas for light. *Nature Photonics*, 5:83–90, 2011.

[14] J Wang, M S Gudiksen, X Duan, Y Cui, and C M Lieber. Highly Polarized Photoluminescence and Photodetection from Single Indium Phosphide Nanowires. *Science*, 293:1455–1458, 2001.

[15] B H Kind, H Yan, B Messer, M Law, and P Yang. Nanowire Ultraviolet Photodetectors and Optical. *Advanced Materials*, 14:158–160, 2002.

[16] Y Gu, E-S Kwak, J L Lensch, J E Allen, T W Odom, and L J Lauhon. Near-field scanning photocurrent microscopy of a nanowire photodetector. *Applied Physics Letters*, 87:043111, 2005.

[17] X Duan, Y Huang, Y Cui, J Wang, and C L Lieber. Indium phosphide nanowires as building blocks for nanoscale electronic and optoelectronic devices. *Nature*, 409:66–69, 2001.

[18] Z Zhong, F Qian, D Wang, and C M Lieber. Synthesis of p-Type Gallium Nitride Nanowires for Electronic and Photonic Nanodevices. *Nano Letters*, 3:343–346, 2003.

[19] F Qian, Y Li, S Gradec, D Wang, C J Barrelet, and C M Lieber. Gallium Nitride-Based Nanowire Radial Heterostructures for Nanophotonics. *Nano Letters*, 4:1975–1979, 2004.

[20] D X Huang, C L Chen, and A J Jacobson. Interface structures and periodic film distortions induced by substrate-surface steps in Gd-doped ceria thin-film growth. *Journal of Applied Physics*, 97:043506, 2005.

[21] M Law, L E Greene, J C Johnson, R Saykally, and P Yang. Nanowire dye-sensitized solar cells. *Nature Materials*, 4:455–459, 2005.

[22] B M Kayes, H A Atwater, and N S Lewis. Comparison of the device physics principles of planar and radial p-n junction nanorod solar cells. *Journal of Applied Physics*, 97:114302, 2005.

[23] B Tian, X Zheng, T J Kempa, Y Fang, N Yu, G Yu, J Huang, and C M Lieber. Coaxial silicon nanowires as solar cells and nanoelectronic power sources. *Nature*, 449:885–889, October 2007.

[24] P Krogstrup, H I Jørgensen, M Heiss, O Demichel, J V Holm, M Aagesen, J Nygard, and A Fontcuberta i Morral. Single-nanowire solar cells beyond the Shockley-Queisser limit. *Nature Photonics*, 7:306–310, March 2013.

[25] J Teubert, P Becker, F Furtmayr, and M Eickhoff. GaN nanodiscs embedded in nanowires as optochemical transducers. *Nanotechnology*, 22:275505, 2011.

[26] J Wallys, J Teubert, F Furtmayr, D M Hofmann, and M Eickhoff. Bias-Enhanced Optical pH Response of Group III- Nitride Nanowires. *Nano Letters*, 4:6180–6186, 2012.

[27] V Mourik, K Zuo, S M Frolov, S R Plissard, E P A M Bakkers, and L P Kouwenhoven. Signatures of Majorana fermions in hybrid superconductor-semiconductor nanowire devices. *Science*, 336:1003–1007, 2012.

[28] M T Deng, C L Yu, G Y Huang, M Larsson, P Caroff, and H Q Xu. Anomalous zero-bias conductance peak in a Nb-InSb nanowire-Nb hybrid device. *Nano Letters*, 12:6414–6419, 2012.

[29] G Chen, G Sun, Y J Ding, P Prete, I Miccoli, N Lovergine, H Shtrikman, P Kung, T Livneh, and J E Spanier. Direct Measurement of Band Edge Discontinuity in Individual Core - Shell Nanowires by Photocurrent Spectroscopy. *Nano Letters*, 13:4152–4157, 2013.

[30] K Wang, S C Rai, J Marmon, J Chen, K Yao, S Wozny, B Cao, Y Yan, Y Zhang, and W Zhou. Nearly lattice matched all wurtzite CdSe/ZnTe type II core-shell nanowires with epitaxial interfaces for photovoltaics. *Nanoscale*, 6:3679–3685, 2014.

[31] R Yan, S Fathipour, Y Han, B Song, S Xiao, M Li, V Protasenko, D A Muller, D Jena, and H G Xing. Esaki diodes in van der Waals heterojunctions with broken-gap energy band alignment. *Nano Letters*, 2015.

[32] B M Borg, K A Dick, B Ganjipour, M-E Pistol, L-E Wernersson, and C Thelander. InAs/GaSb heterostructure nanowires for tunnel field-effect transistors. *Nano Letters*, 10:4080–7085, 2010.

[33] A Hospodková, M Zíková, J Pangrác, J Oswald, J Kubištová, K Kuldová, P Hazdra, and E Hulicius. Type I-type II band alignment of a GaAsSb/InAs/GaAs quantum dot heterostructure influenced by dot size and strain-reducing layer composition. *Journal of Physics D: Applied Physics*, 46:095103, 2013.

[34] K A Dick, J Bolinsson, B M Borg, and J Johansson. Controlling the Abruptness of Axial Heterojunctions in III-V Nanowires: Beyond the Reservoir Effect. *Nano Letters*, 12:3200–3206, 2012.

[35] C-Y Wen, M C Reuter, J Bruley, J Tersoff, S Kodambaka, E A Stach, and F M Ross. Formation of Compositionally Abrupt Axial Heterojunctions in Silicon-Germanium Nanowires. *Science*, 326:1247–1250, 2009.

[36] P Krogstrup, J Yamasaki, C B Sø rensen, E Johnson, J B Wagner, R Pennington, M Aagesen, N Tanaka, and J Nygå rd. Junctions in axial III-V heterostructure nanowires obtained via an interchange of group III elements. *Nano Letters*, 9:3689–3693, 2009.

[37] M Paladugu, J Zou, Y-N Guo, X Zhang, Y Kim, H J Joyce, Q Gao, H H Tan, and C Jagadish. Nature of heterointerfaces in GaAs/InAs and InAs/GaAs axial nanowire heterostructures. *Applied Physics Letters*, 93:101911, 2008.

[38] T Akiyama, T Yamashita, K Nakamura, and T Ito. Band alignment tuning in twin-plane superlattices of semiconductor nanowires. *Nano Letters*, 10:4614–4618, 2010.

[39] X Fu, G Jacopin, M Shahmohammadi, R Liu, M Benameur, J-D Ganiére, W Guo, Z-M Liao, B Deveaud, and D. Yu. Exciton Drift in Semiconductors under Uniform Strain Gradients: Application to Bent ZnO Microwires. *ACS Nano*, 8:3412–3420, 2014.

[40] D Li, Y Liu, M de la Mata, C Magen, J Arbiol, Y Feng, and Q Xiong. Strain-induced spatially indirect exciton recombination in zinc-blende/wurtzite CdS heterostructures. *Nano Research*, 10.1007/s12274-015-0809-8, 2015.

[41] F Schuster, B Laumer, R Zamani, J Arbiol, and M Stutzmann. p-GaN / n-ZnO heterojunction nanowires for UV-LEDs including simulations of the polarity-dependent bandstructure. *ACS Nano*, 8:4376–4384, 2014.

[42] J Arbiol, M de la Mata, M Eickhoff, and Anna Fontcuberta i Morral. Bandgap engineering in a nanowire: self-assembled 0, 1 and 2D quantum structures. *Materials Today*, 16:213–219, 2013.

[43] A Fontcuberta i Morral, D Spirkoska, J Arbiol, M Heigoldt, J R Morante, and G Abstreiter. Prismatic quantum heterostructures synthesized on molecular-beam

epitaxy GaAs nanowires. *Small (Weinheim an der Bergstrasse, Germany)*, 4:899–903, 2008.

[44] M Heigoldt, J Arbiol, D Spirkoska, J M Rebled, S Conesa-Boj, G Abstreiter, F Peiró, J R Morante, and A Fontcuberta i Morral. Long range epitaxial growth of prismatic heterostructures on the facets of catalyst-free GaAs nanowires. *Journal of Materials Chemistry*, 19:840, 2009.

[45] F Qian, Y Li, S Gradecak, H-G Park, Y Dong, Y Ding, Z L Wang, and C M Lieber. Multi-quantum-well nanowire heterostructures for wavelength-controlled lasers. *Nature Materials*, 7:701–706, 2008.

[46] R Koester, J-S Hwang, D Salomon, X Chen, C Bougerol, J-P Barnes, D L S Dang, L Rigutti, A de Luna Bugallo, G Jacopin, M Tchernycheva, C Durand, and Jl Eymery. M-plane core-shell InGaN/GaN multiple-quantum-wells on GaN wires for electroluminescent devices. *Nano Letters*, 11, 2011.

[47] L Rigutti, M Tchernycheva, A De Luna Bugallo, G Jacopin, F H Julien, F Furtmayr, M Stutzmann, M Eickhoff, R Songmuang, and F Fortuna. Photoluminescence polarization properties of single GaN nanowires containing $Al_xGa_{1-x}N$/GaN quantum discs. *Physical Review B*, 81:045411, 2010.

[48] R Songmuang, T Ben, B Daudin, D González, and E Monroy. Identification of III-N nanowire growth kinetics via a marker technique. *Nanotechnology*, 21:295605, 2010.

[49] L F Zagonel, L Rigutti, M Tchernycheva, G Jacopin, R Songmuang, and M Kociak. Visualizing highly localized luminescence in GaN/AlN heterostructures in nanowires. *Nanotechnology*, 23:455205, 2012.

[50] S Deshpande, T Frost, L Yan, S Jahangir, A Hazari, X Liu, J Mirecki-Millunchick, Z Mi, and P Bhattacharya. Formation and Nature of InGaN Quantum Dots in GaN Nanowires. *Nano Letters*, 15:1647–1653, 2015.

[51] T Kehagias, G P Dimitrakopulos, P Becker, J Kioseoglou, F Furtmayr, T Koukoula, I Häusler, A Chernikov, S Chatterjee, T Karakostas, H-M Solowan, U T Schwarz, M Eickhoff, and P Komninou. Nanostructure and strain in InGaN/GaN superlattices grown in GaN nanowires. *Nanotechnology*, 24:435702, 2013.

[52] F Furtmayr, J Teubert, P Becker, S Conesa-Boj, J R Morante, A Chernikov, S Schäfer, S Chatterjee, J Arbiol, and M Eickhoff. Carrier confinement in GaN/$Al_xGa_{1-x}N$ nanowire heterostructures ($0 < x \leq 1$). *Physical Review B*, 84:205303, 2011.

[53] S Koshiba, H Noge, H Akiyama, T Inoshita, Y Nakamura, A. Shimizu, Y. Nagamune, M Tsuchiya, H Kano, H Sakaki, and K Wada. Formation of GaAs ridge quantum wire structures by molecular beam epitaxy on patterned substrates. *Applied Physics Letters*, 64(1994):363–365, 1994.

[54] P Kröger, M Ruth, N Weber, and C Meier. Carrier localization in ZnO quantum wires. *Applied Physics Letters*, 100:263114, 2012.

[55] H-J Choi, J C Johnson, R He, S-K Lee, F Kim, P Pauzauskie, J Goldberger, R J. Saykally, and P Yang. Self-Organized GaN Quantum Wire UV Lasers. *The Journal of Physical Chemistry B*, 107:8721–8725, 2003.

[56] J Arbiol, C Magen, P Becker, G Jacopin, A Chernikov, S Schäfer, F Furtmayr, M Tchernycheva, L Rigutti, J Teubert, S Chatterjee, J R Morante, and M Eickhoff. Self-assembled GaN quantum wires on GaN/AlN nanowire templates. *Nanoscale*, 4:7517–7524, 2012.

[57] M de la Mata, X Zhou, F Furtmayr, J Teubert, S Gradečak, M Eickhoff, A Fontcuberta i Morral, and J Arbiol. A review of MBE grown 0D, 1D and 2D quantum structures in a nanowire. *Journal of Materials Chemistry C*, 1:4300, 2013.

[58] C Colombo, D Spirkoska, M Frimmer, G Abstreiter, and A Fontcuberta i Morral. Ga-assisted catalyst-free growth mechanism of GaAs nanowires by molecular beam epitaxy. *Physical Review B*, 77:155326, 2008.

[59] E Uccelli, J Arbiol, J R Morante, and A Fontcuberta i Morral. InAs quantum dot arrays decorating the facets of GaAs nanowires. *ACS nano*, 4:5985–5993, 2010.

[60] L-X Lu, M S Bharathi, and Y-W Zhang. Self-assembly of ordered epitaxial nanostructures on polygonal nanowires. *Nano Letters*, 13:538–542, 2013.

[61] X Yan, X Zhang, X Ren, X Lv, J Li, Q Wang, S Cai, and Y Huang. Formation mechanism and optical properties of InAs quantum dots on the surface of GaAs nanowires. *Nano Letters*, 12:1851–1856, 2012.

[62] M Heiss, Y Fontana, a Gustafsson, G Wüst, C Magen, D D O'Regan, J W Luo, B Ketterer, S Conesa-Boj, a V Kuhlmann, J Houel, E Russo-Averchi, J R Morante, M Cantoni, N Marzari, J Arbiol, a Zunger, R J Warburton, and A Fontcuberta i Morral. Self-assembled quantum dots in a nanowire system for quantum photonics. *Nature Materials*, 12:439–444, 2013.

[63] D B Williams and C B Carter. *Transmission Electron Microscopy*. Springer New York, 1996.

[64] M Haider, H Rose, S Uhlemann, E Schwan, B Kabius, and K Urban. A spherical-aberration-corrected 200 kV transmission electron microscope. *Ultramicroscopy*, 75:53–60, 1998.

[65] O L Krivanek, N Dellby, A J Spence, R A Camps, and L M Brown. Aberration correction in the STEM. *Proceedings of Conf. EMAG97*, pages 35–40, 1997.

[66] A V Crewe, Wall J, and J Langmore. Visibility of Single Atoms. *Science*, 168:1338–1340, 1970.

[67] Z W Wang, Z Y Li, S J Park, A Abdela, D Tang, and R E Palmer. Quantitative Z-contrast imaging in the scanning transmission electron microscope with size-selected clusters. *Physical Review B*, 84:073408, 2011.

[68] P D Nellist and S J Pennycook. Incoherent imaging using dynamically scattered coherent electrons. *Ultramicroscopy*, 78:111–124, 1999.

[69] M de la Mata, C Magen, J Gazquez, M I B Utama, M Heiss, S Lopatin, F Furtmayr, C J Fernández-Rojas, B Peng, J R Morante, R Rurali, M Eickhoff, A Fontcuberta i Morral, Q Xiong, and J Arbiol. Polarity assignment in ZnTe, GaAs, ZnO, and GaN-AlN nanowires from direct dumbbell analysis. *Nano Letters*, 12:2579–2586, 2012.

[70] R Ishikawa, E Okunishi, H Sawada, Y Kondo, F Hosokawa, and E Abe. Direct imaging of hydrogen-atom columns in a crystal by annular bright-field electron microscopy. *Nature Materials*, 10:278–281, 2011.

[71] S D Findlay, N Shibata, H Sawada, E Okunishi, Y Kondo, and Y Ikuhara. Dynamics of annular bright field imaging in scanning transmission electron microscopy. *Ultramicroscopy*, 110:903–923, 2010.

[72] E Okunishi, I Ishikawa, H Sawada, F Hosokawa, M Hori, Y Kondo, and Bright Field Microscopy. Visualization of Light Elements at Ultrahigh Resolution by STEM Annular Bright Field Microscopy. *Microscopy and Microanalysis*, 15:164, 2009.

[73] S D Findlay, N Shibata, H Sawada, E Okunishi, Y Kondo, T Yamamoto, and Y Ikuhara. Robust atomic resolution imaging of light elements using scanning transmission electron microscopy. *Applied Physics Letters*, 95:191913, 2009.

[74] V Grillo and F Rossi. A new insight on crystalline strain and defect features by STEM-ADF imaging. *Journal of Crystal Growth*, 318:1151–1156, 2011.

[75] P J Phillips, M De Graef, L Kovarik, A Agrawal, W Windl, and M J Mills. Atomic-resolution defect contrast in low angle annular dark-field STEM. *Ultramicroscopy*, 116:47–55, 2012.

[76] M Ohtsuka, T Yamazaki, Y Kotaka, I Hashimoto, and K Watanabe. Imaging of light and heavy atomic columns by spherical aberration corrected middle-angle bright-field STEM. *Ultramicroscopy*, 120:48–55, 2012.

[77] Y Kotaka. Direct visualization method of the atomic structure of light and heavy atoms with double-detector Cs-corrected scanning transmission electron microscopy. *Applied Physics Letters*, 101:133107, 2012.

[78] Challa S S R Kumar. *Transmission Electron Microscopy Characterization of Nanomaterials*. Springer Berlin Heidelberg, Berlin, Heidelberg. Chapter 9 (pp. 375-425): High Resolution in STEM Mode: Individual Atom Analysis in Semiconductor Nanowires; M de la Mata, J Arbiol.

[79] R F Egerton. *Electron energy-loss spectroscopy in the electron microscope*. Springer New York, third edition, 2011.

[80] H Tan, S Turner, E Yücelen, J Verbeeck, and G van Tendeloo. 2D Atomic Mapping of Oxidation States in Transition Metal Oxides by Scanning Transmission Electron Microscopy and Electron Energy-Loss Spectroscopy. *Physical Review Letters*, 107:107602, 2011.

[81] D A Muller, L F Kourkoutis, M Murfitt, J H Song, H Y Hwang, J Silcox, N Dellby, and O L Krivanek. Atomic-scale chemical imaging of composition and bonding by aberration-corrected microscopy. *Science*, 319:1073–1076, 2008.

[82] M Bosman, M Watanabe, D T L Alexander, and V J Keast. Mapping chemical and bonding information using multivariate analysis of electron energy-loss spectrum images. *Ultramicroscopy*, 106:1024–1032, 2006.

[83] S Turner, J Verbeeck, F Ramezanipour, J E Greedan, G van Tendeloo, and G A Botton. Atomic Resolution Coordination Mapping in Ca_2FeCoO_5 Brownmillerite by Spatially Resolved Electron Energy-Loss Spectroscopy. *Chemistry of Materials*, 24:1904–1909, 2012.

[84] J Nelayah, M Kociak, O Stéphan, F J García de Abajo, M Tencé, L Henrard, Dario Taverna, I Pastoriza-Santos, L M Liz-Marzán, and C Colliex. Mapping surface plasmons on a single metallic nanoparticle. *Nature Physics*, 3(5):348–353, 2007.

[85] M Bosman, V J Keast, M Watanabe, A I Maaroof, and M B Cortie. Mapping surface plasmons at the nanometre scale with an electron beam. *Nanotechnology*, 18:165505, 2007.

[86] E Snoeck, B Warot, H Ardhuin, A Rocher, M J Casanove, R Kilaas, and M J Hytch. Quantitative analysis of strain field in thin films from HRTEM micrographs. *Thin Solid Films*, pages 157–162, 1998.

[87] Pe L Galindo, S Kret, A M Sanchez, J-Y Laval, A Yáñez, J Pizarro, E Guerrero, T Ben, and S I Molina. The Peak Pairs algorithm for strain mapping from HRTEM images. *Ultramicroscopy*, 107:1186–1193, 2007.

[88] V Grillo and E Rotunno. STEM_CELL: a software tool for electron microscopy: part 1–simulations. *Ultramicroscopy*, 125:97–111, 2013.

[89] E J Kirkland. *Advanced Computing in Electron Microscopy*. Springer New York, 1998.

[90] S Bernal, F J Botana, J J Calvino, C Lo, and J A Pe. The interpretation of HREM images of supported metal catalysts using image simulation: profile view images. *Ultramicroscopy*, 72:135–164, 1998.

[91] J Arbiol, A Fontcuberta i Morral, S Estrade, F Peiro, B Kalache, P Roca i Cabarrocas, and J R Morante. Influence of the (111) twinning on the formation of diamond cubic/diamond hexagonal heterostructures in Cu-catalyzed Si nanowires. *Journal of Applied Physics*, 104:064312, 2008.

[92] D Cohen, S McKernan, and C Carter. Characterization of the Absolute Crystal Polarity across Twin Boundaries in Gallium Phosphide Using Convergent-Beam Electron Diffraction. *Microscopy and Microanalysis*, 5:173–186, 1999.

[93] J Arbiol, S Estradé, J D Prades, A Cirera, F Furtmayr, Ch Stark, A Laufer, M Stutzmann, M Eickhoff, M H Gass, A L Bleloch, F Peiró, and J R Morante. Triple-twin domains in Mg doped GaN wurtzite nanowires: structural and electronic properties of this zinc-blende-like stacking. *Nanotechnology*, 20:145704, 2009.

[94] L S Ramsdell. Studies on silicon carbide. *American Mineralogist*, 32:64–82, 1947.

[95] H J Joyce, J Wong-Leung, Q Gao, H H Tan, and C Jagadish. Phase perfection in zinc Blende and Wurtzite III-V nanowires using basic growth parameters. *Nano Letters*, 10:908–915, 2010.

[96] K Pemasiri, M Montazeri, R Gass, L M Smith, H E Jackson, J Yarrison-Rice, S Paiman, Q Gao, H H Tan, C Jagadish, X Zhang, and J Zou. Carrier dynamics and quantum confinement in type II ZB-WZ InP nanowire homostructures. *Nano Letters*, 9:648–654, 2009.

[97] D Spirkoska, J Arbiol, A Gustafsson, S Conesa-Boj, F Glas, I Zardo, M Heigoldt, M H Gass, A L Bleloch, S Estrade, M Kaniber, J Rossler, F Peiro, J R Morante, G Abstreiter, L Samuelson, and A Fontcuberta i Morral. Structural and optical properties of high quality zinc-blende/wurtzite GaAs nanowire heterostructures. *Physical Review B*, 80:245325, 2009.

[98] J Bao, D C Bell, F Capasso, J B Wagner, T Mårtensson, J Trägårdh, and L Samuelson. Optical properties of rotationally twinned InP nanowire heterostructures. *Nano Letters*, 8:836–841, 2008.

[99] M Heiss, S Conesa-Boj, J Ren, H-H Tseng, A Gali, A Rudolph, E Uccelli, F Peiró, J R Morante, D Schuh, E Reiger, E Kaxiras, J Arbiol, and A Fontcuberta i Morral. Direct correlation of crystal structure and optical properties in wurtzite/zinc-blende GaAs nanowire heterostructures. *Physical Review B*, 83:045303, 2011.

[100] L Jin, J Wang, S Jia, Q Jiang, X Yan, P Lu, Y Cai, L Deng, and W C H Choy. ZnSe heterocrystalline junctions based on zinc blende-wurtzite polytypism. *Journal of Physical Chemistry C*, 114:1411–1415, 2010.

[101] D Kriegner, C Panse, B Mandl, K A Dick, M Keplinger, J M Persson, P Caroff, D Ercolani, L Sorba, F Bechstedt, J Stangl, and G Bauer. Unit cell structure of crystal polytypes in InAs and InSb nanowires. *Nano Letters*, 11:1483–1489, 2011.

[102] A Urban, J Malindretos, and P Simon. Ga-polar GaN nanocolumn arrays with semipolar faceted tips. *New Journal of Physics*, 15:053045, 2013.

[103] S A Chevtchenko, J C Moore, U Ozgur, X Gu, A A Baski, H Morkoc, B Nemeth, and J E Nause. Comparative study of the (0001) and (000$\bar{1}$) surfaces of ZnO. *Applied Physics Letters*, 89:182111, 2006.

[104] M Losurdo and M M Giangregorio. Interaction of atomic hydrogen with Zn-polar and O-polar ZnO surfaces. *Applied Physics Letters*, 86:091901, 2005.

[105] Yufeng Dong, Z.-Q. Fang, D. C. Look, D. R. Doutt, M. J. Hetzer, and L. J. Brillson. Polarity-related asymetry at ZnO surfaces and metal interfaces. *Journal of Vacuum Science & Technology B*, 27:1710, 2009.

[106] Y-L Lai, C-P Liu, Y-H Lin, R-M Lin, D-Y Lyu, Z-X Peng, and T-Y Lin. Effects of the material polarity on the green emission properties of InGaN/GaN multiple quantum wells. *Applied Physics Letters*, 89:151906, 2006.

[107] K Ikejiri, F Ishizaka, K Tomioka, and T Fukui. Bidirectional growth of indium phosphide nanowires. *Nano Letters*, 12:4770–4774, 2012.

[108] F Schuster, M Hetzl, S Weiszer, J A Garrido, M de la Mata, C Magen, J Arbiol, and M Stutzmann. Position-Controlled Growth of GaN Nanowires and Nanotubes on Diamond by Molecular Beam Epitaxy. *Nano Letters*, 15:1773–1779, 2015.

[109] L S Karlsson, K A Dick, J B Wagner, J-O Malm, K Deppert, L Samuelson, and L R Wallenberg. Understanding the 3D structure of GaAs [111] B nanowires. *Nanotechnology*, 18:485717, 2007.

[110] U Krishnamachari, M B Borgstrom, B J Ohlsson, N Panev, L Samuelson, W Seifert, M W Larsson, and L R Wallenberg. Defect-free InP nanowires grown in [001] direction on InP (001). *Applied Physics Letters*, 85:2077, 2004.

[111] A Fontcuberta i Morral, C Colombo, G Abstreiter, J Arbiol, and J R Morante. Nucleation mechanism of gallium-assisted molecular beam epitaxy growth of gallium arsenide nanowires. *Applied Physics Letters*, 92:063112, 2008.

[112] G Binning, H Rohrer, C Gerber, and E Weibel. Surface Studies by Scanning Tunneling Microscopy. *Physical Review Letters*, 49:57–61, 1982.

[113] J Bolinsson, L Ouattara, W a Hofer, N Sköld, E Lundgren, a Gustafsson, and A Mikkelsen. Direct observation of atomic scale surface relaxation in ortho twin structures in GaAs by XSTM. *Journal of physicsl*, 21:055404, 2009.

[114] A Mikkelsen, N Sköld, L Ouattara, M Borgström, J N Andersen, L Samuelson, W Seifert, and E Lundgren. Direct imaging of the atomic structure inside a nanowire by scanning tunnelling microscopy. *Nature Materials*, 3:519–523, 2004.

[115] T Xu, K A Dick, S Plissard, T H Nguyen, Y Makoudi, M Berthe, J-P Nys, X Wallart, B Grandidier, and P Caroff. Faceting, composition and crystal phase evolution in III-V antimonide nanowire heterostructures revealed by combining microscopy techniques. *Nanotechnology*, 23:095702, 2012.

[116] N D Browing, M F Chisholm, and S. J. Pennycook. Atomic-resolution chemical analysis using a scanning transmission electron microscope. *Nature*, 366:143–146, 1993.

[117] A Carretero-Genevrier, J Gázquez, J C Idrobo, J Oró, J Arbiol, M Varela, E Ferain, J Rodríguez-Carvajal, T Puig, N Mestres, and X Obradors. Single crystalline $La_{0.7}Sr_{0.3}MnO_3$ molecular sieve nanowires with high temperature ferromagnetism. *Journal of the American Chemical Society*, 133:4053–4061, 2011.

[118] A J D'Alfonso, B Freitag, D Klenov, and L J Allen. Atomic-resolution chemical mapping using energy-dispersive x-ray spectroscopy. *Physical Review B*, 81:100101(R), 2010.

[119] X Kong, J Ristić, M A Sanchez-Garcia, E Calleja, and A Trampert. Polarity determination by electron energy-loss spectroscopy: application to ultra-small III-nitride semiconductor nanocolumns. *Nanotechnology*, 22:415701, 2011.

[120] J B Baxter, F Wu, and E S Aydil. Growth mechanism and characterization of zinc oxide hexagonal columns. *Applied Physics Letters*, 83:3797, 2003.

[121] C Kisielowski, C J D Hetherington, Y C Wang, R Kilaas, M A O'Keefe, and A Thust. Imaging columns of the light elements carbon , nitrogen and oxygen with sub Angstrom resolution. *Ultramicroscopy*, 89:243–263, 2001.

[122] M J Polking, J J Urban, D J Milliron, H Zheng, E Chan, M A Caldwell, S Raoux, C F Kisielowski, J W Ager, R Ramesh, and A P Alivisatos. Size-dependent polar ordering in colloidal GeTe nanocrystals. *Nano Letters*, 11:1147–1152, 2011.

[123] M Wagner, T Bartel, R Kirste, A Hoffmann, J Sann, S Lautenschläger, B Meyer, and C Kisielowski. Influence of substrate surface polarity on homoepitaxial growth of ZnO layers by chemical vapor deposition. *Physical Review B*, 79:035307, 2009.

[124] F Furtmayr, M Vielemeyer, M Stutzmann, J Arbiol, S Estradé, Francesca Peiró, J R Morante, and M Eickhoff. Nucleation and growth of GaN nanorods on Si (111) surfaces by plasma-assisted molecular beam epitaxy - The influence of Si- and Mg-doping. *Journal of Applied Physics*, 104:034309, 2008.

[125] Ai Koma. Van der Waals epitaxy for highly lattice-mismatched systems. *Journal of Crystal Growth*, 201-202:236–241, 1999.

[126] M I B Utama, Z Peng, R Chen, B Peng, X Xu, Y Dong, M Wong, S Wang, H Sun, and Q Xiong. Vertically Aligned Cadmium Chalcogenide Nanowire Arrays on Muscovite Mica: A Demonstration of Epitaxial Growth Strategy. *Nano Letters*, 11:3051–3057, 2011.

[127] M I B Utama, F J Belarre, C Magen, B Peng, J Arbiol, and Q Xiong. Incommensurate van der Waals Epitaxy of Nanowire Arrays: A Case Study with ZnO on Muscovite Mica Substrates. *Nano Letters*, 12:2146–2152, 2012.

[128] F Glas, J-C Harmand, and G Patriarche. Why Does Wurtzite Form in Nanowires of III-V Zinc Blende Semiconductors? *Physical Review Letters*, 99:3–6, 2007.

[129] P Caroff, J Bolinsson, and J Johansson. Crystal Phases in III-V Nanowires: From Random Toward Engineered Polytypism. *IEEE Journal of Selected Topics in Quantum Electronics*, 17:829–846, 2011.

[130] K A Dick, P Caroff, J Bolinsson, M E Messing, J Johansson, K Deppert, L R Wallenberg, and L Samuelson. Control of III-V nanowire crystal structure by

growth parameter tuning. *Semiconductor Science and Technology*, 25:024009, 2010.

[131] Neimantas Vainorius, Sebastian Lehmann, Daniel Jacobsson, Lars Samuelson, Kimberly a. Dick, and Mats-Erik Pistol. Confinement in Thickness-Controlled GaAs Polytype Nanodots. *Nano Letters*, 15:2652–2656, 2015.

[132] S Plissard, K A Dick, G Larrieu, S Godey, A Addad, X Wallart, and P Caroff. Gold-free growth of GaAs nanowires on silicon: arrays and polytypism. *Nanotechnology*, 21:385602, 2010.

[133] D Cherns, L Meshi, I Griffiths, S Khongphetsak, S V Novikov, N Farley, R P Campion, and C T Foxon. Defect reduction in GaN/(0001)sapphire films grown by molecular beam epitaxy using nanocolumn intermediate layers. *Applied Physics Letters*, 92:121902, 2008.

[134] B Alloing, S Vézian, O Tottereau, P Vennéguès, E Beraudo, and J Zuniga-Pérez. On the polarity of GaN micro- and nanowires epitaxially grown on sapphire (0001) and Si(111) substrates by metal organic vapor phase epitaxy and ammonia-molecular beam epitaxy. *Applied Physics Letters*, 98:011914, 2011.

[135] M D Brubaker, I Levin, A V Davydov, D M Rourke, N A Sanford, V M Bright, and K A Bertness. Effect of AlN buffer layer properties on the morphology and polarity of GaN nanowires grown by molecular beam epitaxy. *Journal of Applied Physics*, 110:053506, 2011.

[136] S Fernández-Garrido, X Kong, T Gotschke, R Calarco, L Geelhaar, A Trampert, and O Brandt. Spontaneous nucleation and growth of GaN nanowires: the fundamental role of crystal polarity. *Nano Letters*, 12:6119–6125, 2012.

[137] S D Carnevale, T F Kent, P J Phillips, A T M G Sarwar, C Selcu, R F Klie, and R C Myers. Mixed Polarity in Polarization-Induced p-n Junction Nanowire Light-Emitting Diodes. *Nano Letters*, 13:3029–3025, 2013.

[138] H C Gatos. Dangling Bonds in III-V Compounds. *Journal of Applied Physics*, 32:1232–1234, 1961.

[139] E P Warekois, M C Lavine, A N Mariano, and H C Gatos. Crystallographic polarity in the II-VI compounds. *Journal of Applied Physics*, 33:690–696, 1962.

[140] J C Phillips. Ionicity of the Chemical Bond in Crystals. *Reviews of Modern Physics*, 42:317–356, 1970.

[141] R S Wagner and W C Ellis. Vapor-liquid-solid mechanism of single crystal growth. *Applied Physics Letters*, 4(1964):89–90, 1964.

[142] P J Poole, J Lefebvre, and J Fraser. Spatially controlled, nanoparticle-free growth of InP nanowires. *Applied Physics Letters*, 83:2055, 2003.

[143] Q Gao, D Saxena, F Wang, L Fu, S Mokkapati, Y Guo, L Li, J Wong-Leung, P Caroff, H H Tan, and C Jagadish. Selective-Area Epitaxy of Pure Wurtzite InP Nanowires: High Quantum Efficiency and Room-Temperature Lasing. *Nano Letters*, 14:5206–5211, 2014.

[144] D Dalacu, A Kam, D Guy Austing, X Wu, J Lapointe, G C Aers, and P J Poole. Selective-area vapour-liquid-solid growth of InP nanowires. *Nanotechnology*, 20:395602, 2009.

[145] Y Calahorra, Y Greenberg, S Cohen, and D Ritter. Native-oxide-based selective area growth of InP nanowires via metal-organic molecular beam epitaxy mediated by surface diffusion. *Nanotechnology*, 23:245603, 2012.

[146] A Bengoechea-Encabo, F Barbagini, S Fernandez-Garrido, J Grandal, J Ristic, M A Sanchez-Garcia, E Calleja, U Jahn, . Luna, and A Trampert. Understanding the selective area growth of GaN nanocolumns by MBE using Ti nanomasks. *Journal of Crystal Growth*, 325:89–92, 2011.

[147] K A Bertness, A Roshko, L M Mansfield, T E Harvey, and N A Sanford. Mechanism for spontaneous growth of GaN nanowires with molecular beam epitaxy. *Journal of Crystal Growth*, 310:3154–3158, 2008.

[148] F Schuster, F Furtmayr, R Zamani, C Magén, J R Morante, J Arbiol, J A Garrido, and M Stutzmann. Self-assembled GaN nanowires on diamond. *Nano Letters*, 12:2199–2204, 2012.

[149] X Wang, S B Che, Y Ishitani, and A Yoshikawa. Growth of In-polar and N-polar InN nanocolumns on GaN templates by molecular beam epitaxy. *Physica Status Solidi (C) Current Topics in Solid State Physics*, 3:1561–1565, 2006.

[150] T Stoica, R Meijers, R Calarco, T Richter, and H Lüth. MBE growth optimization of InN nanowires. *Journal of Crystal Growth*, 290:241–247, 2006.

[151] Y-L Chang, F Li, A Fatehi, and Z Mi. Molecular beam epitaxial growth and characterization of non-tapered InN nanowires on Si(111). *Nanotechnology*, 20:345203, 2009.

[152] V Sallet, C Sartel, C Vilar, A Lusson, and P Galtier. Opposite crystal polarities observed in spontaneous and vapour-liquid-solid grown ZnO nanowires. *Applied Physics Letters*, 102, 2013.

[153] S Guillemin, L Rapenne, H Roussel, E Sarigiannidou, G Brémond, and V Consonni. Formation Mechanisms of ZnO Nanowires : The Crucial Role of Crystal Orientation and Polarity. *The Journal of Physical Chemistry C*, 117:20738–20745, 2013.

[154] Y Sun, D Cherns, R P Doherty, J L Warren, and P J Heard. Reduction of threading dislocations in ZnO/(0001) sapphire film heterostructure by epitaxial lateral overgrowth of nanorods. *Journal of Applied Physics*, 104, 2008.

[155] D P Nicholls, R Vincent, D Cherns, Y Sun, and M N R Ashfold. Polarity determination of zinc oxide nanorods by defocused convergent-beam electron diffraction. *Philosophical Magazine Letters*, 87:417–421, 2007.

[156] D A Scrymgeour, T L Sounart, N C Simmons, and J W P Hsu. Polarity and piezoelectric response of solution grown zinc oxide nanocrystals on silver. *Journal of Applied Physics*, 101:014316, 2007.

[157] G Perillat-Merceroz, R Thierry, P-H Jouneau, P Ferret, and G Feuillet. Compared growth mechanisms of Zn-polar ZnO nanowires on O-polar ZnO and on sapphire. *Nanotechnology*, 23:125702, 2012.

[158] V Consonni, E Sarigiannidou, E Appert, A Bocheux, and S Guillemin. Selective Area Growth of Well-Ordered ZnO Nanowire Arrays with Controllable Polarity. *ACS nano*, 8:4761–4770, 2014.

[159] J Jasinski, D Zhang, J Parra, V Katkanant, and V J Leppert. Application of channeling-enhanced electron energy-loss spectroscopy for polarity determination in ZnO nanopillars. *Applied Physics Letters*, 92:093104, 2008.

[160] F Schuster, S Weiszer, M Hetzl, A Winnerl, J A Garrido, and M Stutzmann. Influence of substrate material, orientation, and surface termination on GaN nanowire growth. *Journal of Applied Physics*, 116(2014):054301, 2014.

[161] S Fernández-Garrido, V M Kaganer, K K Sabelfeld, T Gotschke, J Grandal, E Calleja, L Geelhaar, and O Brandt. Self-regulated radius of spontaneously formed GaN nanowires in molecular beam epitaxy. *Nano Letters*, 13:3274–3280, 2013.

[162] K Kishino, H Sekiguchi, and A Kikuchi. Improved Ti-mask selective-area growth (SAG) by rf-plasma-assisted molecular beam epitaxy demonstrating extremely uniform GaN nanocolumn arrays. *Journal of Crystal Growth*, 311:2063–2068, 2009.

[163] K A Dick and P Caroff. Metal-seeded growth of III-V semiconductor nanowires: towards gold-free synthesis. *Nanoscale*, 6:3006–21, 2014.

[164] T R Kuykendall, M V P Altoe, D F Ogletree, and S Aloni. Catalyst-Directed Crystallographic Orientation Control of GaN Nanowire Growth. *Nano Letters*, 14:6767–6773, 2014.

[165] H Wang, L A Zepeda-Ruiz, G H Gilmer, and M Upmanyu. Atomistics of vapour-liquid-solid nanowire growth. *Nature Communications*, 4:1956, 2013.

[166] R Sun, D Jacobsson, I-J Chen, M Nilsson, C Thelander, S Lehmann, and K A Dick. Sn-Seeded GaAs Nanowires as Self-Assembled Radial p-n Junctions. *Nano Letters*, 15:3757–3762, 2015.

[167] T Kuykendall, P J Pauzauskie, Y Zhang, J Goldberger, D Sirbuly, J Denlinger, and P Yang. Crystallographic alignment of high-density gallium nitride nanowire arrays. *Nature Materials*, 3:524–528, 2004.

[168] S Breuer, L-F Feiner, and L Geelhaar. Droplet Bulge Effect on the Formation of Nanowire Side Facets. *Crystal Growth & Design*, 13:2749–2755, 2013.

[169] T Chiaramonte, L H G Tizei, D Ugarte, and M A Cotta. Kinetic effects in InP nanowire growth and stacking fault formation: The role of interface roughening. *Nano Letters*, 11:1934–1940, 2011.

[170] E Russo-Averchi, J Vukajlovic Plestina, G Tütüncüoglu, F Matteini, A Dalmau Mallorqui, M de la Mata, D Rüffer, H Potts, J Arbiol, S Conesa-Boj, and A Fontcuberta i Morral. High yield of GaAs nanowire arrays on Si mediated by the pinning and contact angle of Ga. *Nano Letters*, 15:2869–2874, 2015.

[171] X Yuan, P Caroff, J Wong-Leung, L Fu, H Hoe Tan, and C Jagadish. Tunable polarity in a III-V nanowire by droplet wetting and surface energy engineering. *Advanced Materials*. In press.

[172] Z Wang, X Kong, and J Zuo. Induced Growth of Asymmetric Nanocantilever Arrays on Polar Surfaces. *Physical Review Letters*, 91:185502, 2003.

[173] S H Lee, T Minegishi, J Sub Park, S Hwan Park, J S Ha, H J Lee, H J Lee, S Ahn, J Kim, H Jeon, and T Yao. Ordered arrays of ZnO nanorods grown on periodically polarity-inverted surfaces. *Nano Letters*, 8:2419–2422, 2008.

[174] J Park, K H Kim, S H Park, E Yoon, and Ti Yao. Catalyst-free growth of vertically aligned ZnO nanostructures arrays on periodically polarity-inverted substrate. *Applied Physics Express*, 3, 2010.

[175] J Park and T Yao. Position-controlled vertical arrays of single-crystalline ZnO nanowires on periodically polarity inverted templates. *Journal of Alloys and Compounds*, 513:180–183, 2012.

[176] A P Goldstein, S C Andrews, R F Berger, V R Radmilovic, J B Neaton, and P Yang. Zigzag inversion domain boundaries in indium zinc oxide-based nanowires: structure and formation. *ACS Nano*, 7:10747–10751, 2013.

[177] H Schmid, E Okunishi, T Oikawa, and W Mader. Structural and elemental analysis of iron and indium doped zinc oxide by spectroscopic imaging in Cs-corrected STEM. *Micron*, 43:49–56, 2012.

[178] Y Zhu, Y Zhou, M I B Utama, M de la Mata, Y Zhao, Q Zhang, B Peng, C Magen, J Arbiol, and Q Xiong. Solution phase van der Waals epitaxy of ZnO wire arrays. *Nanoscale*, 5:7242–7249, 2013.

[179] S M Hughes and A P Alivisatos. Anisotropic formation and distribution of stacking faults in II-VI semiconductor nanorods. *Nano Letters*, 13:106–110, 2013.

[180] E Janik, P Dłużewski, S Kret, a Presz, H Kirmse, W Neumann, W Zaleszczyk, L T Baczewski, a Petroutchik, E Dynowska, J Sadowski, W Caliebe, G Karczewski, and T Wojtowicz. Catalytic growth of ZnTe nanowires by molecular beam epitaxy: structural studies. *Nanotechnology*, 18:475606, 2007.

[181] Y Cai, T L Wong, S K Chan, I K Sou, D S Su, and N Wang. Growth behaviors of ultrathin ZnSe nanowires by Au-catalyzed molecular-beam epitaxy. *Applied Physics Letters*, 93:16–19, 2008.

[182] D Moore and Z L Wang. Growth of anisotropic one-dimensional ZnS nanostructures. *Journal of Materials Chemistry*, 16:3898–3905, 2006.

[183] Y Wang, G Z Wang, M Y Yau, C Y To, and D H L Ng. Asymmetric growth on the polar surfaces of CdS ribbons. *Chemical Physics Letters*, 407:510–515, 2005.

[184] D D D Ma, C S Lee, F C K Au, S Y Tong, and S T Lee. Small-diameter silicon nanowire surfaces. *Science*, 299:1874–1877, 2003.

[185] Y Hao, G Meng, Z L Wang, C Ye, and L Zhang. Periodically twinned nanowires and polytypic nanobelts of ZnS: The role of mass diffusion in vapor-liquid-solid growth. *Nano Letters*, 6:1650–1655, 2006.

[186] Matthew J Bierman, Y K Albert Lau, Alexander V Kvit, Andrew L Schmitt, and Song Jin. Dislocation-Driven Nanowire Growth and Eshelby Twist. *Scie*, 320:1060–1063, 2008.

[187] E Russo-Averchi, a Dalmau-Mallorquí, I Canales-Mundet, G Tütüncüoğlu, E Alarcon-Llado, M Heiss, D Rüffer, S Conesa-Boj, P Caroff, and A Fontcuberta i Morral. Growth mechanisms and process window for InAs V-shaped nanoscale membranes on Si[001]. *Nanotechnology*, 24:435603, 2013.

[188] R R Zamani, M Ibáñez, M Luysberg, N García-Castelló, L Houben, J Dl Prades, V Grillo, R E Dunin-Borkowski, J R Morante, A Cabot, and J Arbiol. Polarity-driven polytypic branching in cu-based quaternary chalcogenide nanostructures. *ACS nano*, 8:2290–301, 2014.

[189] Utama, M I B†, de la Mata, M†, C Magen, J Arbiol, and Q Xiong. Twinning-, Polytypism-, and Polarity-Induced Morphological Modulation in Nonplanar Nanostructures with van der Waals Epitaxy. *Advanced Functional Materials*, 23:1636–1646, 2013.

[190] Q Zhang, J Zhang, M I B Utama, B Peng, M de la Mata, J Arbiol, and Q Xiong. Exciton-phonon coupling in individual ZnTe nanorods studied by resonant Raman spectroscopy. *Physical Review B*, 85:085418, 2012.

[191] L Li, M Zhao, X Zhang, Z Zhu, F Li, J Li, C Song, X Liu, and Y Xia. Theoretical insight into faceted zns nanowires and nanotubes from interatomic potential and first-principles calculations. *Journal of Physical Chemistry C*, 112(10):3509–3514, 2008.

[192] Z L Wang. ZnO nanowire and nanobelt platform for nanotechnology. *Materials Science and Engineering R: Reports*, 64:33–71, 2009.

[193] J Johansson, L S Karlsson, C P T Svensson, T Mårtensson, B A Wacaser, K Deppert, L Samuelson, and W Seifert. Structural properties of ⟨111⟩B -oriented III-V nanowires. *Nature Materials*, 5:574–580, 2006.

[194] R Wu, Y Pan, G Yang, M Gao, L Wu, J Chen, R Zhai, and J Lin. Twinned SiC Zigzag Nanoneedles. *Journal of Physical Chemistry C*, 111:6233–6237, 2007.

[195] P Caroff, K A Dick, J Johansson, M E Messing, K Deppert, and L Samuelson. Controlled polytypic and twin-plane superlattices in III-V nanowires. *Nature Nanotechnology*, 4:50–55, 2009.

[196] R E Algra, M A Verheijen, L Feiner, G G W Immink, R Theissmann, W J P van Enckevort, E Vlieg, and E P A M Bakkers. Paired twins and [112] morphology in GaP nanowires. *Nano Letters*, 10:2349–2356, 2010.

[197] D T J Hurle. A mechanism for twin formation during Czochralski and encapsulated vertical Bridgman growth of III-V compound semiconductors . *Journal of Crystal Growth*, 147:239–250, 1995.

[198] V G Dubrovskii and N V Sibirev. Growth thermodynamics of nanowires and its application to polytypism of zinc blende III-V nanowires. *Physical Review B*, 77:035414, 2008.

[199] L Manna, E C Scher, and A P Alivisatos. Synthesis of soluble and processable rod-, arrow-, teardrop-, and tetrapod-shaped CdSe nanocrystals. *Journal of the American Chemical Society*, 122:12700–12706, 2000.

[200] M I B Utama, Q Zhang, S Jia, D Li, J Wang, and Q Xiong. Epitaxial II-VI tripod nanocrystals: a generalization of van der Waals epitaxy for nonplanar polytypic nanoarchitectures. *ACS Nano*, 6:2281–2288, 2012.

[201] E Uccelli, J Arbiol, C Magen, P Krogstrup, E Russo-Averchi, M Heiss, G Mugny, J Nyg, J R Morante, and A Fontcuberta i Morral. Three-Dimensional Multiple-Order Twinning of Self-Catalyzed GaAs. *Nano Letters*, 11:3827–3832, 2011.

[202] M Shiojiri and C Kaito. Structure and Growth of ZnO Smoke Particles Prepared by Gas Evaporation Technique. *Journal of the American Chemical Society*, 52:173–177, 1981.

[203] X Fang, Y Bando, U K Gautam, T Zhai, S Gradečak, and D Golberg. Heterostructures and superlattices in one-dimensional nanoscale semiconductors. *Journal of Materials Chemistry*, 19:5683, 2009.

[204] Q Zhang, X Liu, M I B Utama, J Zhang, M de la Mata, J Arbiol, Y Lu, T C Sum, and Q Xiong. Highly enhanced exciton recombination rate by strong electron-phonon coupling in single ZnTe nanobelt. *Nano Letters*, 12:6420–6427, 2012.

[205] Utama, M I B†, de la Mata, M†, Q Zhang, C Magen, Ji Arbiol, and Q Xiong. The Growth of Ultralong ZnTe Micro/Nanostructures: The Influence of Polarity and Twin Direction on the Morphogenesis of Nanobelts and Nanosheets. *Crystal Growth & Design*, 13:2590–2596, 2013.

[206] B Zu, R Dai, Z W Pan, and Z L Wang. Novel Nanostructures of Functional Oxides Synthesized by Thermal Evaporation. *Advanced Functional Materials*, 13:9–24, 2003.

[207] S Conesa-Boj, E Russo-Averchi, A Dalmau-Mallorqui, J Trevino, E F Pecora, C Forestiere, A Handin, M Ek, L Zweifel, L R Wallenberg, D Rüffer, M Heiss, D Troadec, L Dal Negro, P Caroff, and A Fontcuberta i Morral. Vertical "III-V" V-shaped nanomembranes epitaxially grown on a patterned Si[001] substrate and their enhanced light scattering. *ACS Nano*, 6:10982–10991, 2012.

[208] J M Soler, E Artacho, J D Gale, A Garcia, J Junquera, P Ordejon, and D Sanchez-Portal. The SIESTA method for ab initio order-N materials simulation. *Journal of Physics: Condensed Matter*, 14:2745–2779, 2002.

[209] E L Wood and F Sansoz. Growth and properties of coherent twinning superlattice nanowires. *Nanoscale*, 4:5268–5276, 2012.

[210] F M Ross. Controlling nanowire structures through real time growth studies. *Reports on Progress in Physics*, 73:114501, 2010.

[211] S K Lim, S Crawford, G Haberfehlner, and S Gradečak. Controlled modulation of diameter and composition along individual III-V nitride nanowires. *Nano Letters*, 13:331–336, 2013.

[212] P Caroff, J B Wagner, K A Dick, H A Nilsson, M Jeppsson, K Deppert, L Samuelson, L R Wallenberg, and L-E Wernersson. High-quality InAs/InSb nanowire heterostructures grown by metal-organic vapor-phase epitaxy. *Small*, 4:878–882, 2008.

[213] L Lugani, D Ercolani, L Sorba, N V Sibirev, M A Timofeeva, and V G Dubrovskii. Modeling of InAs-InSb nanowires grown by Au-assisted chemical beam epitaxy. *Nanotechnology*, 23:095602, 2012.

[214] T Zhang, J J Harris, W R Branford, Y V Bugoslavsky, S K Clowes, L. F. Cohen, A. Husmann, and S A Solin. Tuning the inherent magnetoresistance of InSb thin films. *Applied Physics Letters*, 88:012110, 2006.

[215] T Zhang, S K Clowes, M Debnath, A Bennett, C Roberts, J. J. Harris, R A Stradling, L F Cohen, T Lyford, and P F Fewster. High-mobility thin InSb films grown by molecular beam epitaxy. *Applied Physics Letters*, 84:4463, 2004.

[216] I van Weperen, S R Plissard, E P A M Bakkers, S M Frolov, and L P Kouwenhoven. Quantized Conductance in an InSb Nanowire. *Nano Letters*, 13:387–391, 2013.

[217] N Goel, J Graham, J C Keay, K Suzuki, S Miyashita, M B Santos, and Y Hirayama. Ballistic transport in InSb mesoscopic structures. *Physica E*, 26:455–459, 2005.

[218] Y Jiang, X Zhang, Y Wang, N Wang, D West, S Zhang, and Z Zhang. Vertical/Planar Growth and Surface Orientation of Bi2Te3 and Bi2Se3 Topological Insulator Nanoplates. *Nano Letters*, 15:3147–3152, 2015.

[219] Y L Chen, J G Analytis, J-H Chu, Z K Liu, S-K Mo, X L Qi, H J Zhang, D H Lu, X Dai, Z Fang, S C Zhang, I R Fisher, Z Hussain, and Z-X Shen. Experimental realization of a three-dimensional topological insulator, Bi_2Te_3. *Science*, 325:178–181, 2009.

[220] Y Zhao, M de la Mata, R L J Qiu, J Zhang, X Wen, C Magen, X P A Gao, J Arbiol, and Q Xiong. Te-seeded growth of few-quintuple layer Bi_2Te_3 nanoplates. *Nano Research*, 7:1243–1253, 2014.

[221] R Brebrick and F Smith. Partial and total vapor pressures over molten Bi_2Te_3. *Journal of the Electrochemical Society*, 118:991–996, 1971.

[222] R. P Elliott. Constitution of Binary Alloys, First Supplement. *McGraw-Hill Company: New York*, 1965.

[223] D. L. Medlin, Q. M. Ramasse, C. D. Spataru, and N. Y. C. Yang. Structure of the (0001) basal twin boundary in Bi_2Te_3. *Journal of Applied Physics*, 108:043517, 2010.

[224] D L Medlin and N Y C Yang. Interfacial Step Structure at a (0001) Basal Twin in Bi_2Te_3. *Journal of Electronic Materials*, 41:1456–1464, 2012.

[225] M K Horton, S Rhode, S-L Sahonta, M J Kappers, S J Haigh, T J Pennycook, C J Humphreys, R O Dusane, and M A Moram. Segregation of In to Dislocations in InGaN. *Nano Letters*, 15, 2015.

[226] M T Björk, B J Ohlsson, T Sass, A I Persson, C Thelander, M H Magnusson, K Deppert, L R Wallenberg, and L Samuelson. One-dimensional Steeplechase for Electrons Realized. *Nano Letters*, 2:87–89, 2002.

[227] M W Larsson, J B Wagner, M Wallin, P Håkansson, L E Fröberg, L Samuelson, and L R Wallenberg. Strain mapping in free-standing heterostructured wurtzite InAs/InP nanowires. *Nanotechnology*, 18:015504, 2007.

[228] E Ertekin, P A Greaney, D C Chrzan, and T D Sands. Equilibrium limits of coherency in strained nanowire heterostructures. *Journal of Applied Physics*, 97:114325, 2005.

[229] F Glas. Critical dimensions for the plastic relaxation of strained axial heterostructures in free-standing nanowires. *Physical Review B*, 74:121302, 2006.

[230] G Kästner and U Gösele. Stress and dislocations at cross-sectional heterojunctions in a cylindrical nanowire. *Philosophical Magazine*, 84:3803–3824, 2004.

[231] G Signorello, S Karg, M T Björk, B Gotsmann, and H Riel. Tuning the light emission from GaAs nanowires over 290 meV with uniaxial strain. *Nano Letters*, 13:917–924, 2013.

[232] K-H Hong, J Kim, S-H Lee, and J K Shin. Strain-Driven Electronic Band Structure Modulation of Si Nanowires 2008. *Nano Letters*, 8:1335–1340, 2008.

[233] C P Kuo, S K Vong, R M Cohen, and G B Stringfellow. Effect of mismatch strain on band gap in III-V semiconductors. *Journal of Applied Physics*, 57:5428, 1985.

[234] W L Ng, M a Lourenço, R M Gwilliam, S Ledain, G Shao, and K P Homewood. An efficient room-temperature silicon-based light-emitting diode. *Nature*, 410:192–194, 2001.

[235] M-E Pistol and C Pryor. Band structure of core-shell semiconductor nanowires. *Physical Review B*, 78:115319, 2008.

[236] C Pryor and M-E Pistol. Band-edge diagrams for strained III-V semiconductor quantum wells, wires, and dots. *Physical Review B*, 72:205311, 2005.

[237] P D Kanungo, H Schmid, M T Björk, L M Gignac, C Breslin, J Bruley, C D Bessire, and H Riel. Selective area growth of III-V nanowires and their heterostructures on silicon in a nanotube template: towards monolithic integration of nano-devices. *Nanotechnology*, 24:225304, 2013.

[238] R Popovitz-Biro, A Kretinin, P von Huth, and H Shtrikman. InAs / GaAs Core-Shell Nanowires. *Crystal Growth & Design*, 11:3858–3865, 2011.

[239] M Jeppsson, K A Dick, J B Wagner, P Caroff, K Deppert, L Samuelson, and L-E Wernersson. GaAs/GaSb nanowire heterostructures grown by MOVPE. *Journal of Crystal Growth*, 310:4115–4121, 2008.

[240] P Caroff, M E Messing, B Mattias Borg, K A Dick, K Deppert, and L-E Wernersson. InSb heterostructure nanowires: MOVPE growth under extreme lattice mismatch. *Nanotechnology*, 20:495606, 2009.

[241] Y N Guo, J Zou, M Paladugu, H Wang, Q Gao, H H Tan, and C Jagadish. Structural characteristics of GaSb/GaAs nanowire heterostructures grown by metal-organic chemical vapor deposition. *Applied Physics Letters*, 89:231917, 2006.

[242] D Ercolani, F Rossi, A Li, S Roddaro, V Grillo, G Salviati, F Beltram, and L Sorba. InAs/InSb nanowire heterostructures grown by chemical beam epitaxy. *Nanotechnology*, 20:505605, 2009.

[243] M Jeppsson, K A Dick, H A Nilsson, N Sköld, J B Wagner, P Caroff, and L-E Wernersson. Characterization of GaSb nanowires grown by MOVPE. *Journal of Crystal Growth*, 310:5119–5122, 2008.

[244] M Ek, B M Borg, J Johansson, and K A Dick. Diameter Limitation in Growth of III-Sb-Containing Nanowire Heterostructures. *ACS Nano*, 7:3668–3675, 2013.

[245] D S Kim, U Gösele, and M Zacharias. Surface-diffusion induced growth of ZnO nanowires. *Journal of Crystal Growth*, 311:3216–3219, 2009.

[246] S A Chambers, T C Droubay, C M Wang, K M Rosso, S M Heald, D A Schwartz, K R Kittilstved, and D R Gamelin. Ferromagnetism in oxide semiconductors. *Materials Today*, 9:28–35, 2006.

[247] D Saxena, S Mokkapati, Nian Parkinson, P J, Q Gao, H H Tan, and C Jagadish. Optically pumped room-temperature gaas nanowire lasers. *Nature Photonics*, pages 963–968, 2013.

[248] B Mayer, Dl Rudolph, J Schnell, S Morkötter, J Winnerl, J Treu, K Müller, G Bracher, G Abstreiter, G Koblmüller, and J J Finley. Lasing from individual GaAs-AlGaAs core-shell nanowires up to room temperature. *Nature Communications*, 4:2931, 2013.

[249] W Wei, X-Y Bao, C Soci, Y Ding, Z-L Wang, and D Wang. Direct heteroepitaxy of vertical InAs nanowires on Si substrates for broad band photovoltaics and photodetection. *Nano Letters*, 9:2926–2934, 2009.

[250] H A Nilsson, P Caroff, C Thelander, M Larsson, J B Wagner, L-E Wernersson, L Samuelson, and H Q Xu. Giant , Level-Dependent g Factors in InSb Nanowire Quantum Dots. *Nano Letters*, 9:3151–3156, 2009.

[251] J Wang, S R Plissard, M A Verheijen, L-F Feiner, A Cavalli, and E P A M Bakkers. Reversible switching of InP nanowire growth direction by catalyst engineering. *Nano Letters*, 13:3802–3806, 2013.

[252] S Fahlvik Svensson, S Jeppesen, C Thelander, L Samuelson, H Linke, and K A Dick. Control and understanding of kink formation in InAs-InP heterostructure nanowires. *Nanotechnology*, 24:345601, 2013.

[253] S H Oh, M F Chisholm, Y Kauffmann, W D Kaplan, W Luo, M Rühle, and C Scheu. Oscillatory mass transport in vapor-liquid-solid growth of sapphire nanowires. *Science*, 330:489–493, 2010.

[254] C-Y Wen, J Tersoff, K Hillerich, M C Reuter, J H Park, S Kodambaka, E A Stach, and F M Ross. Periodically Changing Morphology of the Growth Interface in Si, Ge, and GaP Nanowires. *Physical Review Letters*, 107:025503, 2011.

[255] C V Falub, H von Känel, F Isa, R Bergamaschini, A Marzegalli, D Chrastina, G Isella, E Müller, P Niedermann, and L Miglio. Scaling hetero-epitaxy from layers to three-dimensional crystals. *Science*, 335:1330–1334, 2012.

[256] A M Rocher. Interfacial Dislocations in the GaSb/GaAs (001) Heterostructure. *Solid State Phenomena*, 19/20:563–572, 1991.

[257] S H Huang, G Balakrishnan, A Khoshakhlagh, A Jallipalli, L R Dawson, and D L Huffaker. Strain relief by periodic misfit arrays for low defect density GaSb on GaAs. *Applied Physics Letters*, 88:131911, 2006.

[258] de la Mata M, C Magen, P Caroff, and J Arbiol. Atomic Scale Strain Relaxation in Axial Semiconductor III-V Nanowire Heterostructures. *Letters, Nano*, 14:6614–6620, 2014.

[259] L Lugani, D Ercolani, F Rossi, G Salviati, F Beltram, and L Sorba. Faceting of InAs-InSb Heterostructured Nanowires. *Crystal Growth & Design*, 10:4038–4042, 2010.

[260] S J Pennycook and L A Boatner. Chemically sensitive structure-imaging with a scanning transmission electron microscope. *Nature*, 336:565–567, 1988.

[261] E M James and N D Browning. Practical aspects of atomic resolution imaging and analysis in STEM. *Ultramicroscopy*, 78:125–139, 1999.

[262] D L Dheeraj, G Patriarche, H Zhou, T B Hoang, A F Moses, S Grø nsberg, A T J van Helvoort, B-O Fimland, and H Weman. Growth and characterization of wurtzite GaAs nanowires with defect-free zinc blende GaAsSb inserts. *Nano Letters*, 8:4459–4463, 2008.

[263] B M Borg, K A Dick, Jl Eymery, and L-E Wernersson. Enhanced Sb incorporation in InAsSb nanowires grown by metalorganic vapor phase epitaxy. *Applied Physics Letters*, 98:113104, 2011.

[264] W Lu and C M Lieber. Nanoelectronics from the bottom up. *Nature Materials*, 6:841–850, 2007.

[265] S Deshpande, J Heo, A Das, and P Bhattacharya. Electrically driven polarized single-photon emission from an InGaN quantum dot in a GaN nanowire. *Nature Communications*, 4:1675, 2012.

[266] Y B Tang, Z H Chen, H S Song, C S Lee, H T Cong, H M Cheng, W J Zhang, I Bello, and S T Lee. Vertically Aligned p-Type Single-Crystalline GaN Nanorod Arrays on n-Type Si for Heterojunction Photovoltaic Cells. *Nano Letters*, 8:4191–4195, 2008.

[267] C-T Huang, J Song, W-F Lee, Y Ding, Z Gao, Y Hao, L-J Chen, and Z L Wang. GaN Nanowire Arrays for High-Output Nanogenerators. *Journal of American Chemical Society*, 132:4766–4771, 2010.

[268] E Monroy, M Hermann, E Sarigiannidou, T Andreev, P Holliger, S Monnoye, H Mank, B Daudin, and M Eickhoff. Polytype transition of N-face GaN:Mg from wurtzite to zinc-blende. *Journal of Applied Physics*, 96:3709, 2004.

[269] G Jacopin, L Rigutti, L Largeau, F Fortuna, F Furtmayr, F H Julien, M Eickhoff, and M Tchernycheva. Optical properties of wurtzite/zinc-blende heterostructures in GaN nanowires. *Journal of Applied Physics*, 110:064313, 2011.

[270] P Hille, J Müß ener, P Becker, M de la Mata, N Rosemann, C Magén, J Arbiol, J Teubert, S Chatterjee, J Schörmann, and M Eickhoff. Screening of the quantum-confined Stark effect in AlN/GaN nanowire superlattices by germanium doping. *Applied Physics Letters*, 104:102104, 2014.

[271] M Beeler, C B Lim, P Hille, J Bleuse, J Schörmann, M de la Mata, J Arbiol, M Eickhoff, and E Monroy. Long-lived excitons in GaN/AlN nanowire heterostructures. *Physical Review B*, 91:205440, 2015.

[272] M Beeler, P Hille, J Schörmann, J Teubert, M de la Mata, J Arbiol, M Eickhoff, and E Monroy. Intraband absorption in self-assembled Ge-doped GaN/AlN nanowire heterostructures. *Nano Letters*, 14:1665–1673, 2014.

[273] G Tourbot, C Bougerol, F Glas, L F Zagonel, Z Mahfoud, S Meuret, P Gilet, M Kociak, B Gayral, and B Daudin. Growth mechanism and properties of InGaN insertions in GaN nanowires. *Nanotechnology*, 23:135703, 2012.

[274] J Schörmann, P Hille, M Schäfer, J Müß ener, P Becker, P J Klar, M Kleine-Boymann, M Rohnke, M de la Mata, J Arbiol, D M Hofmann, J Teubert, and M Eickhoff. Germanium doping of self-assembled GaN nanowires grown by plasma-assisted molecular beam epitaxy. *Journal of Applied Physics*, 114:103505, 2013.

[275] T Richter, H L R Meijers, R Calarco, and M Marso. Doping Concentration of GaN Nanowires Determined by Opto-Electrical Measurements. *Nano Letters*, 8:3056–3059, 2008.

APPENDIX A

Nomenclature

ABF	Annular Bright Field
CBD	Chemical Bath Deposition
CBED	Convergent Beam Electron Diffraction
C_c	Chromatic Aberration
CL	Cathodoluminescence
C_s	Spherical Aberration
EDS or EDX	Energy Dispersive X-ray Spectroscopy
EELS	Electron Energy-Loss Spectroscopy
fcc	Face-centered cubic
HAADF	High Angle Annular Dark Field
hcp	Hexagonal closed-packed
HRTEM	High Resolution Transmission Electron Microscopy
MBE	Molecular Beam Epitaxy

MOCVP	Metal-Organic Chemical Vapor Deposition
MOVPE	Metal-Organic Vapor Phase Epitaxy
ND	Nanodisc
NPT	Nanoplate
NS	Nanosail
NW	Nanowire
PL	Photoluminescence
QD	Quantum Dot
QS	Quantum Structure
QWR	Quantum Wire
QW	Quantum Well
SAED	Selected Area Electron Diffraction
STEM	Scanning Transmission Electron Microscopy
STM	Scanning Tunnel Microscopy
VLS	Vapor-Liquid-Solid
VPE	Vapor Phase Epitaxy
WZ	Wurtzite
ZB	Zinc-blende

APPENDIX B

List of Atomic Weights

Element	***Z***
N	7
O	8
Al	13
P	15
S	16
Zn	30
Ga	31
As	33
Se	34
Cd	48
In	49
Sb	51
Te	52

APPENDIX C

List of Publications

Publications related to the PhD:

- Q. Zhang, J. Zhang, M. I. B. Utama, B. Peng, M. de la Mata, J. Arbiol, Q. Xiomg, *Exciton-phonon coupling in individual ZnTe nanorods studied by resonant Raman spectroscopy.* Physical Review B, **85**, 085418 (2012).

- M. de la Mata, C. Magen, J. Gazquez, M. I. B. Utama, M. Heiss, S. Lopatin, F. Furtmayr, C. J. Fernández-Rojas, B. Peng, J. R. Morante, R. Rurali, M. Eickhoff, A. Fontcuberta i Morral, Q Xiong, J. Arbiol, *Polarity assignment in ZnTe, GaAs, ZnO and GaN-AlN nanowires from direct dumbbell analysis.* Nano Letters, **12**, 2579 (2012)

- Q. Zhang, X. Liu, M. I. B. Utama, J. Zhang, M. de la Mata, Jordi Arbiol, T. C. Sum, Q. Xiong, *Highly Enhanced Exciton Recombination Rate by Strong Electron-phonon Coupling in Single ZnTe Nanobelt.* Nano Letters, **12**, 6420 (2012).

- M. I. B. Utama†, M. de la Mata†, Q. Zhang, C. Magen, J. Arbiol, Q. Xiong, *The Growth of Ultralong ZnTe Micro/Nanostructures: The Influence of Polarity and Twin Direction on The Morphogenesis of Nanobelts and Nanosheets.* Crystal Growth & Design, **13**, 2590 (2013).

- M. de la Mata, X. Zhou, F. Furtmayr, J. Teubert, S. Gradečak, M. Eickhoff, A. Fontcuberta i Morral, J. Arbiol, *A review of MBE grown 0D, 1D and 2D quantum structures in a nanowire.* Journal of Materials Chemistry C, **1**, 4300 (2013).

- J. Arbiol, M. de la Mata, M. Eickhoff, A. Fontcuberta i Morral, *Bandgap engineering in a nanowire: self-assembled 0, 1 and 2D quantum structures.* Materials Today, **16**, 213 (2013).

- J. Schörmann, P. Hille, M. Schäfer, J. Müβener, P. Becker, P. J. Klar, P. M. Kleine-Boymann, M. Rohnke, M. de la Mata, J. Arbiol, D. M. Hofmann, J. Teubert, M. Eickhoff, *Germanium doping of self-assembled GaN nanowires grown by plasma-assisted molecular beam epitaxy.* Journal of Applied Physics, **114**, 103505 (2013).

- M. I. B. Utama†, M. de la Mata†, C. Magen, J. Arbiol, Q. Xiong, *Twinning-, polytypism-, and polarity-induced morphological modulation in nonplanar nanostructures with van der Waals epitaxy.* Advanced Functional Materials, **23**, 1636 (2013).

- Y. Zhu, Y. Zhou, M. I. B. Utama, M. de la Mata, Y. Zhao, Q. Zhang, B. Peng, C. Magen, J. Arbiol, Q. Xiong, *Solution phase van der Waals epitaxy of ZnO wire arrays.* Nanoscale, **5**, 7242 (2013).

- M. de la Mata, J. Arbiol, *High Resolution in STEM Mode: Individual Atom Analysis in Semiconductor Nanowire. Transmission Electron Microscopy Characterization of Nanomaterials*, **ISBN**: 978-3-642-38933-7, Springer Heidelberg New York Dordrecht London, 375-425 (2014).

- M. Beeler, P. Hille, J. Schörmann, J. Teubert, M. de la Mata, J. Arbiol, M. Eickhoff, E. Monroy, *Intraband Absorption in Self-Assembled Ge-Doped GaN/AlN Nanowire Heterostructures.* Nano Letters, **14**, 1665 (2014).

- P. Hille, J. Müβener, P. Becker, M. de la Mata, N. Rosemann, C. Magén, J. Arbiol, J. Teubert, S. Chatterjee, J. Schörmann, M. Eickhoff, *Screening of the quantum-confined Stark effect in AlN/GaN nanowire superlattices by germanium doping.* Applied Physical Letters, **104**, 102104 (2014).

- Y. Zhao, M. de la Mata, R. L. J. Qiu, J. Zhang, X. Wen, C. Magen, X. P. A. Gao, J. Arbiol, Q. Xiong, *Te-seeded Growth of Few-Quintuple Layer Bi_2Te_3 Nanoplates.* Nano Research, **7**, 1243 (2014).

- J. Müβener, J. Teubert, P. Hille, M. Schäfer, J. Schörmann, M. de la Mata, J. Arbiol, M. Eickhoff, *Probing the Internal Electric Field in GaN/AlGaN Nanowire Heterostructures.* Nano Letters, **14**, 5118 (2014).

- M. de la Mata, C. Magen, P. Caroff, J. Arbiol, *Atomic Scale Strain Relaxation in Axial Semiconductor III-V Nanowire Heterostructures.* Nano Letters, **14**, 6614 (2014).

- F. Amaduzzi, E. Alarcon-Llado, E. Russo-Averchi, F. Matteini, M. Heiss, G. Tütüncüoglu, S. Conesa-Boj, M. de la Mata, J. Arbiol, A. Fontcuberta i Morral, *Probing inhomogeneous composition in core/shell nanowires by Raman spectroscopy.* Journal of Applied Physics, **116**, 184303 (2014).

- F. Schuster, M. Hetzl, S. Weiszer, J. Antonio Garrido, M. de la Mata, C. Magen, J. Arbiol, M. Stutzmann, *Position-Controlled Growth of GaN Nanowires and Nanotubes on Diamond by Molecular Beam Epitaxy.* Nano Letters, **15**, 1773 (2015).

- M. Beeler, C. B. Lim, P. Hille, J. Bleuse, J. Schörmann, M. de la Mata, J. Arbiol, M. Eickhoff, E. Monroy, *Long-lived excitons in GaN/AlN nanowire heterostructures.* Physical Review B, **91**, 205440 (2015).

- E. Russo-Averchi, G. Tütüncüoglu, A. Dalmau-Mallorqui, I. Canales Mundet, M. de la Mata, D. Rüffer, J. Arbiol, S. Conesa-Boj, A. Fontcuberta i Morral, *Bottom-up engineering of InAs at the nanoscale: from V-shaped nanomembranes to Nanowires.* Journal of Crystal Growth, **420**, 47 (2015).

- E. Russo-Averchi, J. Vukajlovic Plestina, G. Tütüncüoglu, F. Matteini, A. Dalmau Mallorqui, M. de la Mata, D. Rüffer, H. Potts, J. Arbiol, S. Conesa-Boj, A. Fontcuberta i Morral, *High yield of GaAs nanowire arrays on Si mediated by the pinning and contact angle of Ga.* Nano Letters, **15**, 2869 (2015).

- S. Mukherjee, U. Givan, S. Senz, A. Bergeron, S. Francoeur, M. de la Mata, J. Arbiol, T. Sekiguchi, K. M. Itoh, D. Isheim, D. N. Seidman, O. Moutanabbir, *Phonon Engineering in Isotopically Disordered Silicon Nanowires.* Nano Letters, **15**, 3885 (2015).

- G. Tütüncüoglu, M. de la Mata, D. Deiana, H. Potts, F. Matteini, J. Arbiol, A. Fontcuberta i Morral, *Towards defect-free 1-D GaAs/AlGaAs Heterostructures based on GaAs nanomembranes.* Submitted.

- M. de la Mata, R. Leturcq, S. Plissard, C. Rolland, X. Wallart, J. Arbiol, P. Caroff, *High mobility InSb nanosails: a convenient 2D quantum system.* In preparation.

Other publications developed during the PhD period:

- X. Liu, S. Tung Ha, Q. Zhang, M. de la Mata, C. Magen, J. Arbiol, T. Chien Sum, Q. Xiong, *Whispering Gallery Mode Lasing from Hexagonal Shaped Layered Lead Iodide Crystals.* ACS Nano, **9**, 687 (2015).

- M. Y. Bashouti, C. A. Garzuzi, M. de la Mata, J. Arbiol, J. Ristein, H. Haick, S. Christiansen, *The Role of Silicon Nanowire Diameter for Alkyl (chain lengths: C1-C18) Passivation Efficiency through Si-C Bonds.* Langmuir, **31**, 2430 (2015).

- A. Queraltó, A. Perez del Pino, M. de la Mata, J. Arbiol, X. Obradors, T. Puig, *Ultrafast crystallization of $Ce_{0.9}Zr_{0.1}O_{2-y}$ epitaxial films on flexible technical substrates by pulsed laser irradiation of chemical solution derived precursor layers.* Crystal Growth & Design, **15**, 1957 (2015).

- A. Queraltó, A. Pérez del Pino, M. de la Mata, J. Arbiol, M. Tristany, A. Gómez, X. Obradors, T. Puig, *Growth of ferroelectric $Ba_{0.8}Sr_{0.2}TiO_3$ epitaxial films by ultraviolet pulsed laser irradiation of chemical solution derived precursor layers.* Applied Physics Letters, **106**, 262903 (2015).

- A. Garzón-Manjón, E. Solano, M. de la Mata, R. Guzmán, J. Arbiol, T. Puig, X. Obradors, Ramón Yáñez, S. Ricart, J. Ros, *Induced shape controllability by tailored precursor design in thermal and microwave-assisted synthesis of Fe_3O_4 nanoparticles.* Journal of Nanoparticle Research, **17**, 291 (2015).

- D. Li, Y. Liu, M. de la Mata, C. Magen, J. Arbiol, Y. Feng, Q. Xiong, *Strain-induced spatially indirect exciton recombination in zinc-blende/wurtzite CdS heterostructures.* Nano Research, Accepted Manuscript, DOI: 10.1007/s12274-015-0809-8 (2015).